LOW-LEVEL CONVERGENCE AND ITS ROLE IN CONVECTIVE INTENSITY AND FREQUENCY OVER THE HOUSTON LIGHTNING AND RAINFALL ANOMALY

A Thesis

by

VERONICA ANN MCNEAR

Submitted to the Office of Graduate Studies of
Texas A&M University
in partial fulfillment of the requirements for the degree of

MASTER OF SCIENCE

May 2007

Major Subject: Atmospheric Sciences

LOW-LEVEL CONVERGENCE AND ITS ROLE IN CONVECTIVE INTENSITY AND FREQUENCY OVER THE HOUSTON LIGHTNING AND RAINFALL ANOMALY

A Thesis

by

VERONICA ANN MCNEAR

Submitted to the Office of Graduate Studies of
Texas A&M University
in partial fulfillment of the requirements for the degree of

MASTER OF SCIENCE

Approved by:

Chair of Committee,	Lawrence D. Carey
Committee Members,	John W. Nielsen-Gammon
	Daniel Z. Sui
Head of Department,	Richard E. Orville

May 2007

Major Subject: Atmospheric Sciences

ABSTRACT

Low-Level Convergence and Its Role in Convective Intensity and Frequency over the Houston Lightning and Rainfall Anomaly. (May 2007)

Veronica Ann McNear, B.S., Purdue University

Chair of Advisory Committee: Dr. Larry Carey

An increase in the amount of lightning and rainfall over the Houston area, compared to the surrounding rural areas, has been well documented in previous studies. The placement of a Shared Mobile Atmospheric Research and Teaching Radar (SMART-R) in the Houston area during the summer season of 2005 presented a unique opportunity to investigate the role of boundary-layer convergence in modulating convective frequency and intensity and, thereby, likely causing the rainfall and lightning anomalies. The role of the urban heat island (UHI) and the sea-breeze, as a source of low-level convergence leading to enhanced convection over Houston, was examined.

Hourly average dual-Doppler wind and convergence maps were created on 1 X 1 km grids for an eleven-week period. By using these images along with average lightning, rainfall, and reflectivity for a large Houston-centered domain, it was possible to discern a correlation between low-level convergence and convection. Also, past findings of enhancement in lightning and rainfall over Houston and downwind of Houston were validated. High convergence levels for the Houston area in the mid-morning were followed closely by a peak in convection in the early afternoon. The enhancement of

rainfall and lightning over and downwind of downtown was found to be primarily from a large increase in frequency of deep convective events when compared to the surrounding domain. Also, it was found that UHI, rather than sea-breeze, was likely the primary causative mechanism in the development of convection over the Houston area because of the lack of deep convection in areas equally affected by the sea-breeze and the timing of the convection compared to time of peak sea-breeze. An area of weaker enhancement south of Houston, not discussed in previous studies, was found to be present, possibly from the interactions between the bay-breeze off of the Galveston Bay and the sea-breeze.

DEDICATION

I would like to dedicate my thesis to my wonderful husband, Wes, and my daughter, Macy. This thesis would never have been completed without Wes's patience, understanding, and encouragement. His belief in my abilities, both academically and professionally, was the prime reason for any of my successes. Macy has given me unconditional love and an all new reason to succeed.

I would also like to dedicate this thesis to my family. Their support of Wes and me while we lived so far away were invaluable.

Finally, I would like to thank all of my friends and co-workers at Texas A&M who helped me cope with school, work, and having a family. The support I received was immeasurable, and I thank them from the bottom of my heart.

ACKNOWLEDGMENTS

I would like to extend deepest thanks to my advisor Dr. Larry Carey. His expertise and guidance were one of the most important elements in the completion of this thesis. I would also like to thank my committee members, Dr. Nielsen-Gammon and Dr. Daniel Sui for their time and assistance. I would like to thank Dr. Stephen Quiring for his willingness to substitute.

I would also like to thank all of my co-workers who offered their help. I would especially like to thank Chas Hodapp and Nate Clements for their assistance with the land-use map. Many corrections were made after discussions with my office mates!

This research was made possible by a grant from TCEQ and the NSF.

TABLE OF CONTENTS

CHAPTER Page

LIST OF FIGURES

FIGURE Page

FIGURE Page

FIGURE Page

LIST OF TABLES

CHAPTER I

INTRODUCTION

1.1 *Motivation*

As cities across the United States grow larger, so does their influence on the local climatology. It has long been known that the urban areas are warmer than their rural surroundings. This occurrence, known as the urban heat island, has a large effect on the local weather, and therefore has significant impacts on the local population. Increased temperature within cities can cause increases in convection, attributing to increases in lightning and rainfall. Urban heat islands have been extensively studied in order to try to understand the magnitudes and frequencies of these impacts.

Houston, Texas is the fourth largest city in the United States, with a 2005 population of just over 2 million and an estimated 2000 greater Houston metropolitan population of over 5.2 million (U.S. Census Bureau; http://www.census.gov/population/www/estimates/Estimates%20pages_final.html). Houston has many characteristics which make it unique among other large cities in the United States. Sitting along the Gulf Coast, Houston has a complex coastline with Galveston Bay and the shipping channel located to the east, and the Gulf Coast and Galveston Island to the south. Due to Houston's location, the city is frequently affected by both a bay-breeze and a sea-breeze during the afternoon hours. Houston also has a large amount of oil refineries, which create

---

This thesis follows the style of the *Journal of Applied Meteorology.*

particulate matter and increase pollution.

Past research has focused on the Houston area to examine what effects the city of Houston has on the local climatology. An increased amount of lightning (Figure 1.1) (Orville et al. 2001; Steiger et al. 2002) and rainfall (Figure 1.2) (Shepherd and Burian 2003) has been found over the Houston, Texas urban area. A lightning enhancement of 45% was found over the Houston area as compared with the background rural areas. The cloud-to-ground (CG) lightning enhancement was associated with large lightning events, indicating an increase in thunderstorm intensity, rather than an increase in thunderstorm initiation (Steiger et al. 2002). However, Gauthier et al. (2005) found that the area immediately east of Galveston Bay had an increase of 2.5 times the flash density of the mean of East Texas and West Louisiana, and when large lightning event days were removed, this anomaly decreased only to 1.5 to 2 times the mean over the same area.

Rainfall anomalies have also been apparent near the Houston area. Shepherd and Burian (2003) found that the largest rainfall amounts occurred during the summer months, down-wind of the city. Burian and Shepherd (2005) determined that the highest ratio of rainfall between the urban area and the local rural areas occurring during the hours of 1200 to 1600, local time. The urban area showed a 59% greater rainfall amount than the surrounding rural areas from noon to midnight, and the downwind areas had a 30% greater rainfall amount for the same time period during the warm season.

There have been many hypotheses for the observed increase in convection over the Houston area. Possible causes include Urban Heat Island, mesoscale convergence due to sea-breeze activity, and the increase in particulate matter around the Houston area due to the presence of oil refineries near the coast line and Galveston Bay. The enhancement of lightning due to the presence of aerosols was examined by Gauthier (2006). By isolating high pollution days, it was found that aerosols were not a significant contributing factor to the lightning enhancement. The effect of particulate matter on the enhancement of lightning will not be examined in this thesis.

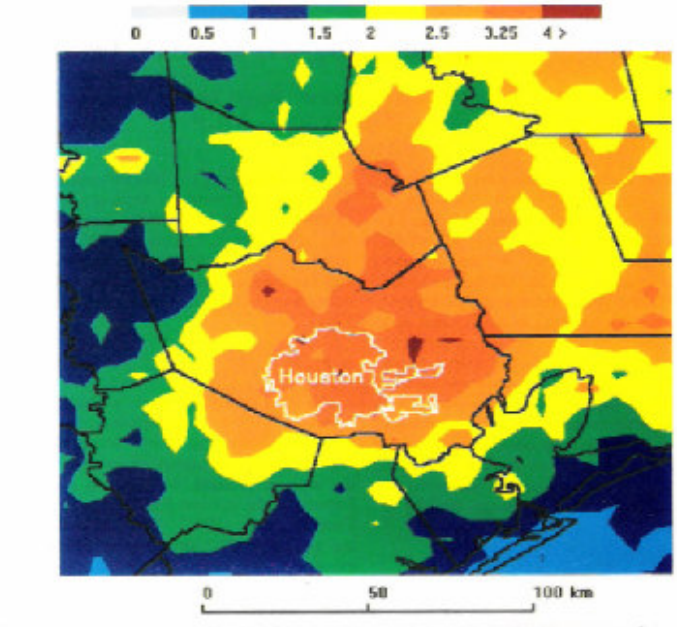

FIG. 1.1. Twelve year summer flash density (flashes km^{-2}) from 1989-2000 (Orville et al. 2001).

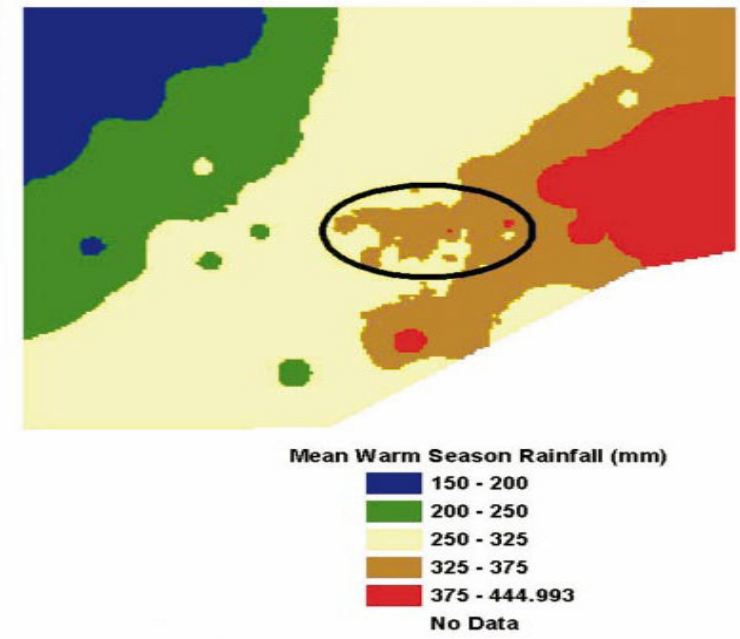

FIG. 1.2. Mean warm season rainfall over 13 year period from 1984-1997. Circle indicates Houston area (Shepherd and Burian 2003).

1.2 *Objective and Organization of Thesis*

The Second Texas Air Quality Study (TexAQS II) was a comprehensive research initiative to better understand the causes of air pollution and, ultimately, to improve regulatory analysis of and prediction tools for ozone. Air pollution events are the consequence of both atmospheric chemistry and meteorological processes on local to regional scales. An important component of this research initiative was to provide enhanced meteorological measurements during an extended period (spring 2005 – autumn 2006) over eastern Texas, including the urban environments of Houston-Galveston and Dallas-Fort Worth. A key objective of the enhanced meteorological

monitoring was to quantify the transport into, within (including on urban scales), and out of Texas so that the formation and accumulation of ozone can be better predicted.

During the summer of 2005, two Shared Mobile Atmospheric Research and Teaching Radars (SMART-R) were deployed to specifically sample boundary layer winds over the Greater Dallas-Fort Worth and Houston-Galveston metropolitan areas. This program provided virtually un-interrupted data from the period between mid-July to mid-September. The data presented a unique opportunity to study month long averages of high temporal and spatial resolution data over an urban domain. The thesis will present an analysis of the accuracy of the boundary layer dual-Doppler processed winds for both the SMART-R over the Houston (SR1) and Dallas (SR2) areas and month long averages of mesoscale features discernable from Doppler radar, such as boundary layer wind convergence, rainfall, reflectivity structure in the vertical, and lightning, over the Houston area. From these observations, the thesis will explore the potential roles of the Urban Heat Island and sea-breeze in modulating convective frequency and intensity and therefore producing the rainfall and lightning anomalies over the Houston area.

This thesis is divided into six chapters. Background and theory behind the relationship between Urban Heat Island (UHI) and sea breeze and convergence and convection, and the relationship between convection and lightning are presented in chapter II. Chapter II also presents the hypothesis and ancillary questions that will be addressed in this thesis. Chapter III consists of the data and methodology in regards to data retrieval, processing, and analysis techniques. Chapter IV discusses the results of both the boundary layer wind accuracy and the convective study over Houston and

chapter V includes a discussion of the results with regards to the Houston rainfall and lightning anomalies. Chapter VI includes a conclusion and suggestions for possible future research.

CHAPTER II

BACKGROUND AND THEORY

2.1 *Boundary-Layer Radar Retrieval*

Observations of the boundary-layer winds are very valuable when studying convective initiation. However, direct boundary-layer measurements are not often readily available, or may be sparse. Convective initiation studies require data samples where convection occurs, which cannot be easily predicted, making point measurements problematic. On the other hand, Doppler radar sampling provides high spatial (e.g., order 1 km) and temporal (e.g., order 10 minute) resolution winds in the boundary layer over a large domain (e.g., order 10,000 km^2) at the expense of increased error relative to more direct point measurements, as will be shown in Chapter III.

Current Doppler radars are highly sensitive to small (e.g., order 1-10 mm) targets in the atmosphere. Boundary-layer returns rely on the presence of passive tracers, that is, tracers that are carried by the wind. Radar returns from insects are the most common form of this type of tracer. Though insects have a velocity, flight is random and does not adversely affect the horizontal wind retrievals (Wilson et al. 1994). Birds are also responsible for some clear-air returns. Unlike insects, birds are normally isolated and appear as point targets, and therefore, do not cause large biases in the velocity data. However, during migration, birds can cause large errors in velocity (Gauthreaux et al. 1998). The problem of bird contamination is described in section 3.2.1.

2.2 *Sea-Breeze*

Sea-breezes are a common occurrence that affects the local climate of areas near the coast. Such water and land circulations also occur near other large bodies of water, such as the Great Lakes. The sea-breeze effect is a response to the temperature gradient between the land and water created from day-time heating. After sunrise, the temperature of the land surface quickly rises. Due to the large heat capacity of water, the temperature of the water rises much more slowly. The land air will expand as it heats, and this expansion creates a pressure gradient between the land surface and the ocean surface. The pressure gradient creates a circulation in which the winds at the surface will blow inland. Once sunset occurs, the opposite begins to take place. Once again, temperature change over land is fairly rapid, while temperature change over the water is considerably slower. This results in offshore winds, or land-breeze.

The sea-breeze passage is characterized by a change in many meteorological parameters. Sea-breeze passage is usually marked by a sudden change in wind speed and direction. Wind speed will increase, and the direction of the wind will change to perpendicular to the coastline. A drop in temperature and rise in dew point follow a sea-breeze front due to the advection of the cooler, moister ocean air.

2.2.1 *Sea-Breeze and Convergence*

The progression of the sea-breeze inland forms a boundary between the warmer, drier land air and the cooler, moister sea air. As the sea-breeze advances, it forces the warmer air to rise. If the lift is strong enough to overcome convective inhibition and the

air can reach the level of free convection (LFC), convection will form. This type of sea-breeze forcing occurs frequently near coastal areas and accounts for much of the typical afternoon convection during the summer months. The direction of the synoptic-scale flow plays a role in the strength of the sea-breeze front. When synoptic flow is offshore, the sea-breeze forms later, progresses inward more slowly, and is more sharply defined (Banta et al. 1993; Atkins and Wakimoto 1997). For the Texas Gulf Coast, a study of the 1000-700 hPA wind patterns over a 14 year warm season period revealed the most common low-level wind flow is from the southwest, with southeasterly flow the second most common (Smith et al. 2005).

A study of convective initiation along a sea-breeze in the Florida peninsula by Cooper et al. (1982) found that maximum convergence occurred approximately 90 minutes before peak upward convective transport. However, a model by Aksoy et al. (2005) found that the highest levels of convergence and vertical velocity occurred three hours after maximum heating. Burpee and Lahiff (1983) found that sea-breeze days accounted for 35-40% of summer rainfall over the south Florida peninsula. A model study by Shepherd et al. (2001) found that as winds behind the sea-breeze were increased, surface moisture convergence and initial rainfall were increased. It was also found that the magnitude of the convergence is more important for convective initiation than the depth of the sea-breeze. Kingsmill (1995) found that cells initiated on the areas of maximum convergence associated with sea-breeze front. Sea breeze convection enhances lightning density, especially on days with calm wind, less than 2.5 m s^{-1}, on the northern Gulf Coast (Smith et al. 2005). Complex coastlines and their influence on the

location of sea breeze convection were studied by Gibson and Vonder Haar (1990). According to their study, large bays hinder convergence associated with the sea-breeze, but convective maxima appear on land adjacent to the bays. Peninsulas enhance sea breeze convergence.

2.2.2 *The Houston Sea-Breeze*

The location of the city of Houston, both the latitude and complex shoreline, results in a very complicated sea-breeze pattern. Houston is located at approximately 30° north. At this latitude, the diurnal period and the inertial period are equal. This results in a temporary cancellation of the sea-breeze winds when the gradient wind is similar in magnitude (Banta et al. 2005). There is also a breeze associated with the presence of the Galveston Bay. This breeze is often weaker and occurs earlier in the day than the larger sea-breeze. The idealized sea-breeze wind pattern for Houston begins from the north before sunrise, and then proceeds clockwise through the morning and early afternoon, southerly in the afternoon, and then westerly after sunset before returning to northerly overnight (Banta et al. 2005).

Convection over Houston caused by the sea breeze is of interest due to the complexity of the Houston shoreline and the location of the Galveston Bay. A numerical study by McPherson (1970) found that sea-breeze convergence is distorted land-ward by the presence of a bay, and that convection forms northwest and northeast of a Bay. In the case of the Galveston area, it was found that convection would form near Houston. Enhanced sea breeze days were found to contribute to about a quarter of the mean flash

density over the northeast and southern Houston areas (Gauthier 2006). Gauthier et al. (2005) found the Houston lightning enhancement to be a local anomaly but not unique along the Gulf Coast. However, Shepherd and Burian (2003) found the Houston area to be a unique area of enhanced rainfall in the band of Gulf Coast sea-breeze convergence.

2.3 *Urban Heat Island*

The urban heat island (UHI) effect occurs due to the presence of buildings and pavement in contrast to natural vegetation. Various causes for the UHI were outlined in Arya (2001) and include increased incoming longwave radiation from pollution, decreased outgoing longwave radiation due to absorption by buildings, increased shortwave radiation absorption due to lower albedo, large heat storage because of the thermal properties of urban materials, additional heat release due to industrial, commercial, and transportation operations, and decreased evaporation due to lack of vegetation. This trapped radiation and heat increases the temperature over the urban area, creating a temperature gradient that can be several degrees between the urban and adjacent rural areas.

2.3.1 *UHI and Convergence*

UHI can affect convection due to thermodynamic and dynamic effects. Thermodynamic effects include increased temperatures and increased instability. Thermodynamic effects over the Houston area are difficult to resolve due to the lack of upper air information. Only dynamic effects due to low-level convergence will be

examined in this thesis. Dynamic effects include the convergence of winds due to temperature, and therefore pressure gradient differences. The low-level horizontal convergence forces vertical motion. A study by Kurbatskii (2001) modeled an urban temperature field and found positive buoyancy in the lower section of the urban thermal plume. If vertical motion is large enough, the LFC will be reached for the air parcels, and convection will form.

Convection caused by UHI effect has been shown to occur over many large cities. The Metropolitan Meteorological Experiment (METROMEX) field project studied urban effects over the city of St. Louis during the summers of 1971-1976. Large surface temperature differences were found between the city and the surrounding rural areas. The temperature difference was found to be decreased, but still present, at an elevation of 1 km above the surface. Observations of wind fields at 450 m showed perturbation streamlines converging over the urban area and the divergence associated with the streamlines correlate to the thermal field (Auer 1981). A plot of the locations of the first radar detectable echo, made to analyze convective initiation caused by St. Louis, showed an increase in convective initiation centered over downtown (Braham, Jr. 1981). Convection initiation frequencies were twice that of the local rural areas. Also, echo tops were an average of 4 km higher over urban areas than rural. More recently, Changnon et al. (1991) found marked increases in precipitation downwind of St. Louis during the months of September and October. A simulation of St. Louis also showed convergence and convection downwind of the city (Rozoff et al. 2003). There also have been noted increases in lightning and precipitation over a number of other urban areas,

including Chicago and Atlanta (Changnon 1980; Westcott 1995; Dixon and Mote 2003; Stallins et al. 2006).

2.3.2 *Houston UHI*

UHI effects have also been demonstrated over the Houston urban area. The mean UHI magnitude, taken from satellite skin temperatures during the early morning hours, of Houston from 1999-2001 was 3.19 ± 0.08 K (Struetker 2002). A UHI convection simulation by Orville et al. (2001) using a simple land surface parameterization demonstrated the importance of the Houston UHI on convergence. Convection formed over the area designated as urban due to the vertical circulation caused by higher urban temperatures. When Houston was removed from the simulation, convergence over the Houston area disappeared (Figure 2.1). Gauthier (2006) found that peak of the mean thermal anomaly over Houston existed from local noon to approximately 1500 CST. By isolating only days with UHI forcing, the UHI appeared to enhance the background climatology, and accounted for 25% of the mean lightning flash density. It was noted that peak enhancements occurred over the central northern and southern boundary of the city (Gauthier 2006). Steiger et al. (2002) and Shepherd and Burian (2003) speculated that UHI was mostly responsible for the lightning and rainfall anomaly due to the increase in the anomaly during the summer months, when UHI effects on mesoscale convergence is strongest.

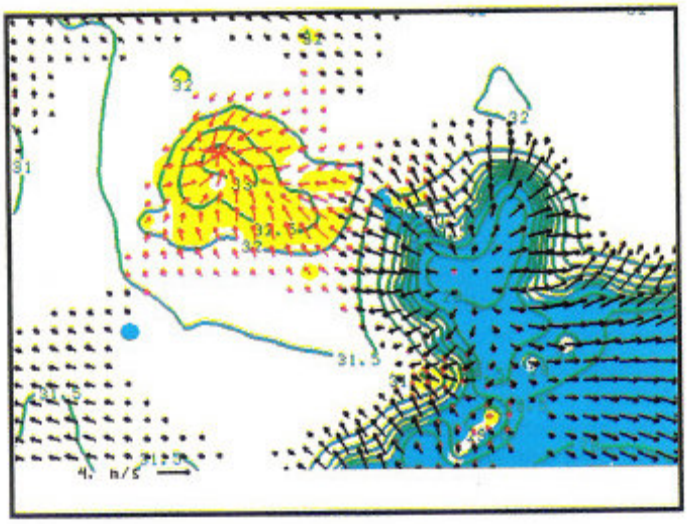

FIG. 2.1. Simulated UHI convergence over Houston (Orville et al. 2001).

2.4 *Lightning and Convective Intensity*

Lightning is created by complicated microphysical charging processes in a storm that are not well understood. A non-inductive charging process is the main theory used to explain electrification within a thunderstorm. This theory suggests that charge is separated on the particle scale during the rebounding collision of graupel particles with ice crystals in the presence of super-cooled water. Many laboratories studies have been done to identify the correlations between many environmental parameters found in thunderstorms and the charging of graupel. Takahashi (1978) found that graupel became negatively charged in temperatures lower than -10 °C, and that graupel is not highly electrified in high cloud water content. However, a study by Pereyra et al. (2000) found that when the graupel and super-cooled water drops were created in separate chambers, and then mixed, the graupel charges negative at higher values of cloud effective liquid

water content (EW) and graupel acquires a positive charge at low EW and at higher temperatures. A study by Saunders and Peck (1998) related the charging of graupel to rime accretion rate (RAR). The RAR = EW * V, where V is the graupel/crystal relative velocity. It was found that graupel becomes negatively charged at higher temperatures for lower RAR, and for higher RAR graupel charges positively. Avila et al. (1995) found that as the temperature difference increases between the ambient air and the graupel, negative charge transfer is more likely to occur. However, it was found that as the temperature difference continues to increase, the charge transfer will become positive. If the graupel is not rimed, the charge transfer will be mainly negative. A study on the effect of drop size found that a broad array of drops in temperatures above -20 °C increased the negative charge of graupel (Avila et al. 1998).

Since the storm scale separation of charge is dependent on the vertical draft structure and the relative difference in particle fall speeds (i.e., graupel – ice crystal), storm structure and life cycle are important variables in the production of CG lightning. The onset of CG lightning is believe to occur due to the descent of graupel below the negative charge center. Graupel will begin to descend once the updraft is no longer strong enough to support it. Williams et al. (1989) found that the decent of ice particles through the region of negative charge stimulated CG lightning. Reflectivity values of 45-60 dBZ have been shown to correlate with the presence of graupel based on polarimetric radar, and the descent of the reflectivity core below the freezing level correlated with the peak microburst, surface hail, and CG flash rate (Carey and Rutledge 1996). A correlation between CG lightning and rainfall was found by Carey and

Rutledge (2000). CG lightning was also associated with the descent of graupel from the -10 to -20°C region in their study. The correlation between reflectivity descent below the negative charge height and CG lightning is shown in Figure 2.2 from Williams et al. (1989).

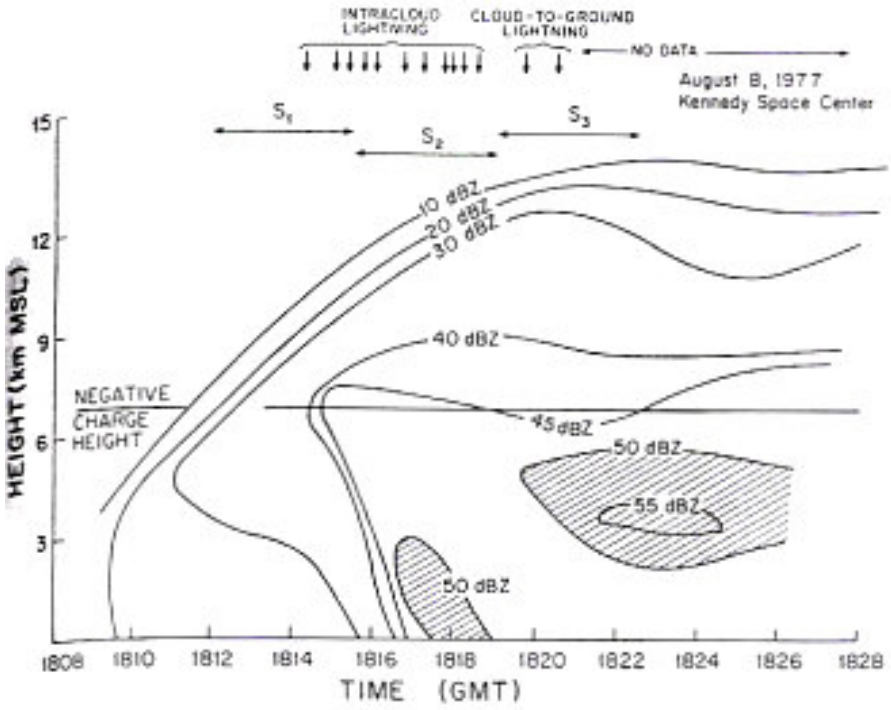

FIG. 2.2. Time-height evolution of a Florida thunderstorm (Williams et al. 1989).

2.5 *Hypothesis and Ancillary Questions*

Based on the previous studies, I hypothesize that low-level convergence is important for the modulation of convection frequency and intensity over and downwind of Houston

and hence likely plays a significant causative role in the formation of the Houston lightning and rainfall anomaly. Some specific questions to be addressed in this thesis are: Can the low-level convergence due to urban heat island and sea-breeze be resolved diurnally and which effect has the most influence on the anomaly? Do the areas of convergence correlate with the convection? Does the location of the lightning correlate with the reflectivity values of 30 dBZ or greater? Do the areas of convection and lightning correlate with the Houston anomaly identified in past studies and are they statistically significant from the surrounding domain?

The manner in which low-level convergence correlates to convection and convective intensity will be studied using boundary layer dual-Doppler data. The relationship between convective intensity and lightning will be analyzed using radar reflectivity and the National Lightning Detection Network (NLDN) CG lightning data. Finally, diurnal patterns will be analyzed to resolve possible sea-breeze and daytime heating effects and their relation to convection.

CHAPTER III

DATA AND METHODOLOGY

3.1 *Radars*

The following sections provide information on the radars, as well as the radar parameters and derived values obtained during the TEXAQSII study. The SMART-R in Houston (SR-1) first became available July 9th, 2005. The radar ran with approximately 6% down time until September 21st, 2005. The SMART-R in Dallas (SR-2) first became available July 18th, and continued until September 22nd, 2005 with approximately 3% down time. Down time for both radars was due to mechanical and technical issues, as well as time needed to re-fuel. Less than 1% down time was experienced by the KHGX National Weather Service Houston radar during the same time period as SR1, and less than 3% down time was experienced by KFWS National Weather Service radar in Dallas for the same time period as SR2.

3.1.1 *SMART-R*

The SMART Radars are a collaborative effort between the National Severe Storms Laboratory, Texas A&M University, Texas Tech University, and the University of Oklahoma. The radars are C-band 5-cm mobile Doppler radars mounted on flatbed trucks (Figure 3.1). The radars were deployed in areas appropriate for dual-Doppler synthesis and where few surface obstacles close to the radars would be present (see

section 3.2.3 for more details). The radars were deployed at La Porte Municipal Airport and Dallas Hensley Field for SR1 and SR2, respectively. Due to the location of the truck cabs, a 34° azimuthal sector of radar sampling was blanked out. The centers of these sectors correspond to approximately 180° for SR1 and approximately 240° for SR2. Scanning strategies and technical specifics for the SMART radars are presented in Table 3.1.

FIG. 3.1. Photograph of SR1. Truck cab represents area of beam blockage (Biggerstaff et al. 2005)

Table 3.1. SMART-R technical specifications from the final progress report to TCEQ by Carey (2005).

Item	**Description**
Wavelength	5.5 cm
Polarization	Linear Horizontal (H) Polarization
Recorded data fields	Horizontal reflectivity (Z_H) and Radial Velocity (V_R) [Doppler Spectral Width(σ_D) if desired]
Pulse Repetition Frequency (PRF) Unambiguous Velocity (Range)	1200 Hz 16.5 m s^{-1} (125 km)
Scan Type	330° Plan Position Indicator (PPI) radar sector volumes (i.e., varying azimuthal sweeps at multiple fixed elevation angles)
Number of Samples	64 pulses
Scan speed	15 deg s^{-1}
Fixed Elevation Angles	0.5, 1.5, 2.5, 3.5, 4.5, 6.0° (SR1)/ 1.0, 1.5, 2.0, 2.5, 3.5, 4.5, 6.0, 7.5° (SR2)
Scan Time	≈ 160 s (2.7 min)

The SR1 and SR2 boundary layer surveillance scans provided data approximately every three minutes. During convective times the scans were changed to precipitation mode. Precipitation volume scans covered narrow (120°) sectors centered on convective activity with a larger number of plan position indicators (PPI) up to higher elevation angles. During convective times, boundary layer surveillance scans were completed approximately every ten minutes.

3.1.2 *WSR-88D*

The Weather Surveillance Radar – 1988 Doppler (WSR-88D) S-Band Doppler radars are operated by the National Oceanic and Atmospheric Administration (NOAA) National

Weather Service (NWS). The Houston area radar, KHGX, is located in League City. The Dallas area radar, KFWS, is located in Fort Worth. At the time of the field deployment, the NWS utilized primarily three volume coverage patterns (VCP), depending on meteorological conditions. Table 3.2 highlights some basic technical specifications of the WSR-88D. Figure 3.2 is an image of the clear air mode VCP while Figures 3.3 and 3.4 are images of the precipitation and severe VCPs, respectively.

Table 3.2: WSR-88D technical specifications.

Item	Description
Wavelength	10.0 -11.1 cm
Pulse Frequency/Unambiguous Velocity	1014-1181/ 26.8- 31.2ms^{-1} (at 10 cm wavelength)
Pulse width	1.57 μs – 4.7μs
Scan Speed	36° s^{-1}

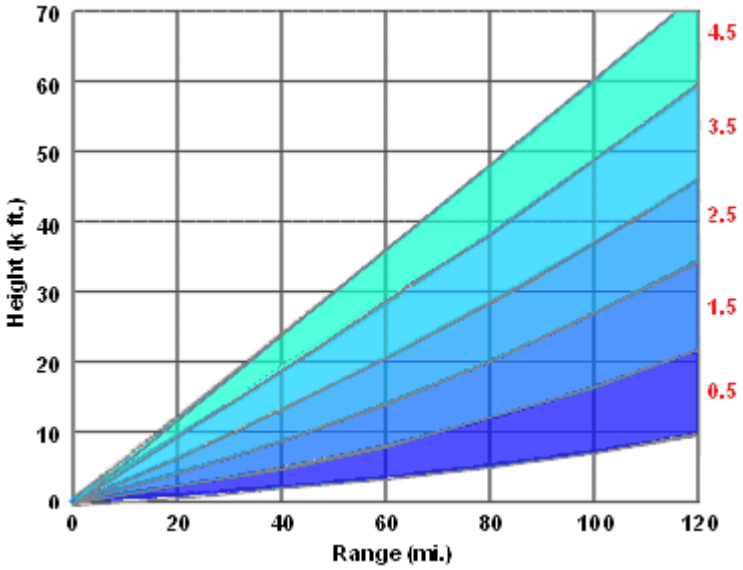

FIG. 3.2. WSR-88D clear air mode volume coverage pattern 31/32. (http://www.srh.noaa.gov/radar/radinfo/vcp31.html)

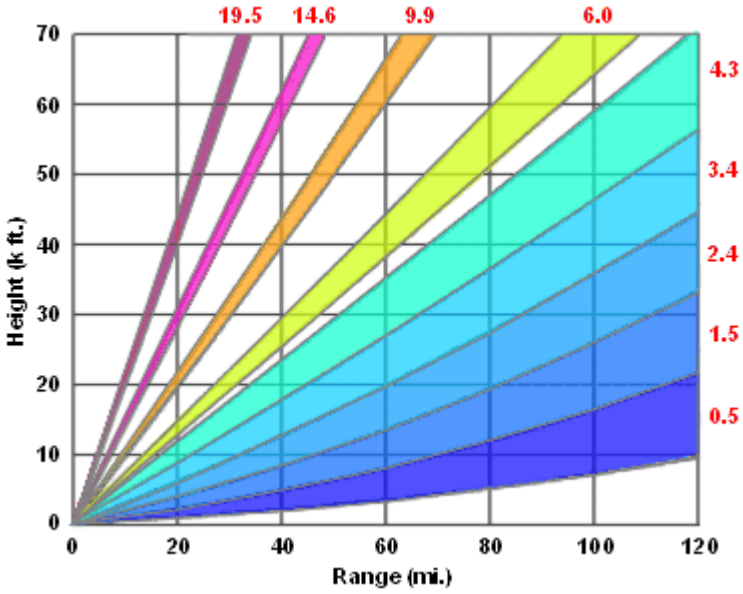

FIG. 3.3. WSR-88D precipitation volume coverage pattern 21. (http://www.srh.noaa.gov/radar/radinfo/vcp21.html)

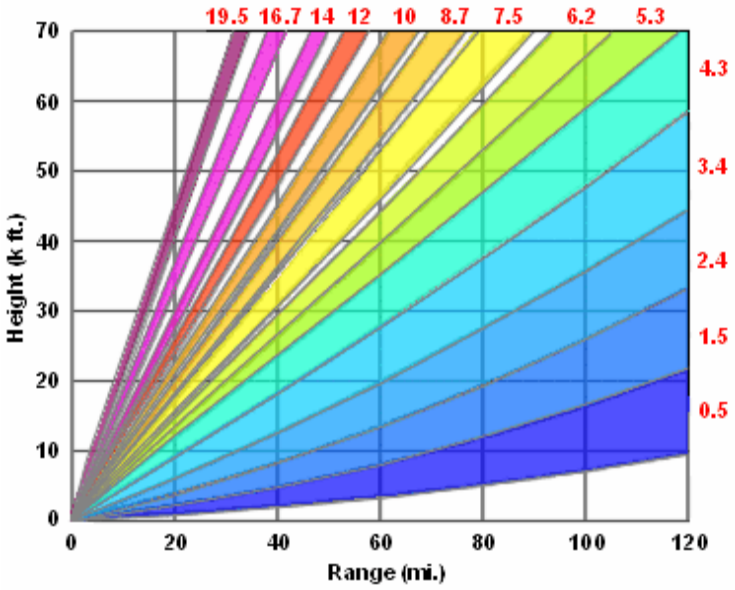

FIG. 3.4. WSR-88D precipitation volume coverage pattern 11. (http://www.srh.noaa.gov/radar/radinfo/vcp11.html)

Clear air scans have a slower rotational speed and this allows the radar to be more sensitive. Clear air scans are completed every ten minutes. Precipitation VCP 21 scans are used in the presence of convergence and are completed every six minutes. Severe mode VCP 11 scans are used during strong or severe weather and scans are completed every five minutes. WSR-88D data was received in near real-time through a Unidata Local Data Manager (LDM) in level II format. The LDM is software created by the University Corporation for Atmospheric Research (UCAR), which allows workstations to acquire meteorological data. Any missing data was retrieved through the National Climatic Data Center website, http://www.ncdc.noaa.gov/oa/radar/radarresources.html.

3.1.3 *Radar Parameters and Derived Values*

Reflectivity, Z, is a measure of the power returned to the radar from a backscattering target. Radars observe all types of scatters, be they precipitation, such as rain, snow, hail, etc., or non-meteorological. Most non-meteorological targets are observed as clear-air targets and caused by either particulates, such as biological scatterers, or refractive index gradients. When temperature or humidity changes are significant, but take place along the same size of the wavelength of the radar most likely due to turbulence, the radar can detect a clear-air echo. In the case of precipitation radars, any clear-air return is most likely particulates (Wilson et al. 1994). As discussed in section 2.1, insects serve as the primary source of radial radar retrieved winds.

In the computation of Z from radar observations, Rayleigh conditions are assumed. In order for Rayleigh conditions to be satisfied, the backscatter cross-section of the target, α, must be small compared to the wavelength of the radar. Assuming Rayleigh conditions apply, the radar reflectivity factor, z, can be computed using the equation:

$$z = \int_0^\infty N(D) D^6 dD \tag{3.1}$$

where D is the diameter of the target and N(D) is the number of drops of diameter D. Due to their size compared to the wavelength of the radar, insects are not considered Rayleigh targets. However, this is not an issue due to the fact that the reflectivity from insects is not used quantitatively. With the exception of large hail, precipitation targets meet Rayleigh conditions. Due to the sixth power dependence of the diameter, z

becomes very large for large targets. The radar reflectivity factor is usually translated into a logarithmic scale:

$$Z = 10log_{10}(z) \tag{3.2}$$

Radial velocity, Vr, is the velocity of an object in the radial direction, measured as either heading toward, or away from, the radar. Doppler velocity is based on the theory that a moving object will shift the frequency of the radar wave proportional to the speed with which it moves. The phase shift can be calculated from:

$$\phi = \phi_0 + \frac{4\pi r}{\lambda} \tag{3.3}$$

where ϕ_0 is the initial phase, and λ is the wavelength of the radar. The amount of phase shift between radar pulses is related to the frequency of the shift:

$$f = \frac{d\phi}{dt}\frac{1}{2\pi} \tag{3.4}$$

The radial component of the velocity (v) can then be found by:

$$V = \frac{f\lambda}{2\cos\alpha} \tag{3.5}$$

where α is the angle with which the target is moving relative to the beam angle of the radar. Depending on the wavelength of the radar, there is a maximum velocity that a radar can detect, also called the Nyquist velocity:

$$V_{\max} = \pm\frac{\lambda f_{\max}}{2} \tag{3.6}$$

The maximum frequency is the pulse repetition frequency (PRF) of the radar divided by two (e.g., Rinehart 2004). The Nyquist velocity for the SMART-R is 16.5 ms^{-1} (Table 1)

and is 28 ms^{-1} for the WSR-88D. Once velocities exceed the Nyquist velocity, velocity aliasing, or folding occurs. Folding appears as large magnitude velocities that are in the opposite radial direction of the nearby non-folded velocities. This produces anomalous velocities, which must be corrected in order to determine the correct winds. More discussion on how this was done will be described in section 3.2.

Spectrum width is a measure of the amount of velocity variability. Spectrum width is computed by finding the amount of velocity variance within a certain radar sample:

$$\sigma^2 = \frac{\sum (V_i - V_{ave})^2}{N-1} \tag{3.7}$$

where V_i is the velocity at any point, V_{ave} is the average velocity of the sample, and N is the number of points in the sample (Rinehart 2004). A low spectral width could indicate the presence of ground clutter.

Radar reflectivity is frequently used as a convenient method of estimating rainfall. Using radar to estimate rainfall has the advantage of high spatial resolution compared to rain gauges. Rain gauges are often spaced too far apart to be useful, or may not be present at all, especially when analyzing a specific area of interest. A Z-R relationship is used to compute the amount of rainfall from a radar sample. The default WSR-88D relationship is:

$$Z = 300R^{1.4} \tag{3.8}$$

where z is the radar reflectivity factor and R is the amount of rain (from the Federal Meteorology Handbook No. 11, http://www.ofcm.gov/fmh11/fmh11B.htm). The relationship:

$$Z = 250R^{1.2} \tag{3.9}$$

is used for tropical precipitation (Rosenfeld et al. 1993). Rainfall estimation by radar can be in error by a significant factor. The use of Z assumes a known drop size distribution. This is usually not the case due to the fact that drop size distribution can vary by a large amount temporally and spatially. The presence of mixed phase precipitation can present many problems, including multiple dielectric constants, various drop size diameters, and the presence of non-Rayleigh scatterers. Other problems associated with radar rainfall estimation include power calibration, attenuation, horizontal and vertical winds, the bright band, evaporation, beam blockage, ground clutter and anomalous propagation, incomplete beam filling, and large rain gradients and insufficient spatial resolution (e.g., Doviak and Zrnic 1993)

3.2 *Data Processing*

The data obtained from the SMART-R and WSR-88D data had to be translated from the radar coordinates (i.e., azimuth angle, elevation angle, range) in raw form, which are IRIS and Level II, respectively. This was done using the xltrsii data translator developed by the National Center for Atmospheric Research (NCAR). The data then had to be cleaned and unfolded, if necessary. In order for dual-Doppler processing to be done, the data were translated to Cartesian coordinates using the NCAR program REORDER (Oye and Case 1995). Dual-Doppler synthesis was done using the NCAR program Custom Editing and Display of Reduced Information in Cartesian space (CEDRIC) (Miller and Frederick 1998).

3.2.1 *XLTRSII and Cleaning Raw Data*

The xltrsii software is a binary program which translates the raw radar data into universal format (UF) or NCAR sweep format, which can be gridded using REORDER. The lowest two scans of the WSR-88D are completed twice using separate PRFs. The low PRF scan can cause an erroneous Nyquist velocity which is carried through the rest of the processing unless removed. Therefore, the low, duplicate PRF scan was removed using xltrsii.

From UF format, the SMART-R data was run through a Fortran program written by Larry Carey. This program read in the UF format, corrected the beam pointing angle, and applied thresholds to remove ground clutter. The pointing angle correction was needed to correct any heading error that occurred due to the radars mobile positioning. This correction was 2.3 degrees and 0.52 degrees for the SR1 and SR2, respectively. A radar sample with spectrum width less than 0.7 ms^{-1} or a velocity between -0.25 and .25 ms^{-1} was considered to be ground clutter and was removed. Thresholds were determined by finding a large enough value to adequately restrict ground artifacts while retaining most of the valid clear-air and precipitation data. No thresholding was done on the WSR-88D data as the National Weather Service already does a clutter mitigation scheme on all level II data to remove ground clutter and other artifacts in the data (Kessinger et al. 2004).

Due to the presence of birds located in the Houston dual-Doppler domain, it was necessary to determine if there existed practical ways to remove contaminated data.

Karl Schulze (2003) explored possible ways to remove bird contamination in his TAMU Master's thesis. Velocity signals were separated into two clusters, one for birds, and one for wind-carried targets. A best fit curve for each cluster was then found to differentiate the clusters objectively. One method was attempted by separating the clusters and running the currently used algorithm for the Velocity Azimuth Display (VAD) best fit curve for each cluster. Another method involves finding the minimum and maximum velocities and the variances near these points. The first method proved harder than the second due to ambiguity in identifying the different clusters, but both would take computational time and require further testing for possible errors.

Another method for removing contaminated velocities was suggested by Liu et al. (2004) and Zhang et al. (2005). This method involves creating three quality control parameters, mean reflectivity, velocity data coverage, and along-beam perturbation velocity sign changes. Birds enhance reflectivity, increase the area of velocities, and cause velocities to vary greatly gate to gate. The Bayes theorem was used to determine the probability of birds given each QC parameter. The Bayes theorem states that the probability of event A given event B can be found if the probability of event B given event A is known. By studying known bird cases, the probability of each QC parameter was found, and by using the Bayes theorem, the probability of birds given the QC parameters can be determined. If the probability of a contamination based on all three parameters was greater than 50%, then the sweep was marked as contaminated by birds. Using this method, 94.6% of contaminated sweeps were correctly identified. However, 37.2% of sweeps were falsely identified as contaminated. The methods suggested by

Liu et al. (2004) and Zhang et al. (2005) have not had much testing and both methods were tested using only one radar over only a single period of time and, therefore, may not work in different conditions. These methods would also take time and computational power to implement, beyond the scope of this thesis. The best option to remove birds in the future will most likely come with the conversion of the WSR-88D to polarimetry. The identification of birds and insects using polarimetric radar is described in Ryzhokov and Zrnic (1998), and the use of differential phase to remove ground clutter, including birds, is described in Zrnic et al. (2006).

A large number of Purple Martins roost just south of I-10, between Gessner and Sam Houston Toll way[1]. It was found that in this location, up to 100,000 Purple Martins may roost[2]. Near sunrise, birds take off from roost, producing a diverging donut type reflectivity feature (Figure 3.5). Near sunset, birds tend to appear as a "cloud" of reflectivity at approximately the same location (Figure 3.6). This pattern is consistent with purple martins as described in Russell and Gauthreaux (1998). The typical flight configuration for sunrise and sunset from Russell and Gauthreaux (1998) is presented in Figure 3.7. Also, bird migration during the early fall months occurs southwardly along the Houston coast shortly after sunset until sunrise (Schulze 2003). Nothing was done to remove the presence of birds in reflectivity. However, times in which the birds are present are known and the presence of birds is considered when taking into account any ambiguities. Any bird contamination was taken note of, but no attempt was made to

[1]www.houstonaudubon.org/index.cfm/act/newsletter.cfm/newsletterid1247/catergory/Bird%20Gallery/MenuGroup/Home/htm

[2] www.users.stargate.net/~jhill/roost/roost.html

remove it prior to the validation. For the computation of average convergence and average horizontal winds used in the analysis, outliers were computed to remove possible contamination due to birds and other artifacts. The method that outliers were removed will be discussed in section 3.4.4.

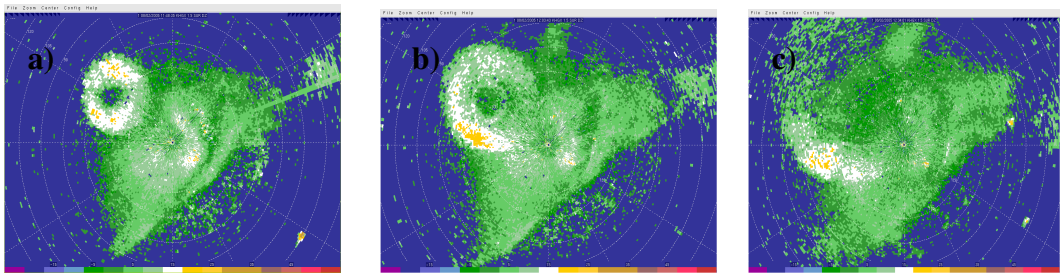

FIG. 3.5. SR1 reflectivities showing bird contamination near sunrise. Reflectivities are from 1148Z (a), 1220Z (b), and 1233Z (c).

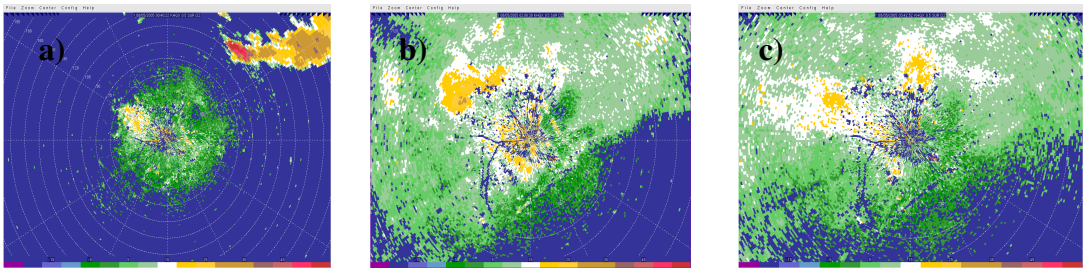

FIG. 3.6. SR1 reflectivities showing bird contamination near sunset. Reflectivities are from 0040Z (a), 0151Z (b), and 0342Z (c).

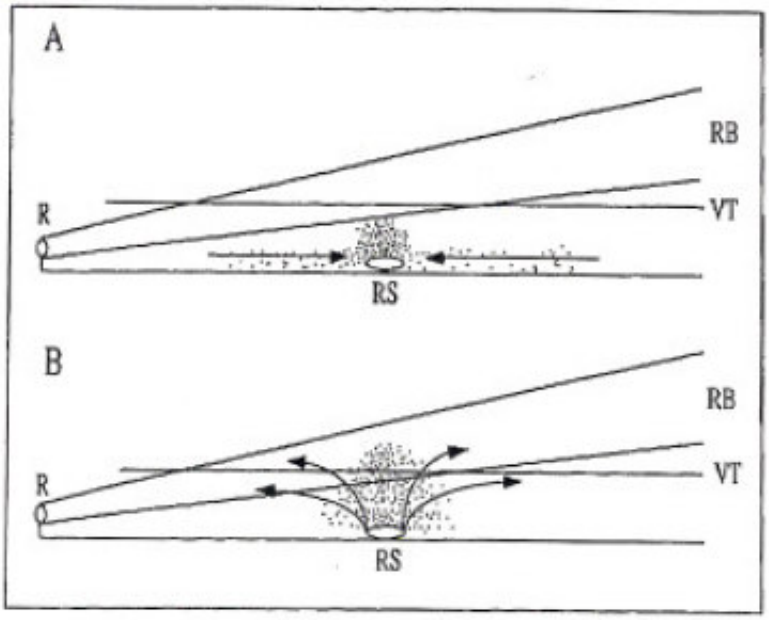

FIG. 3.7. Cartoon depicting birds returning to roost near sunset (A) and taking off from flight at sunrise (B). R is the radar, RB is the radar beam coverage, RS is the roost site, and VT is the visual observation threshold (Russell and Gauthreaux 1998).

3.2.2 *REORDER*

REORDER grids the UF or NCAR sweep data by interpolating the polar radar coordinates into Cartesian Coordinates. Grid spacing and the radii of influence are subjective based on the scanning strategy and needs of the user. To meet requirements set by the Texas Commission on Environmental Quality (TCEQ), grid spacing was 2 kilometers in the horizontal and 200 meters in the vertical with a maximum grid level of 2 km. Horizontal radii, dX and dY, and a vertical radius, dZ, of influence of 2 km and 400 m, respectively, were used. A Cressman weighting scheme was applied to interpolate each grid point (Cressman 1959). A Cressman weighting scheme applies

more significance to radar values close to the calculated grid point. It is a function of the radii of influence, R, and the distance of the grid point to the radar gate, r:

$$R^2 = dX^2 + dY^2 + dZ^2 \tag{3.10}$$

$$W = \frac{R^2 - r^2}{R^2 + r^2} \tag{3.11}$$

Grids of 1 km horizontal spacing, 200 m vertical spacing with up to 2 km above ground level, 1 km horizontal radius of influence, and 400 m vertical radius of influence were made for convergence and wind maps. The 1 km x 1 km horizontal grid spacing was chosen to increase data resolution. The vertical grid spacing and radius of influence were chosen to avoid sampling outside of the boundary layer while providing adequate horizontal coverage of the Houston area. Grids of 1 km horizontal and vertical resolution up to 10 km altitude with 1 km horizontal and vertical radii of influence were made for radar reflectivity analysis of precipitation features. The larger vertical radius of influence, grid spacing, and maximum grid level were chosen to increase vertical data coverage to retrieve convective reflectivity values aloft. All maps had a grid size of 60 X 60 km. Local radial velocity unfolding was done using REORDER (Miller et al. 1986).

3.2.3 *Dual-Doppler Derived Winds*

The positioning of two radars in proximity to one another allows two-dimensional winds to be computed as described in Armijo (1969). The baseline between radars affects data resolution and range. Davies-Jones (1979) shows that for a large baseline

range and coverage areas are increased, while data resolution is decreased. The distance between SR1 and KHGX (SR2 and KFWS) is approximately 22 (37) kilometers. For typical boundary layer depths and minimum radar elevation angles discussed earlier, the dual-Doppler lobes are confined to an area within approximately 60 kilometers of the radar to avoid sampling outside of the boundary layer (Figure 3.8). Furthermore, the sensitivity of SMART-R and WSR-88D to clear-air signatures is typically limited in range to about 60 km, regardless of boundary layer depth.

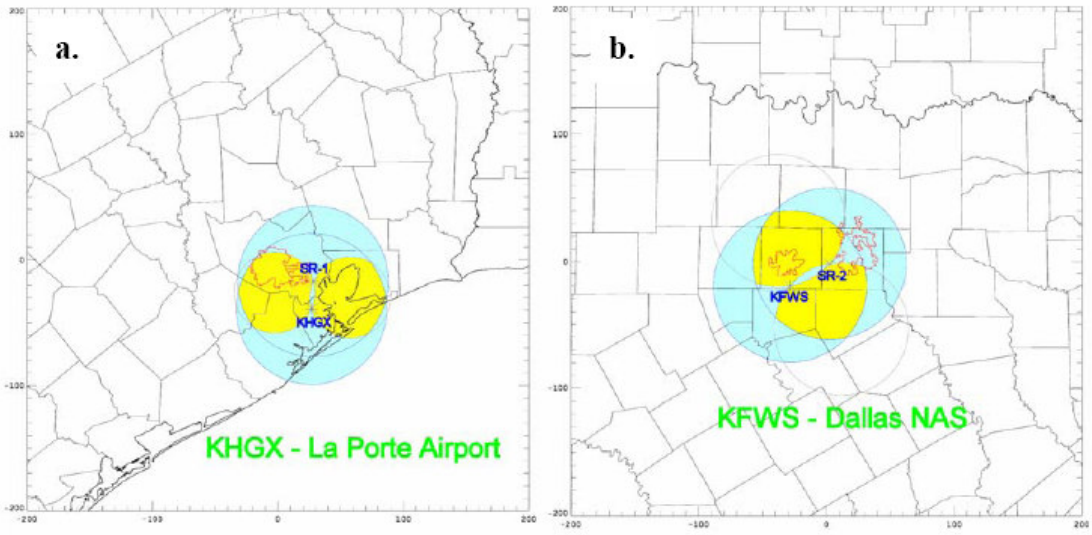

FIG. 3.8. Dual-Doppler lobes from final report to TCEQ by Larry Carey. Yellow areas indicate dual-Doppler lobes. The blue circles are single Doppler sampling area within 60 kilometers of the radar.

The beam-crossing angle, β, between the two radar beams is related to the error variance of the u and v components of the wind, σ_u and σ_v, and the error variances of the radars, σ_1 and σ_2 (Lhermitte and Miller 1970):

$$\frac{\sigma_u^2 + \sigma_v^2}{\sigma_1^2 + \sigma_2^2} = \csc^2 \beta \tag{3.12}$$

A beam-crossing angle of greater than about 20° to 30° represents acceptable error variance while a beam-crossing angle of 90 degrees is ideal (Davies-Jones 1979). A 20 degree beam-crossing angle threshold was chosen for this thesis to maximize the area of winds while maintaining acceptable error variances.

The program CEDRIC was used to derive the dual-Doppler winds from the Cartesian outputs produced by REORDER. After Cartesian coordinates are found, the radial velocity, $\hat{v}_r$, at location x, y, and z, can then be related to the u, v, and w components of the wind:

$$\frac{[\hat{v}_r\, r]_t + \Delta t}{[r]_t} = \left[\hat{u}\left(\frac{x - x_0 + U\Delta t}{r} \right) + \hat{v}\left(\frac{y - y_0 + V\Delta t}{r} \right) + \hat{W}\left(\frac{z - z_0}{r} \right) \right]_t \tag{3.13}$$

where r is the slant range of the radar with a radar location of x_0, y_0, and z_0:

$$r = \left[(x - x_0)^2 + (y - y_0)^2 + (z - z_0)^2 \right]^{\frac{1}{2}} \tag{3.14}$$

$\hat{W}$ from equation 3.13 is a combination of the vertical velocity as well as the precipitation fall speed, t is the time of the sample, and Δt is the sample duration. When only two radars take measurements, w must be calculated using the mass continuity equation:

$$\frac{\partial(\rho\omega)}{\partial z}+\frac{\partial(\rho u)}{\partial x}+\frac{\partial(\rho v)}{\partial y}=0 \tag{3.15}$$

where ρ is density, and u, υ, and ω the horizontal and vertical wind components. By setting a boundary condition, equation 3.15 can be integrated to compute the vertical velocity (Miller and Fredrick 1998). In clear-air conditions, it can be assumed that the vertical velocity near the surface is zero. The zero vertical velocity can be used as a boundary condition for upward integration. Therefore, for the purpose of this thesis, upward integration was used with a boundary layer condition of a fraction of the calculated divergence. The precipitation fall speed and storm motion fields were set to zero to reflect clear air conditions. While some scans have precipitation present, this will not adversely affect the horizontal wind results. The horizontal winds are affected by the vertical velocity by w * sinα, where w is the vertical velocity and α is the elevation angle of the radar. The horizontal convergence and winds were calculated using the lowest elevation radar scans. Therefore, the presence of precipitation with non-negligible fall speeds will introduce only negligible error to the horizontal convergence and wind fields due to the sinα dependence of the associated error.

Once u and v values were found at all levels, the divergence could be calculated:

$$\nabla \bullet V=\frac{\partial u}{\partial x}+\frac{\partial v}{\partial y} \tag{3.16}$$

Convergence is simply the negative of the divergence. Global unfolding was completed in CEDRIC (Mohr and Miller 1983). New u, v, w, and convergence values were output in the form of netCDF.

3.2.4 *National Lightning Detection Network*

The National Lightning Detection Network (NLDN) is the primary source of cloud-to-ground (CG) lightning data for research and the NWS. The network consists of 106 sensors located around the United States which detect time, direction of arrival, and location of the lightning strokes (Cummins et al. 1998). The network detects peak currents of 4-5 kA or larger. A validation done in the upper Texas/Oklahoma region revealed median location accuracy of 282 m, and a stroke detection efficiency of 85% (Cummins et al. 2006).

3.3 *Validation of Dual-Doppler Derived Winds*

Dual-Doppler derived low-level horizontal wind maps for all of the data were created for TCEQ during the winter of 2005-2006. For the Houston area, maps were made at 400 meters above the surface. Due to a higher initial scan by SR2, maps for Dallas were made at 600 meters above the surface. An Interactive Data Language (IDL) program was used to compute the magnitude and direction of the horizontal winds at each grid point from the u and v components that were output by CEDRIC. The magnitude of each grid point can be expressed as:

$$mag = \sqrt{u^2 + v^2} \tag{3.17}$$

and the direction as:

$$\text{dir} = \arctan(v, u) \tag{3.18}$$

Dual-Doppler derived horizontal winds were compared to surface stations, rawinsonde data for Dallas, and profiler data for Houston. Though it will not be used further in this study, Dallas and Fort Worth area data were used for validation to expand the confidence in the methodology of the dual-Doppler analysis for inferring boundary layer winds using clear-air targets. Surface station data were gathered from the Meteorological Assimilation Data Ingest System (MADIS)[3] which posts private, government, including national weather service automated and manual stations and port data, and public data. Rawinsonde data was obtained from the University of Wyoming Department of Atmospheric Science web page[4]. Wind profiler data was gathered from the Cooperative Agency Profilers (CAP)[5]. Due to the large amount of possible data points, a subset of times had to be analyzed. In order to make the selection of the days and hours used for the analysis, a random number generator in EXCEL was used. For each day selected, a three hour time span was analyzed in increments of 15 minutes. Different dates and times were analyzed for Dallas and Houston.

Randomly chosen times for Houston resulted in a sample size of 54 hours distributed across 17 different days over the course of the summer. Four days were in July, eight in August, and five in September. Twenty-nine of the hours were before noon, and twenty-five were after. This sample resulted in 1196 data points for wind speed, and 986 data points for wind direction. For Dallas validation, ten total days were chosen over the summer resulting in a sample size of 30 hours. Four days were in July, three in August,

[3] http://www.madis-fsl.org/public/sfcdumpguest.html
[4] http://weather.uwyo.edu/upperair/sounding.html
[5] http://www.profiler.noaa.gov/cap/

and three in September. Fifteen hours occurred before noon, and fifteen after. The total number of surface data points gathered was 1162 for wind speed, and 1071 for wind direction. The difference in wind and direction data sample size occurred due to days in which the wind speed was zero, and there were no measurable wind gusts, therefore, wind direction could not be determined.

Upper air comparisons were done using the Dallas rawinsonde sounding and the La Porte profiler over Houston. The closest rawinsonde reading, within 100 meters, to the grid height of 600 meters was used for the comparison. Rawinsonde data were collected every 12 hours, at 0Z and 12Z, with the exception of some days during the end of August and September, most likely due to the approaching hurricanes Katrina and Rita, in which data was also collected at 6Z and 18Z. All possible data points were used for this comparison, totaling 133 points. The LaPorte profiler averaged thirty minutes of samples which were about five minutes in duration. This resulted in an averaging of about five or six samples, starting thirty minutes before the hour and ending on the hour. In order to compare the winds as accurately as possible, thirty minute averaging of dual-Doppler winds were also done, using the same times as the profiler. The profiler was located within 30-50 meters of the SMART-R and therefore not ideal for comparison. The SMART-R has limited ability to detect targets that are elevated in height and close to the radar due to beam angle elevation. It is likely that grid points close to the radar are more in error than grid points further from the radar. Due to the profiler's proximity to the SMART-R, averages of the twelve closest grid points were used. Every three hours was used for comparison every day available for the course of the project. There

was a gap of seven days from August 17 to August 23 where profiler data was not available. The total number of comparison points gathered was 425. The closest profiler height level to 400 meters was used for the comparison. This comparison is reasonable because under quiescent conditions, winds do not vary much within small spatial ranges.

In order to compare grid points to surface and upper air measurements, the latitude and longitude of each station were converted into grid coordinates. The closest computed wind vector on the grid was found to be used for comparison. Differences in speed and direction were calculated from the two by subtracting the measured wind values from the derived wind values. Statistics of the differences were calculated for all platforms, and histograms were created. For statistical purposes, the surface or upper air measurement values were considered "truth". Relative errors were also found. To avoid a division by zero, "truth" in the relative errors was taken as the average of the measured wind speeds and the derived wind speeds.

The average differences versus time were plotted, and plots were created of the average speed and direction difference versus range and beam-crossing angle. Student's t-tests were done on speed and direction difference for the profiler and sounding, to statistically prove the validity of the data and to check for any biases. The Student's t-tests were done on the hypothesis of no difference in mean between the dual-Doppler calculated winds and the profiler (sounding) for both speed and direction.

Speed difference versus wind speed and direction difference versus wind speed were plotted for the sounding and profiler data comparisons to resolve if differences between wind speed and wind direction varied with increasing or decreasing wind speed.

3.4 *Averages and Counts*

Using the processed radar data described in section 3.2 and the NLDN data described in section 3.3, averages of reflectivity, rain, lightning, convergence, and dual-Doppler horizontal winds were created. Only days that were missing no more than an hour of data were used. Therefore, 56 days were used in the analysis, 15 days from July, 29 from August, and 12 from September of 2005. Diurnal averages were done for each hour of every day by reading in the netCDFs which fell in an hour time span. For example, the 19Z average would include all files between 1900Z to 1959Z. A total average was done which takes in all time periods for the entire 56 days.

3.4.1 *Reflectivity*

Reflectivity was averaged at 2 km above ground level (AGL) and 7 km AGL using the KHGX radar. This radar was chosen due to its clutter mitigation scheme and complete domain coverage. Only reflectivity values over 20 dBZ were used for the average largely removing any clear air signal in the averaging. Due to this, some higher reflectivities can be caused by a single event. The gridded reflectivities from the CEDRIC output were used for the images and averaging. Averages were taken by first converting the dBZ to the linear reflectivity factor, z. For each grid point, the reflectivities were added if they were greater than 20 dBZ, and the number of times this occurred was counted. After all netCDF files were read, the total value z was divided by the count to give an average reflectivity, which was then converted to dBZ using 3.2.

The total reflectivity averages at 2km were made for all hours using the same algorithm as the hourly plots but only for reflectivities over 30 dBZ. This removes any fair weather and non-meteorological scatterers from the average which would affect the long term average. This was not needed for the 7km reflectivity average due to the lack of low reflectivities at 7 km.

At 2 km, the amount of times the dBZ was greater than 20 was counted and mapped. For the hourly images, the counts were plotted as a percentage of total files, and a total count encompassing all times was plotted. To examine if lightning is correlated with areas of enhanced reflectivity (Carey and Rutledge 1996), counts of the number of times the reflectivity exceeded 30 dBZ at 7 km were plotted for both the hourly and total images. A count instead of a percentage was used at 7 km due to the comparison with the lightning data. The counts will be used as an indicator of convective strength in addition to an indicator of convective frequency. Reflectivities greater than 40 dBZ have been correlated with the presence of lightning (Larsen and Stansbury 1974, Marshall and Radhakant 1978, and Carey and Rutledge 1996). However, 30 dBZ was chosen due to Houston's semi-tropical climate which could result in less mixed phase clouds and fewer occurrences of high reflectivity values. The height of 7 km was chosen due to its proximity to the -10°C isotherm, near the Houston area, and hence potential correlation with negatively charged graupel according to the non-inductive charging mechanism discussed earlier (Takahashi 1978).

3.4.2 *Rain*

Average hourly and total hourly cumulative rainfall images were created using the 2 km reflectivity. Once again, only dBZ greater than 20 were averaged. First, dBZ was converted to the linear reflectivity factor, z. The tropical rainfall equation (3.9) was used due to Houston's sub-tropical location. A rainfall rate was then calculated for each netCDF file. A centered time step strategy was used to compute rain amounts from the reflectivity. The rain rate for a given while was multiplied by the time given by the time between the file and the previous file and the file and the following file. For the first file of the hour read, the initial time was considered to be 0 minutes, and for the last file of the hour read, the final time was considered to be 60 minutes. Each period of time was multiplied by the rainfall rate to give a rainfall amount. For the entire span of the hour, each rainfall amount was added together to give a total rainfall amount for the hour. Each day's hourly rainfall totals at a given grid point were added and then divided by the number of times rainfall was greater than 0. For the total average cumulative rainfall the same was done, but for all hours of every day and for dBZ greater than 30. This was done to avoid averaging large values of low reflectivities that would result from the presence of cumulus or other non-precipitating clouds over the larger time span.

3.4.3 *Lightning*

Lightning data was gathered from the NLDN network. Due to the possible large spatial error in lightning accuracy of up to 500 m (Cummins et al. 1998) and point nature of ground flashes, a box filter approach (Kelly et al. 1978) was used to smooth the data.

Lightning data was added for each hour in 2 X 2 grid box at each 1 km grid spacing used in the REORDER analysis. This value was divided by 4 km^2 to give a lightning density per km^2. This was done for each 1 km grid spacing. This created lightning density maps which were comparable to the averaged reflectivity. The total lightning count was then divided by 56, the number of days in the analysis, to give hourly average lightning. The same technique was used for the total average lightning, resulting in a daily average lightning map.

3.4.4 *Horizontal Convergence and Winds*

Hourly average maps of both horizontal convergence and winds were created at the 200 meter level. An outlier rejection technique was used to remove potentially contaminated wind data in the boundary layer. Horizontal convergence and winds were filtered by removing any wind vector in which either the u wind component or v wind component that occurs in the 25^{th} percentile or in the 75^{th} percentile. This large rejection region was used due to the large amount of variability present at the boundaries of the dual-Doppler lobes and also in the areas identified as erroneous. This was done locally by creating a box around a grid point and computing statistics for that box. Also, a global wind magnitude filter was applied by removing any magnitude greater than the third quartile of the entire data set for the hour. Convergence was averaged for each hour by adding all the good data values for every day at that hour and dividing by the number of good points. The same was done for a total convergence map. The same procedure was done on the u and v components of the wind vectors to average winds.

The averages were used to compute magnitude and direction (see equations 3.17 and 3.18). Only every other wind vector was plotted to make the vectors more visible. A total average wind map was not created.

3.4.5 *Statistics*

For each averaged map, with the exception of the hourly averaged winds, statistics were done on select areas of the grid and the entire domain. Three areas were chosen due to their potential maximum in convective activity, while one was chosen due to its potential minimum in convective activity. Areas with expected maxima in convective activity were directly over Houston, downwind of Houston, and south of Houston, east of the bay. The box chosen with an anticipated minimum in convective activity was directly over the Galveston Bay. Figure 3.9 presents a graphical example of the domains. Each box was made to be 900 km^2. Averages of each box and a domain average were found for each time. However, additional domain and box means were was used for wind convergence that subjectively excluded known bird contamination regions in addition to the normally computed domain and box mean. Due to the consistency in the size of the bird anomaly, a smaller box within the big box and domain was removed from the average, and a new average computed. To compute the statistical significance of each box compared to the domain mean a Wilcoxon Rank-Sum test at the 95% level of significance was used. This was preferable to the Student's t-test due to the non-normal distribution of the data. Results of not significant, significantly greater, or significantly less were gathered between the averages in each box and the domain.

Graphs of the domain and box averages were made. Time series plots of the hourly averages over each grid box and domain were created to resolve diurnal variability. In order to remove possible bird contamination, a small box was not used to calculate the averages for the convergence images. The results of with and without the bird data were included in the time series plot for comparison.

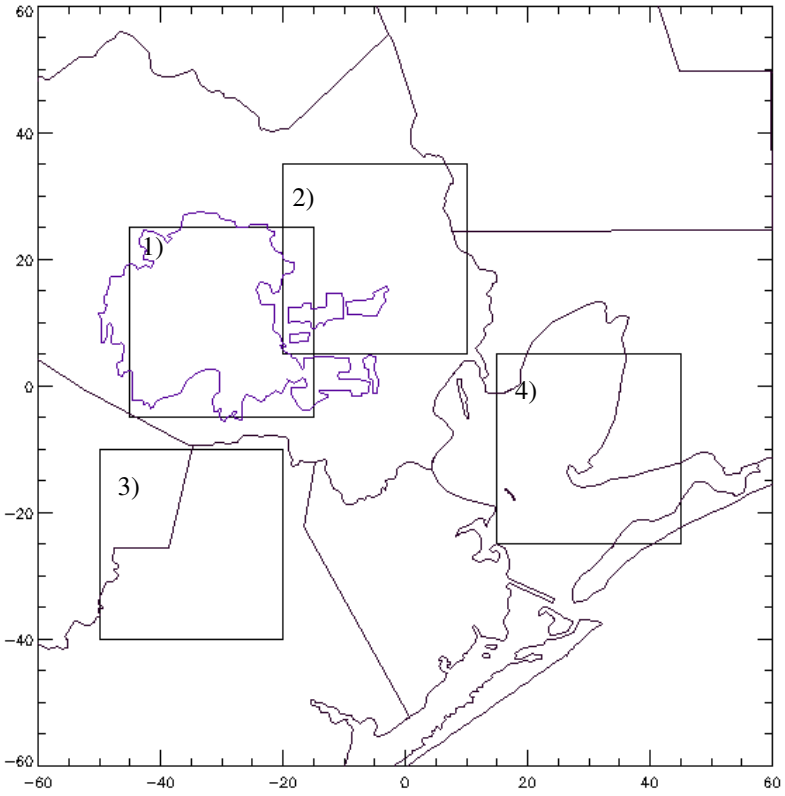

FIG. 3.9. Graphical representation of the domain and statistical boxes.

CHAPTER IV

RESULTS

4.1 *Performance of Dual-Doppler Winds*

The next sections will examine the validity of the boundary layer winds derived from the dual-Doppler retrieval from so-called clear-air echo. The gridded winds will be compared to winds from surface stations, rawinsonde in Dallas, and the La Porte wind profiler in Houston. Statistics used to compare the two data will be presented and a discussion on the results and the suitability of the data for scientific use will follow.

4.1.1 *Surface Station and Dual-Doppler Wind Analysis*

Histograms of the speed (a) and direction (b) differences between the gridded winds and the surface stations' winds are presented for Houston (Figure 4.1) and Dallas (Figure 4.2). A positive (negative) difference in speed indicates the dual-Doppler synthesis produced faster (slower) winds than the comparing instrument. A positive (negative) difference in direction indicates that the dual-Doppler synthesis was more clockwise (counter-clock wise) than the surface station. The mean, median, and standard deviations of the differences for wind speed and direction for both Houston and Dallas are presented in Table 4.1.

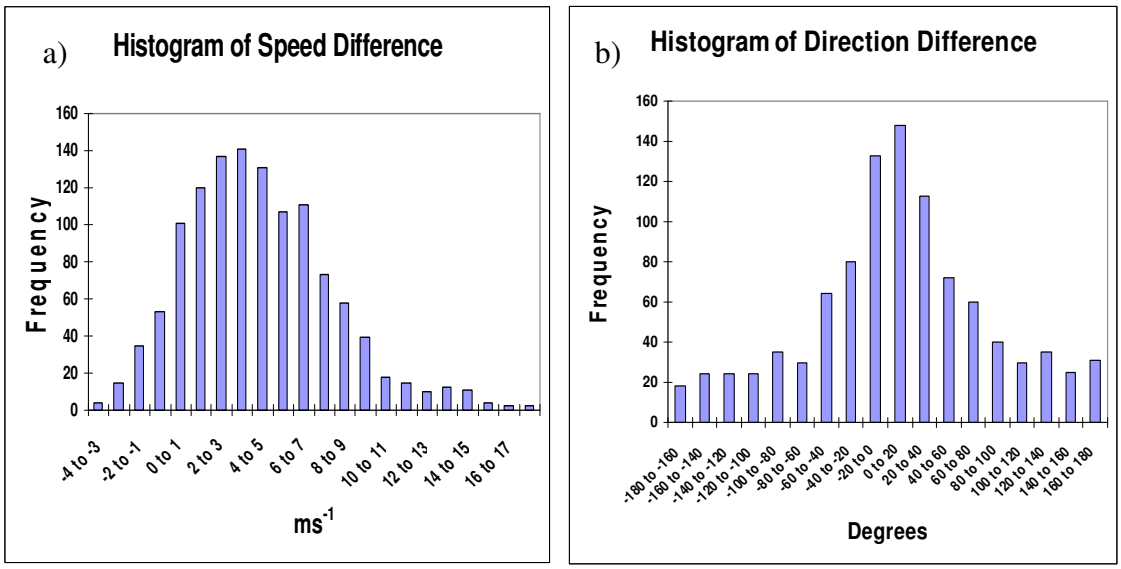

FIG. 4.1. Histogram of surface station wind speed (a) and direction (b) differences for Houston.

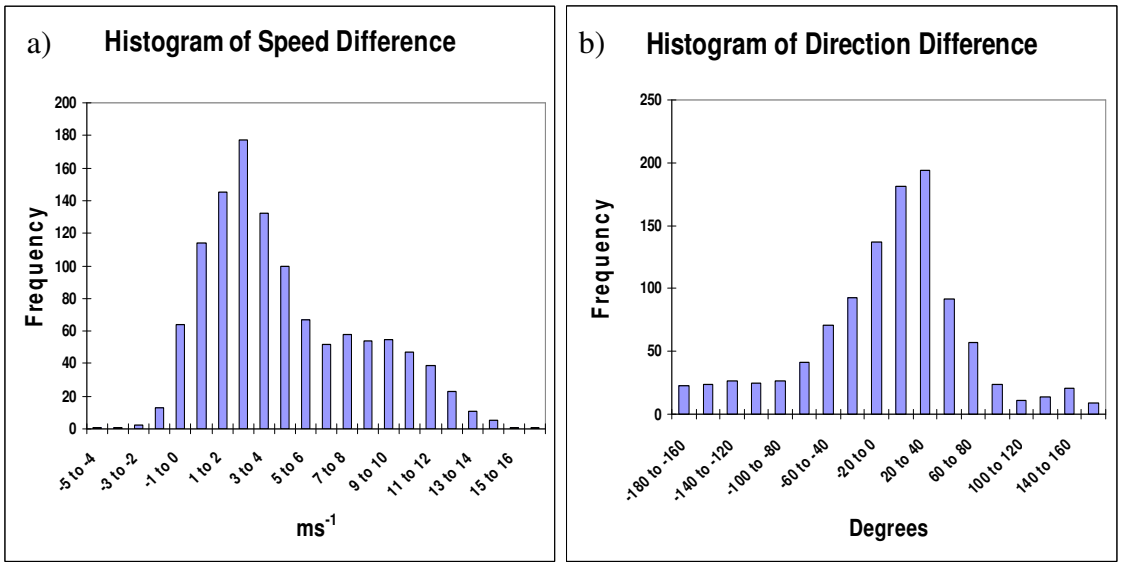

FIG. 4.2. Histogram of surface station wind speed (a) and direction (b) differences for Dallas.

Table 4.1. Difference statistics for surface and dual-Doppler comparisons.

Instrument	Median	Mean	St. Dev.	Relative Error Median	Relative Error Mean	Relative St. Dev.
Speed Houston Surface (ms^{-1})	3.97	4.36	3.59	1.65	1.31	0.81
Speed Dallas surface (ms^{-1})	3.45	4.43	3.72	1.1	1.09	0.71
Direction Houston Surface (degrees)	9.38	9.04	75.91	X	X	X
Direction Dallas Surface (degrees)	7.2	-0.38	66.03	X	X	X

The location of each surface station in regards to the beam-crossing angle and range from the radar modulates an error in the grid interpolated winds. Error associated with beam-crossing is related to the error variance (Eq. 3.12). Range increases the error due to the decreasing spatial resolution and increasing beam-height with distance. Figure 4.3 (Figure 4.4) shows the locations of the surface stations for range (a) and beam-crossing angle (b) for the Houston (Dallas) area. Bar-graphs for speed and direction differences vs. range (a) and beam-crossing angle (b) for Houston (Dallas) are presented in Figure 4.5 (Figure 4.6). To account for influences due to both beam-crossing angle and range, a multiple regression relationship was computed. By using a multiple regression, one equation can be found for the influence of multiple independent variables (range and beam-crossing) on a single dependent variable (speed or direction). The r^2 values for wind speed and direction for the Houston surface stations are 0.44 and 0.09, and the r^2 values are 0.11 and 0.29 for Dallas. Absolute speed (a) and direction (b) differences

versus time were plotted for both Houston (Figure 4.7) and Dallas (Figure 4.8). Data was averaged over the course of every day that data was compared. For example, the data in the 18 LST (local standard time) column contains any data from 1800 LST to 1859 LST.

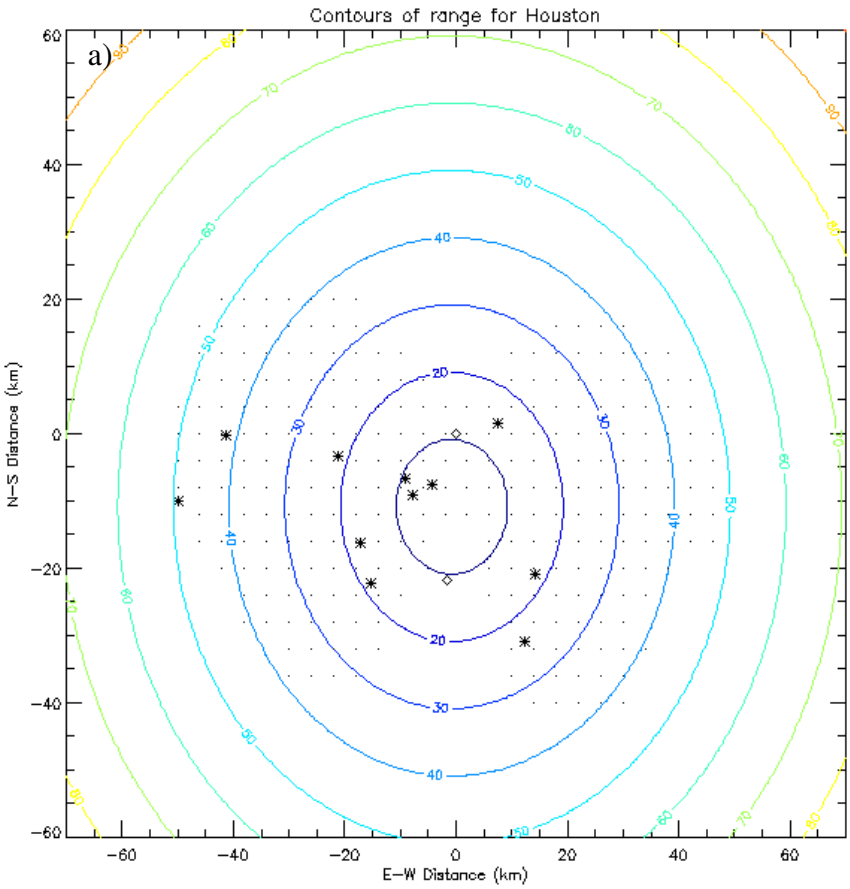

FIG. 4.3. Contours of range and beam-crossing angle for Houston centered on SR1. (a) Range is contoured every 10 km starting at 10 km and is measured from the center of the baseline. Dots indicate the approximate dual-Doppler lobes, asterisks indicate the surface stations, and diamonds indicate the radar locations. The location of the profiler is not plotted due to its proximity to SR1.

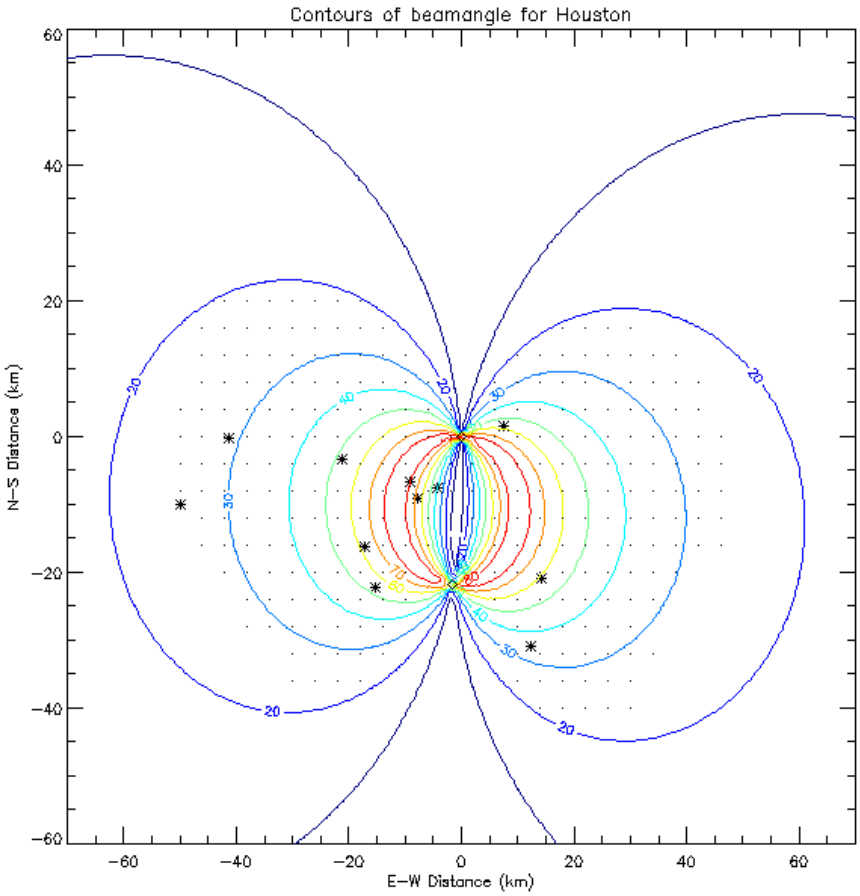

FIG. 4.3. cont. (b) Beam-angle is contoured every 10 degrees, blue is 10 degrees and red is 90 degrees. Dots indicate the approximate dual-Doppler lobes, asterisks indicate the surface stations, and diamonds indicate the radar locations. The location of the profiler is not plotted due to its proximity to SR1.

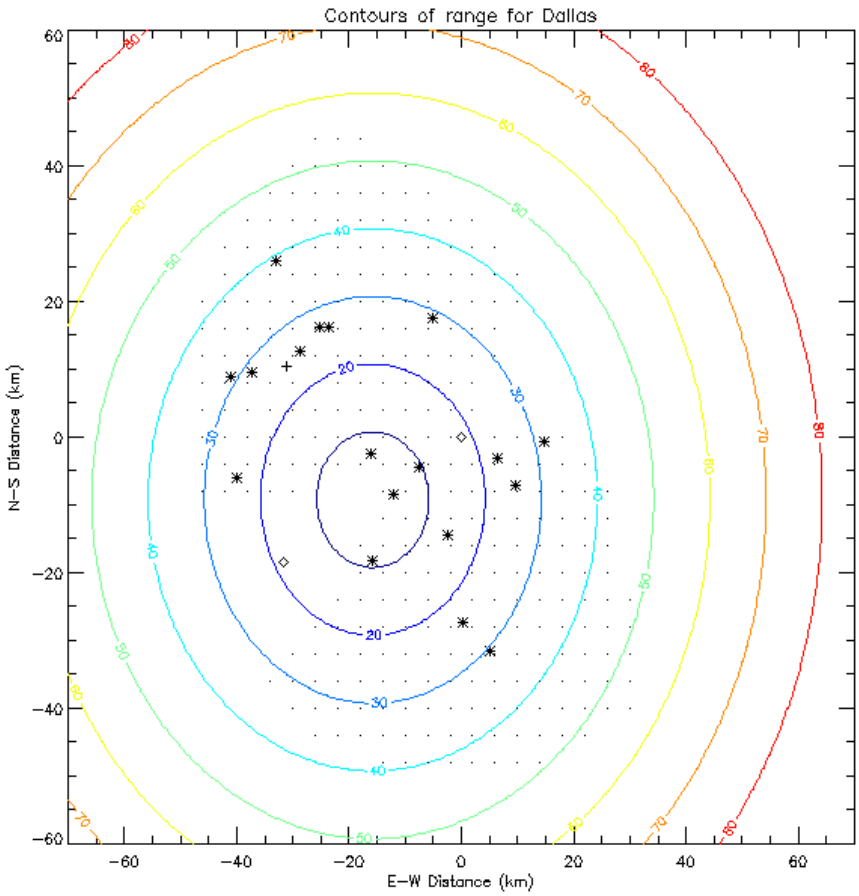

FIG. 4.4. Contours of range and beam-crossing angle for Dallas centered on SR2. (a) Range is contoured every 10 km starting at 10 km and is measured from the center of the baseline. Dots indicate the approximate dual-Doppler lobes, asterisks indicate the surface stations, the plus indicates the rawinsonde location, and diamonds indicate the radar locations.

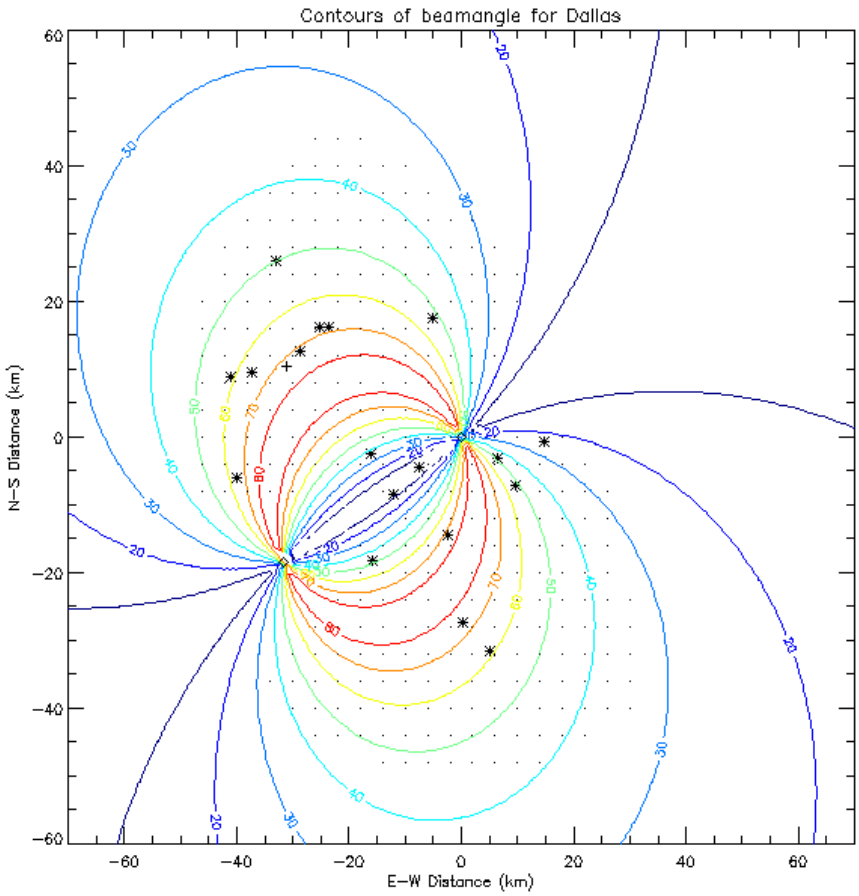

FIG. 4.4 cont. (b) Beam-angle is contoured every 10 degrees, blue is 10 degrees and red is 90 degrees. Dots indicate the approximate dual-Doppler lobes, asterisks indicate the surface stations, the plus indicates the rawinsonde location, and diamonds indicate the radar locations.

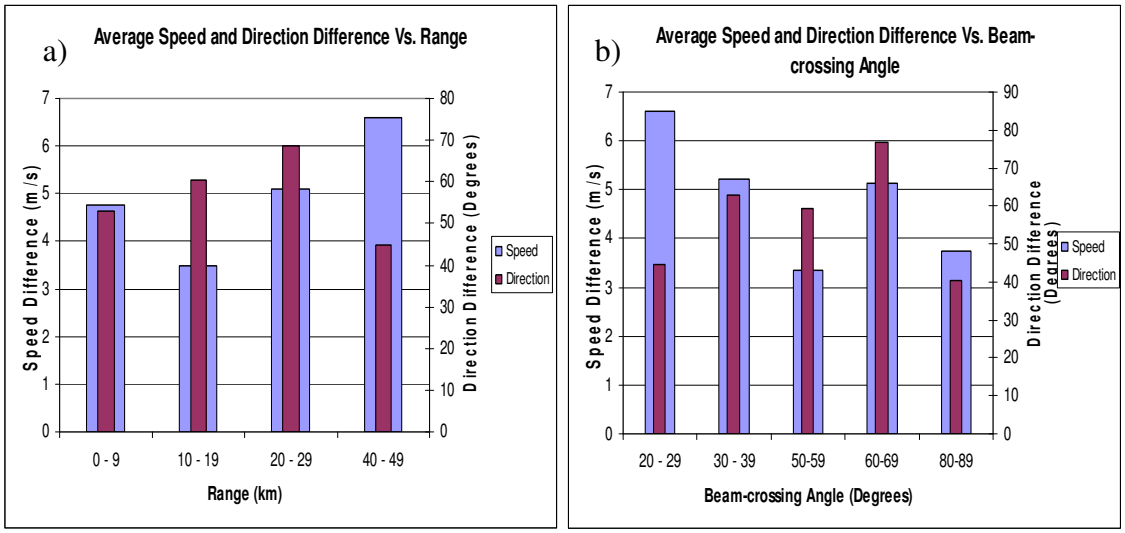

FIG. 4.5. Average speed and direction differences vs. range (a) and beam-crossing angle (b) for Houston.

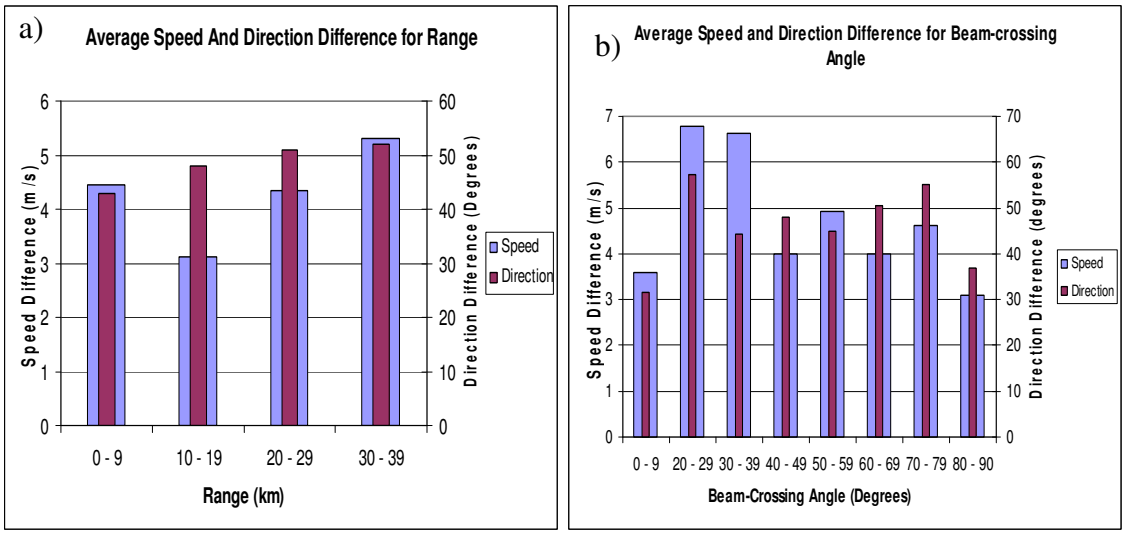

FIG. 4.6. Average speed and direction differences vs. range (a) and beam-crossing angle (b) for Dallas.

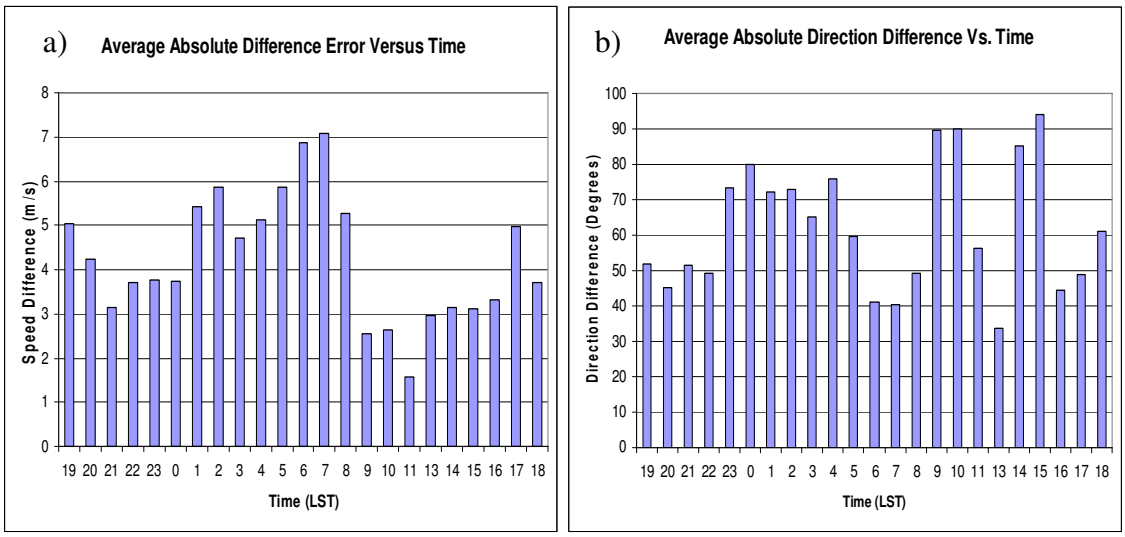

FIG. 4.7. Average absolute speed (a) and direction (b) differences versus time for Houston.

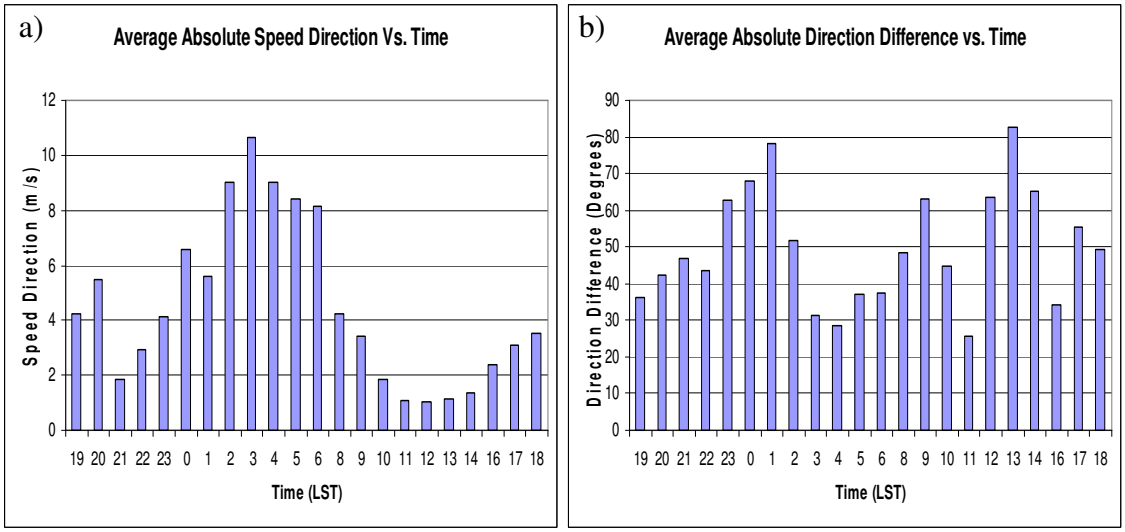

FIG. 4.8. Average absolute speed (a) and direction (b) differences versus time for Dallas.

4.1.2 *Surface-Station Discussion*

Large positive medians for speed differences were present for both Houston and Dallas (Table 4.1 and Figs. 4.1 and 4.2). A large speed bias was expected for the surface

stations because it is assumed that winds aloft are faster than winds at the surface due to friction at the surface. A positive bias in wind direction was also calculated for both Houston and Dallas (Table 3 and Figs. 4.1 and 4.2). This, too, is acceptable because of the expected difference in conditions aloft and the conditions at the surface. At the surface, winds are balanced between pressure gradient, coriolis, and a frictional force. Aloft, winds are not subject to a frictional force and are strictly subject to a balance between pressure gradient and coriolis, resulting in more westerly winds.

Large differences in the multiple regression r^2 values for beam-crossing angle and range for wind speed and direction errors were present between Houston and Dallas. Forty-four percent of the variability in speed difference can be explained by the range and beam-crossing angle for Houston, while only eleven percent of the speed difference variability can be explained by range and beam-crossing angle for Dallas. Wind direction difference presents the opposite situation, with 9 percent explainable by range and beam-crossing angle for Houston, and 29 percent explainable by range and beam-crossing angle for Dallas. The difference in correlations between cities most likely is a result from the different boundary layer characteristics. Houston is more likely than Dallas to have directional shear between the surface and the grid level due to the land-breeze and sea-breeze effect. Dallas can have either directional shear or speed shear, depending on the synoptic conditions occurring at the time.

The plot of wind speed and direction differences versus time (Fig. 4.7 and 4.8) shows that the largest difference in speeds occurred during the early morning hours, from 2 to 5 LST for Dallas, and 2 to 7 LST for Houston. Both recorded lower differences over the

late morning and early afternoon hours, about 9 to 16 LST for both. Higher differences for direction were calculated during the overnight hours and early morning hours, from about 21 to 2 LST for Dallas and 21 to 4 LST for Houston. During the overnight hours, a turbulent, residual layer is present over a stable, nocturnal boundary layer (Stull 1988). The differences in the wind characteristics between the two layers can explain the high differences in direction and speed during the overnight hours. Both preformed well over the early evening hours, from 19 to 23 LST. Houston had two spikes of high difference at 9 and 10 LST and again at 14 and 15 LST. Dallas also had relatively high differences at these times, though not as pronounced. During the summer months over Houston, before the onset of a sea-breeze, stagnant flow is frequently observed (Banta et al. 2005). During this time, winds at the surface are light and variable, which can cause large difference in the dual-Doppler synthesis of wind direction. Fourteen and 15 LST correspond with a typical time for the progression of the sea-breeze. At this time, the difference between winds at the surface and winds aloft may be large. The timing of the sea-breeze does vary greatly, however, from late morning to early evening. It is possible that any of the large directional differences over Houston could be caused by sea-breeze progression.

4.1.3 *Upper-Air and Dual-Doppler Wind Analysis*

Dual-Doppler wind vectors were calculated at 400 meters and 600 meters above the surface for Houston and Dallas, respectively. Upper-air observations were used for

comparison to more closely match the height level at which dual-Doppler wind calculations were made and avoid the problems discussed above. Figure 4.9 and Figure 4.10 are histograms of wind speed (a) and direction (b) differences from the La Porte wind profiler in Houston and the rawinsonde in Dallas, respectively. Statistics produced for each location are presented in Table 4.2. The Student's t-tests done on the differences from the wind profiler comparison show that there is enough evidence to reject the hypothesis that the differences in the means are equal to zero for both speed and direction at the 5% significance level. The student's t-tests done on the differences from the rawinsonde comparison show that there is enough evidence to reject the hypothesis that the differences in the means are equal to zero for both speed and direction at the 5% significance level. However, there is not significant evidence to reject the hypothesis at the 1% significance level for either speed or direction.

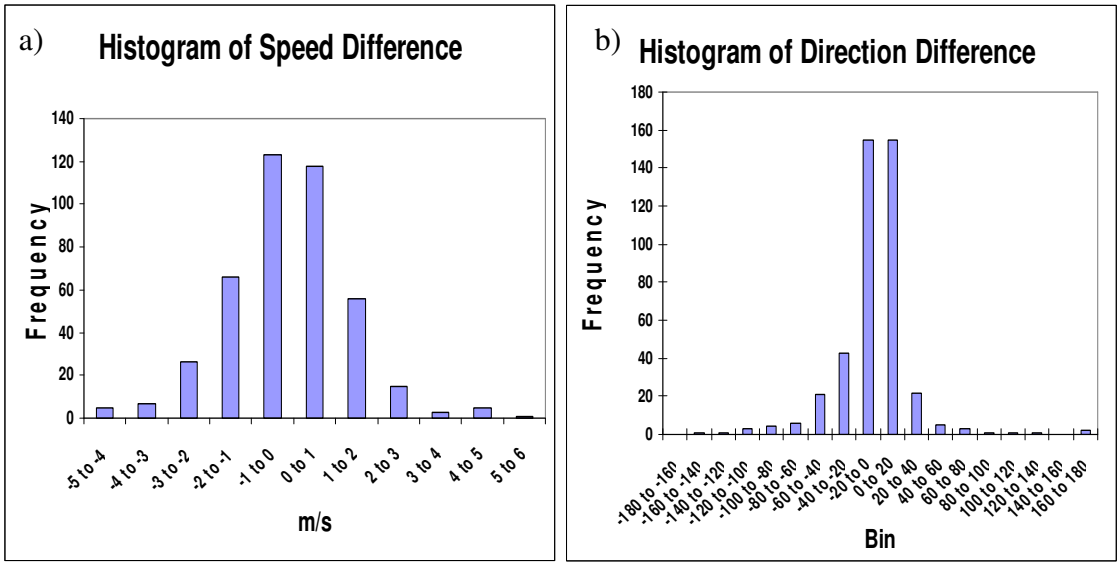

FIG. 4.9. Histograms of speed (a) and direction (b) differences for the Laporte wind profiler.

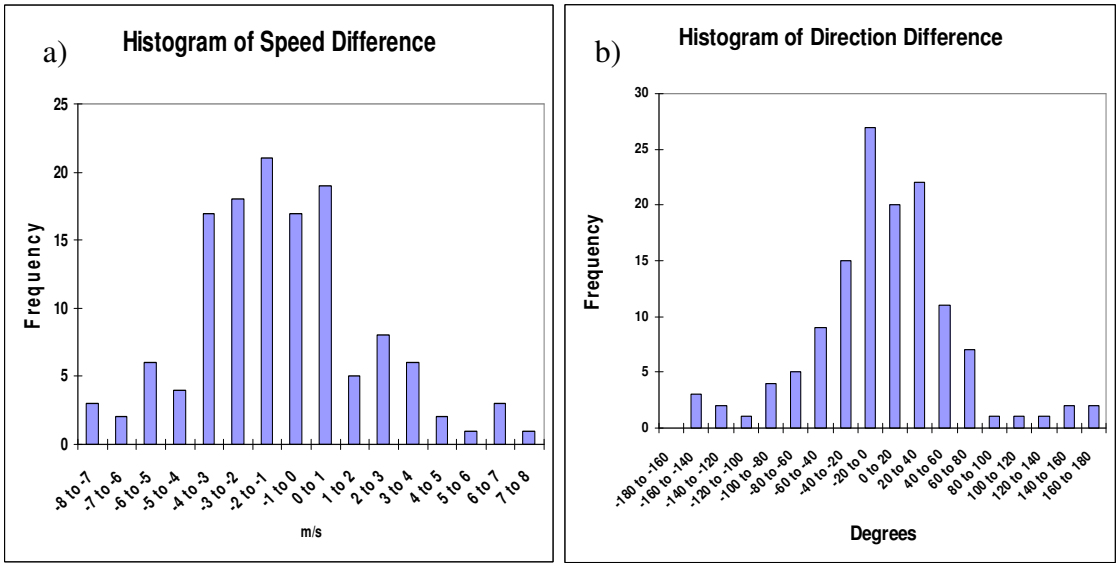

FIG. 4.10. Histograms of speed (a) and direction (b) differences for the Dallas rawinsonde.

Table 4.2. Descriptive statistics for the speed and direction differences for the wind profiler and the sounding

Instrument	Median	Mean	St. Dev.	Relative Error Median	Relative Error Mean	Relative St. Dev.
Speed Profiler (ms^{-1})	-0.12	-0.15	1.46	-0.032	0.018	0.37
Direction Profiler (degrees)	-1.86	-4.77	29.64	X	X	X
Speed Sounding (ms^{-1})	-1.10	-1	2.94	-0.23	-0.18	0.60
Direction Sounding (degrees)	0.17	0.94	57.32	X	X	X

Absolute speed (a) and direction (b) differences versus time were plotted for both Houston (Figure 4.11) and Dallas (Figure 4.12). Data were averaged over the course of every day that data was compared. For example, the data in the 18Z column contain any data from 1800Z to 1859Z. Direction difference vs. profiler (rawinsonde) recorded wind speed (a) and wind speed difference vs. profiler (rawinsonde) recorded wind speed (b) are presented in Figure 4.13 (Figure 4.14) for Houston (Dallas). The r^2 for the profiler (sounding) is 0.3223 (0.3416) for speed difference versus wind speed. It was not appropriate to compute a linear r^2 value for direction difference versus wind speed.

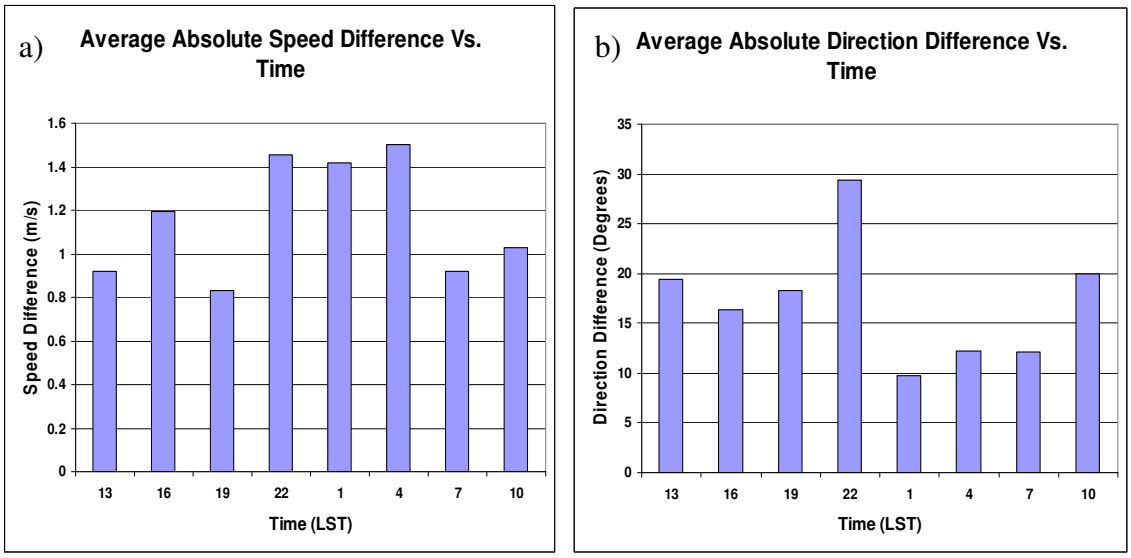

FIG 4.11. Average absolute speed (a) and direction (b) differences versus time for the La Porte profiler.

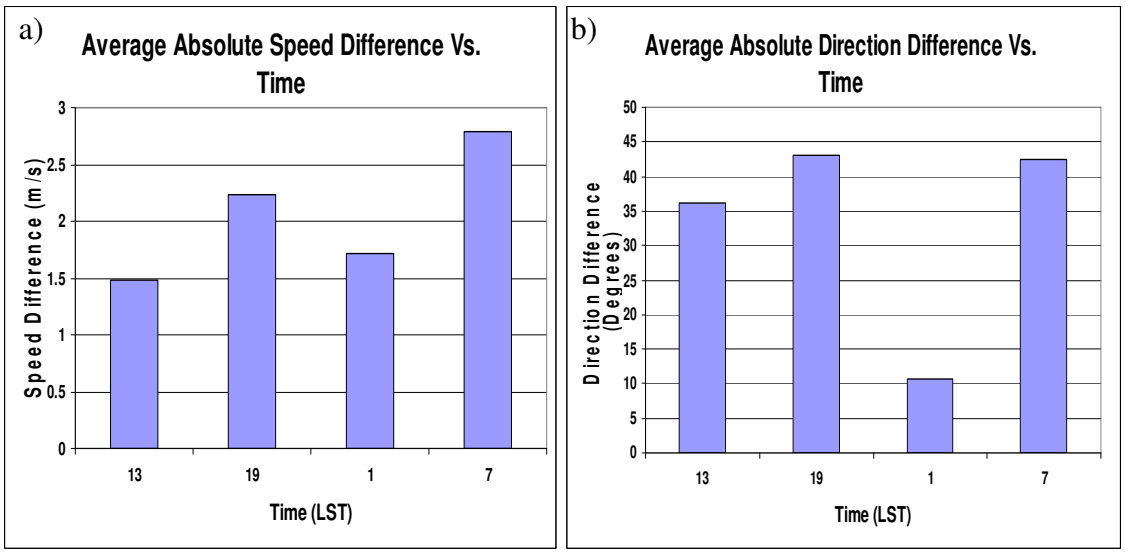

FIG 4.12. Average absolute speed (a) and direction (b) differences versus time for the Dallas rawinsonde.

b)

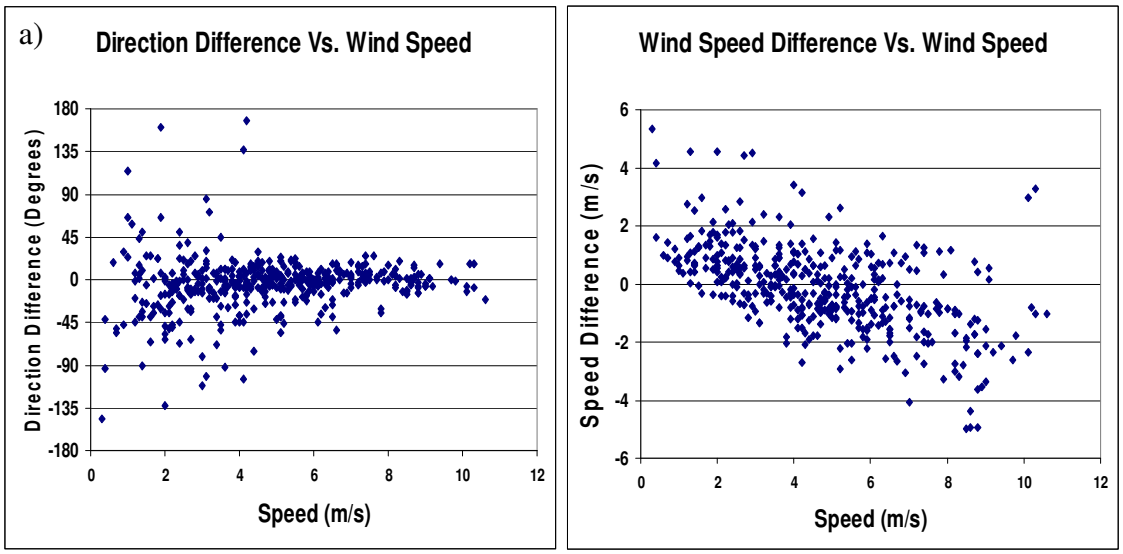

FIG. 4.13. Direction (a) and speed (b) differences versus profiler measured speed.

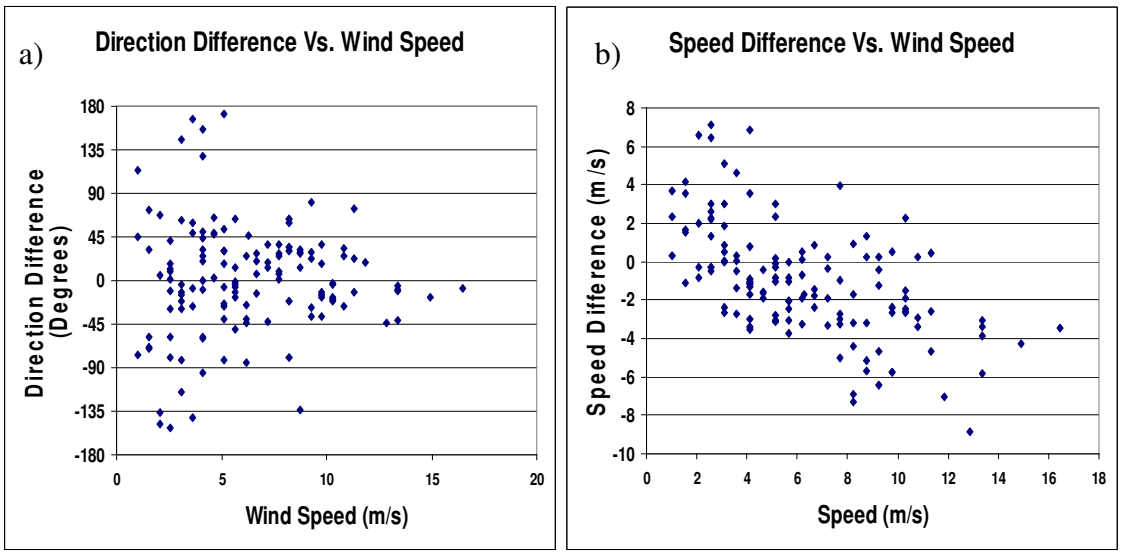

FIG. 4.14. Direction (a) and speed (b) differences versus rawinsonde measured wind speed.

4.1.4 *Upper-Air Discussion*

Comparisons to both the rawinsonde and the profiler yielded much smaller differences than the comparisons to surface stations. This was anticipated based on the assumption that much of the difference calculated in the surface station comparison was due to the difference in height between the calculated dual-Doppler winds and the surface. The profiler results were in better agreement than the rawinsonde comparison. It is possible that due to the averaging done for both the profiler and the dual-Doppler data, any small temporal or spatial variations in wind speed and direction were averaged out, producing results that were in better agreement than measurements that were compared at point times and locations. Statistical results also show the validity of the dual-Doppler data. We are able to conclude that the difference between the means of both speed and direction at the 5% significance level is not significantly different from zero for the profiler. We are able to conclude the same for the rawinsonde at the 1% significance level. However, the profiler and the rawinsonde may have errors associated with them, and therefore, this test is evidence enough of the validiaty of the dual-Doppler data.

By assuming that the data is normally distributed based on the histogram results; it is possible to make a statement on the possibility of any biases in the data. For normally distributed data, the mean of the data is roughly equal to the median. From Table 4.2, it appears as though this is the case with both speed and direction for the profiler and rawinsonde. Because of this, if the mean was not computed to be significantly different

from zero, than the median can be assumed to also not be significantly different from zero, and no significant biases exist.

Diurnal analysis of upper-air comparisons resulted in slightly different patterns than the surface station analysis. Profiler comparisons show that the majority of wind speed difference occurred late evening into overnight, while the largest differences for wind direction occurred in the late morning into the afternoon. Though plotted, the times of 1 and 13 LST recorded much less data by the rawinsondes than the times of 7 and 19 LST. The largest differences for wind speed for the sounding data occurred during mid-morning. The differences for direction were fairly constant. The lack of temporal data for the Dallas rawinsonde creates difficulty in coming to a conclusion on diurnal patterns and if there is any difference from the surface stations. The difference between the profiler comparison and the Houston surface station comparisons is most likely due to the more complicated diurnal boundary layer conditions in the form of land, bay, and sea-breezes, present in Houston. The various breezes are limited in vertical structure. This creates wind patterns near the surface which are different than the winds above the breezes, which are normally limited to the lowest first kilometer.

Almost all direction difference for both the profiler and the rawinsonde occurred when winds were less than 5 ms^{-1}. This is expected due to errors in radar wind measurements at low speeds. Wind direction tends to be variable when wind speed is low. However, the data could be biased due to the lower amount of data collected for higher wind speeds. There is more scatter present with the Dallas data, but this is most likely a result of the averaging done with the profiler. The plots and correlation

coefficients of wind speed difference versus wind speed were very similar between the profiler and the rawinsonde. The r^2 value for both expresses that about 1/3 of the variability in wind speed difference can be explained by wind speed. The plots show that for lower wind speeds, the dual-Doppler analysis overestimates wind speeds while for higher wind speeds the dual-Doppler analysis underestimates wind speeds. Dual-Doppler comparison to sounding data by Wilson et al. (1994) yielded similar results.

In conclusion, based on the above analysis, the dual-Doppler winds appear favorable for further scientific use. At the specific locations tested (Figures 4.3 and 4.4), most differences are either random or can be explained by radar techniques or differences in height levels between measurements. There does not appear to be any significant biases with the wind data that would make the data unsuitable for use. However, there appears to be some issues involving artifacts and contamination by birds, which will be discussed in some more detail in the following sections.

4.2 *Averaged Results*

The following sections will present the results from the averaged data analyses. Diurnal images of convergence, 2 km reflectivity, 2 km frequency, 7 km reflectivity, count of greater than 30 dBZ reflectivity at 7 km, average cumulative rain, and a plot of wind vectors will be presented along with time-series plots for all of the above. Total averages will also be presented.

4.2.1 *Average Horizontal Winds in the Boundary Layer*

Figure 4.15 presents horizontal wind vectors plotted every 1 km at 0.4 km above ground level (AGL). Wind vectors are scaled to the largest vector, which is indicated in meters per second at the bottom right corner of each plot. At midnight (a) winds were generally from the east. Winds were slightly more south-easterly south of Houston, and winds were more north easterly over and east of Galveston Bay. This pattern was the same at 1 LST (b). A similar pattern was present during the next three hours (c-e), but the southerly flow over Houston and the northerly flow over Galveston Bay increased in strength. Also during these hours, a small area of anti-cyclonic flow was present over the northwest coast of Galveston Bay. At 5 LST (f) the flow over the left dual-Doppler lobe was almost entirely southerly, while the flow over the north Galveston Bay was almost entirely northerly. The flow over the south Galveston Bay remained from the northeast. At 6 LST (g) the general flow was the same. However, the presence of birds can be identified by the divergent wind vectors located west of downtown Houston. At 7 LST (h) the northerly/southerly pattern was still present, but wind was slightly more random. At 8 LST (i), winds to the north east of Houston are from the north east while winds south of Houston were generally from the southeast. The convergence area was co-located with an area of erroneous winds also identified in the convergence plots. Winds between 9 and 12 LST (j-m) remain the same until 13 LST (n) at which time winds to the north east of Houston and to the west of the Galveston Bay coast become easterly. At 14 LST (o) winds in the left dual-Doppler lobe were from the southeast. Winds in the bottom right corner of the left dual-Doppler lobe are known to be in error.

This area was also identified in the convergence plots. Also, winds over the right dual-Doppler lobe were almost entirely easterly. Winds to the east of Galveston Bay were still slightly north easterly. Wind patterns remain similar over 15 and 16 LST (p and q). At 17 LST (r) winds north of Galveston Bay became southeasterly. At 18 LST (s) winds to the west of Houston became slightly more southerly. By 19 LST (t) winds to the east and northern portion of Galveston Bay were from the southeast. At 20 LST (u) the winds east Galveston Bay changed to northeasterly, with the whole domain showing a more easterly pattern. During the next two hours (v and w) winds were mainly from the east over the Galveston Bay and southeasterly over and near Houston. At 23 LST (x) winds were almost entirely easterly over the whole domain.

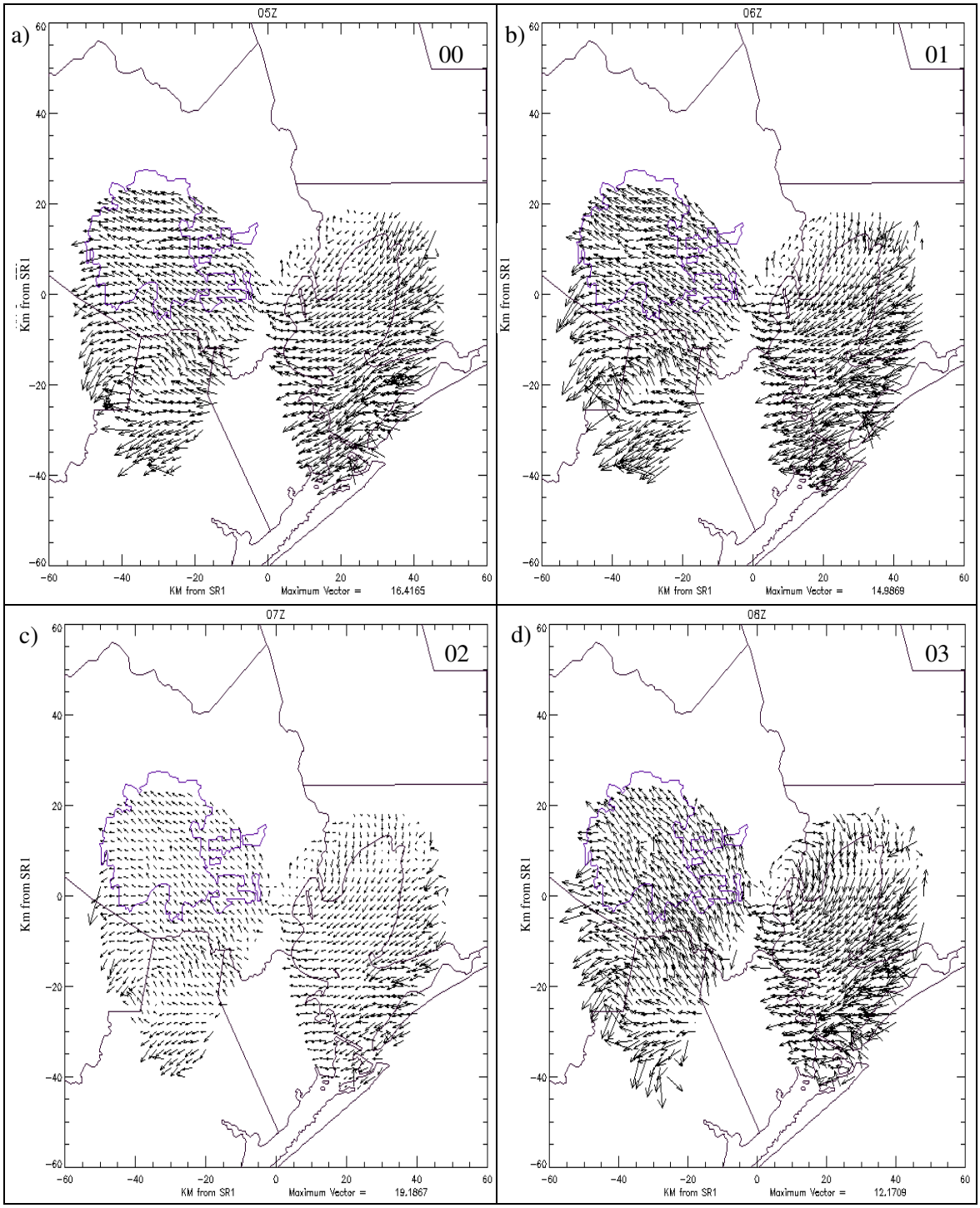

Figure 4.15. Average horizontal boundary layer wind vectors. (a-d) 00 to 03 LST at 0.4 km AGL. Largest wind vector in meters per second. Times in upper right corners are local.

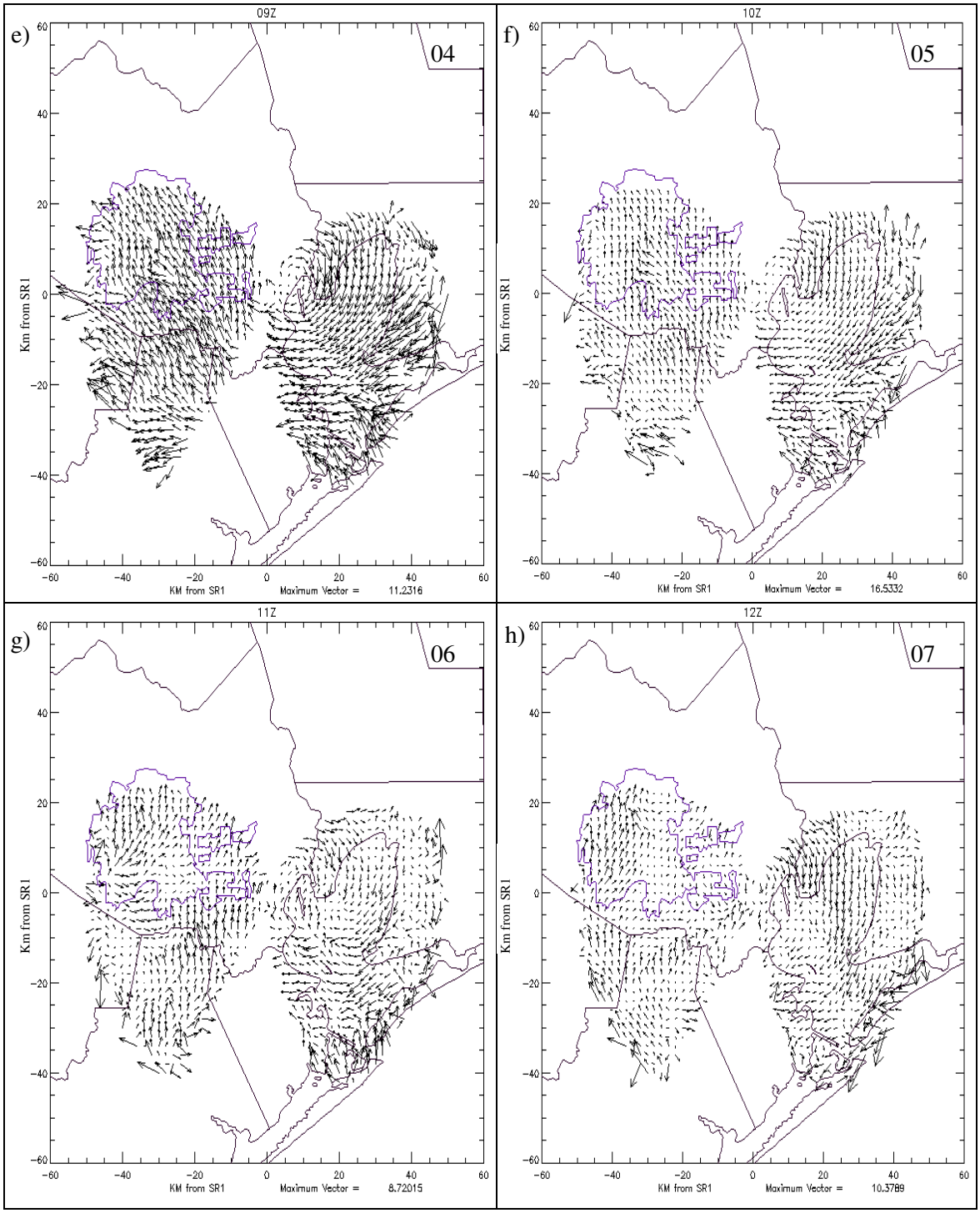

Figure 4.15 cont. (e-h) 04 to 07 LST.

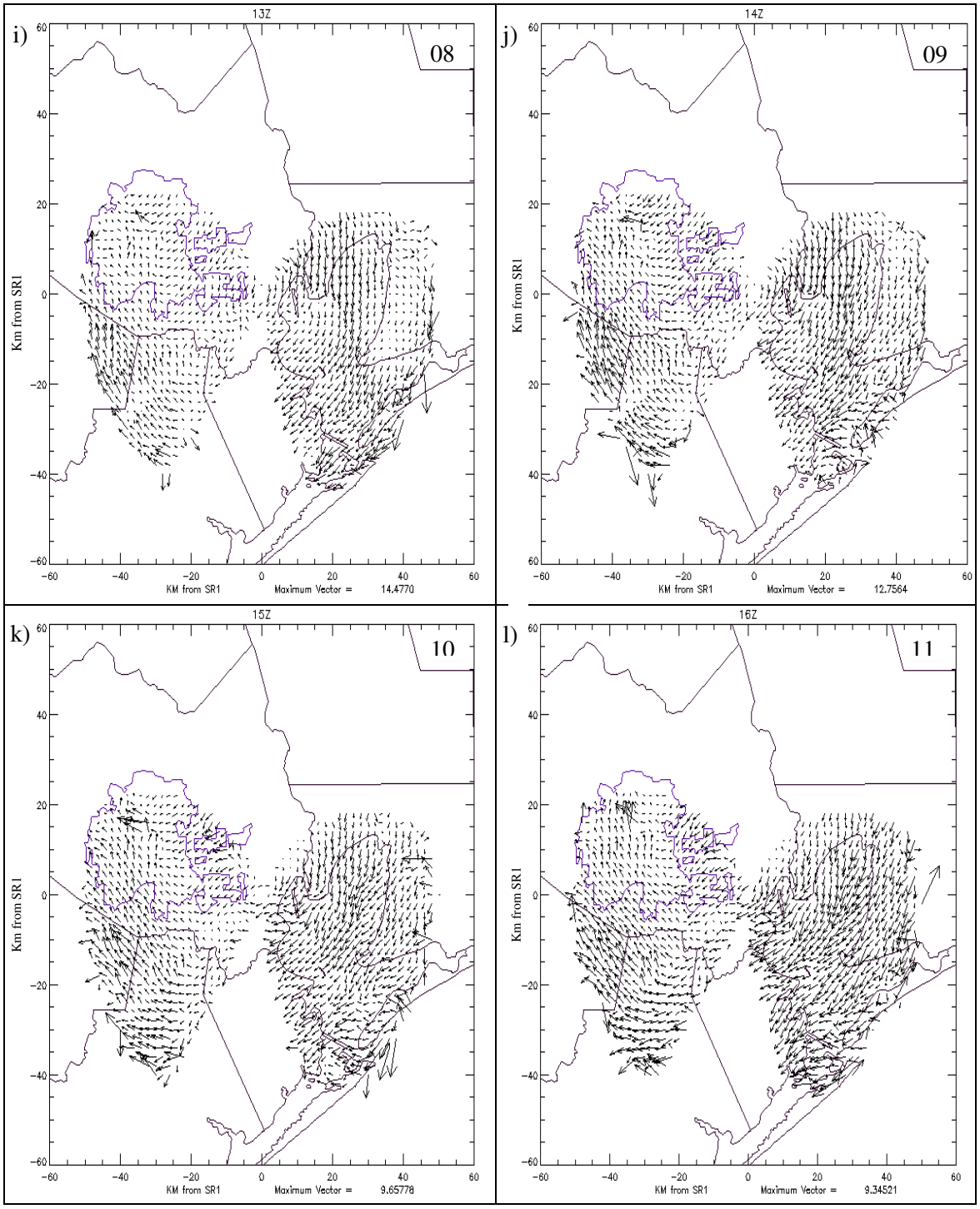

Figure 4.15 cont. (i-l) 08 to 11 LST.

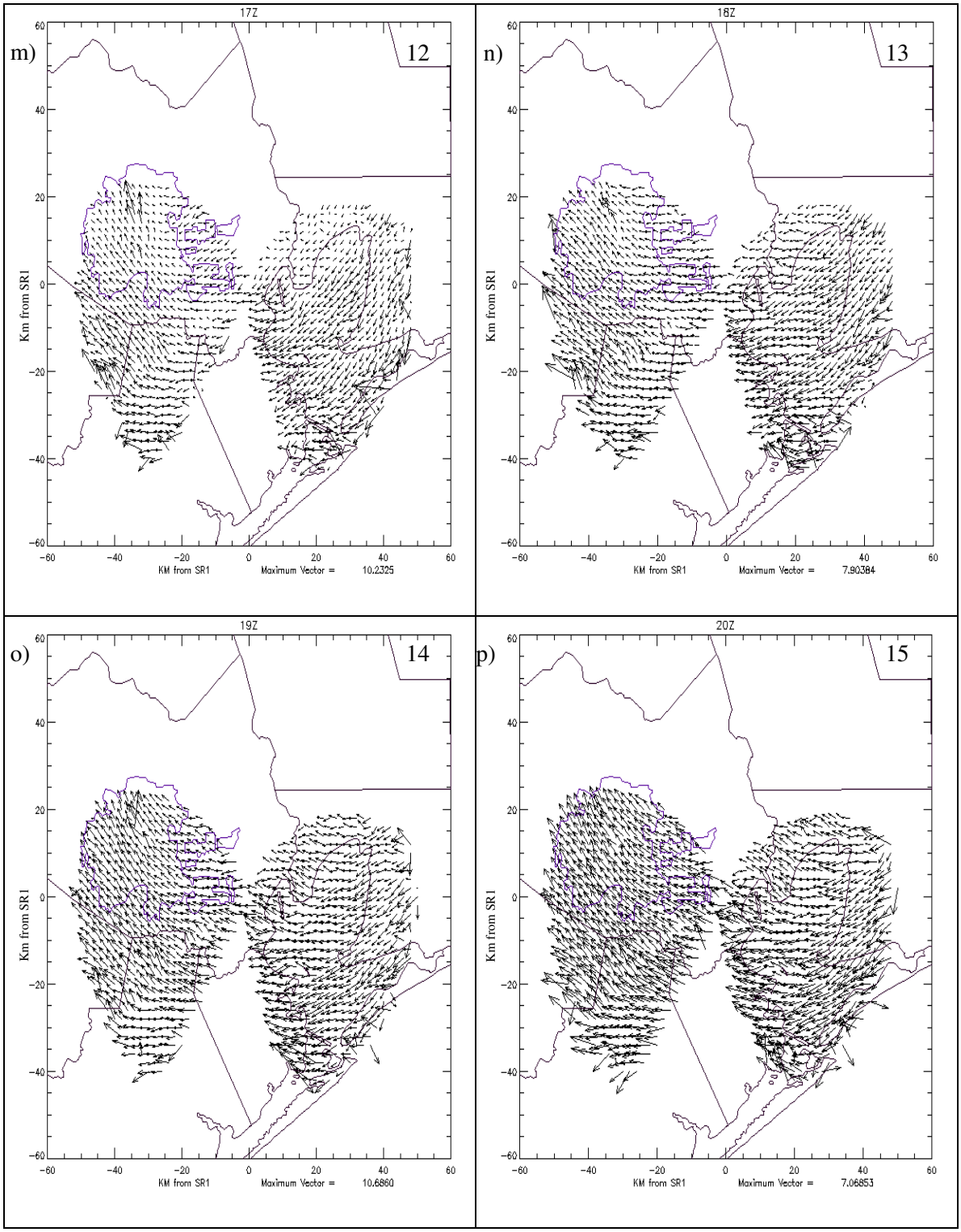

Figure 4.15 cont. (m-p) 12 to 15 LST.

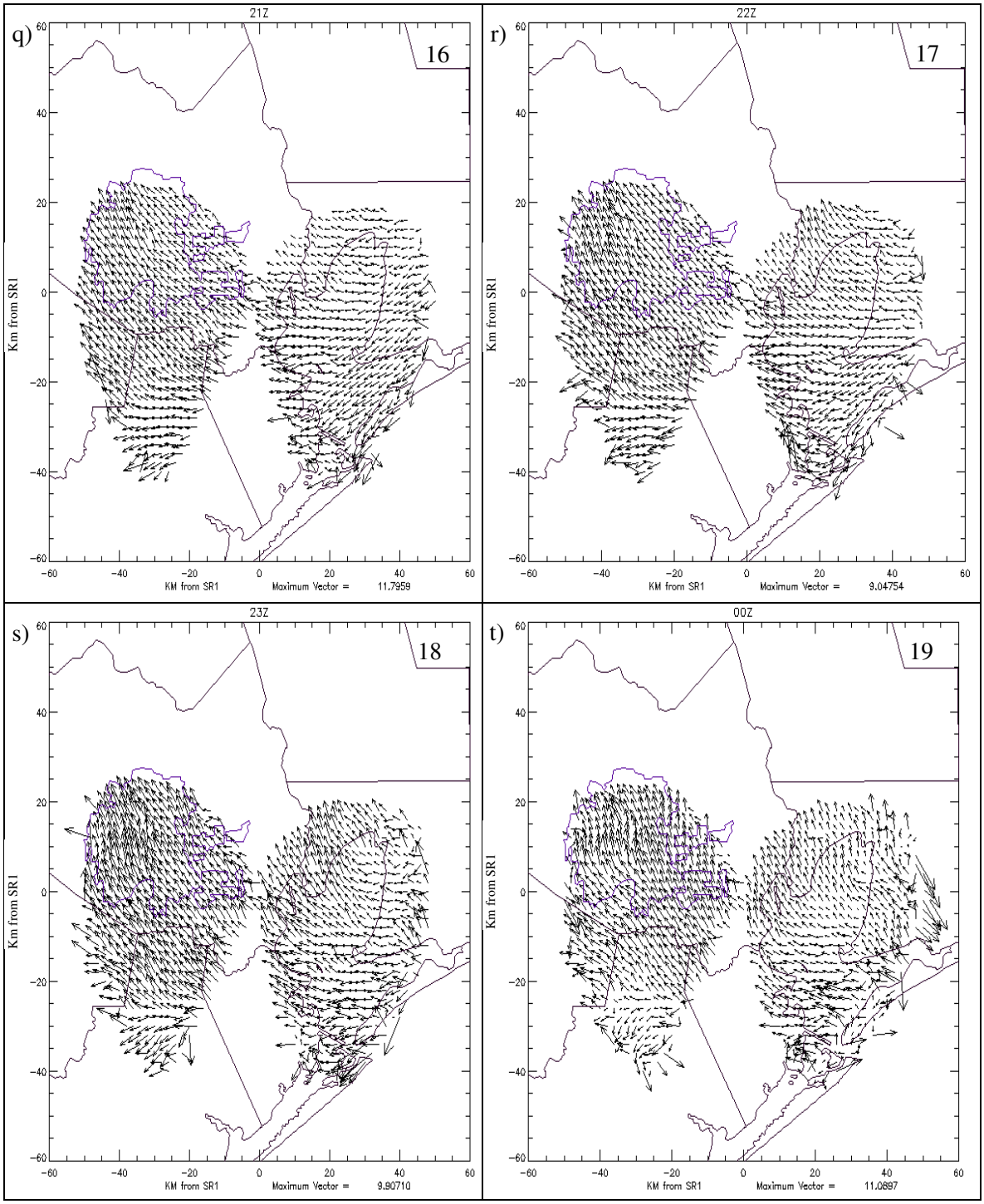

Figure 4.15 cont. (q-t) 16 to 19 LST.

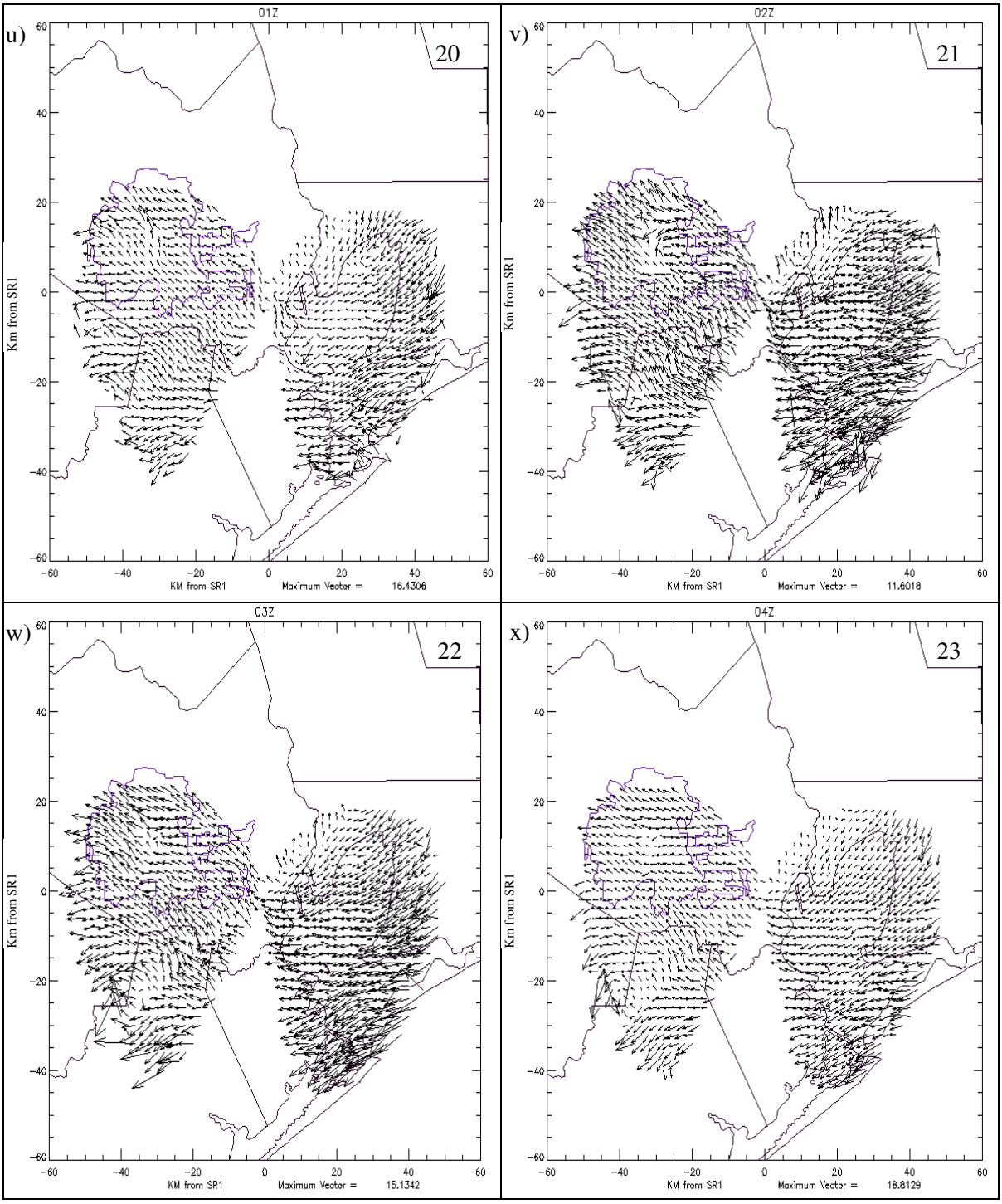

Figure 4.15 cont. (u-x) 20 to 23 LST.

Figure 4.16 presents a time series of average boundary layer wind vectors at 400 m AGL for box 1, box 4, and the domain. Values below each time series is the maximum vector for that time series in meters per second. Each time series is scaled to its maximum vector. The box 1 time series shows that winds average out of the south for each hour. Winds averaged southeast between midnight and 5 LST. At 6 and 7 LST winds were weakly southwest. Winds were then weakly southeast for the rest of the time series. The winds were the strongest from the southeast at 19 LST. Box 4 was almost entirely northeast. Winds averaged from the southeast only between 17 and 19 LST. There appears to be no strong peak in northeast wind speeds, but winds were generally strongly from the northeast between 20 and 5 LST. The domain average was easterly between midnight and 3 LST. Winds became southerly by 6 LST. Winds were from the northeast between 8 and 11 LST. Winds became southeasterly at 14 LST, and reached a peak in strength at 19 LST. The domain averaged winds then returned to easterly at 20 LST.

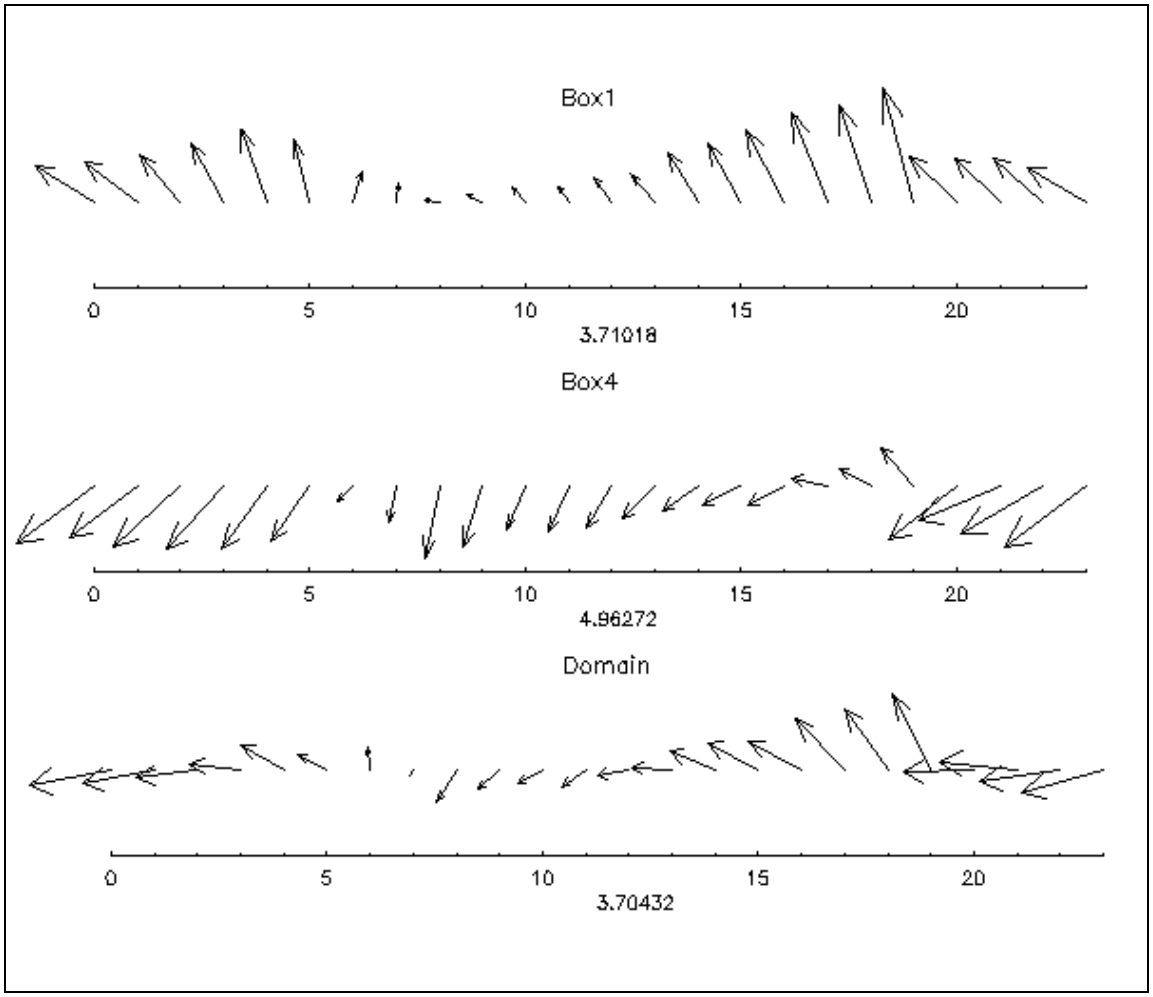

Figure 4.16. Time series of average boundary layer wind vectors at 0.4 km AGL altitude for box 1, box 4, and the domain. Values under each time series is the maximum average vector for the time series in meters per second. Time on the x-axis is local.

4.2.2 *Average Convergence*

Diurnal convergence images are presented in Figure 4.17. Despite the filtering done on the convergence images, some artifacts persist. A convergence/divergence couplet was consistently present over northwest Houston, and only present on the WSR-88D raw data. It is highly unlikely that this feature is real due to its consistency and is most likely

an error in the WSR-88D, possibly due to the multiple PRFs or the clutter mitigation scheme used. There also exists an area of bad data that is radial to SR1, located at the southwest portion of the left dual-Doppler lobe. The radial artifact is non-physical in shape and is suspected to be a propagation error due to a tower closely located to SR-1. At midnight (a), there was convergence over both the bay and downtown Houston. The northwest shoreline of Galveston Bay showed the greatest amount of convergence during this time. This pattern continued until dawn (b-f) at which time convergence increased greatly south of Houston, west of Galveston Bay. A large area of divergence over southwest Houston also appeared at this time, 6 LST (g), which is known to be an area that birds leave roost at dawn. A line of convergence formed nearly perpendicular to the northern Galveston Bay shore line at 7 LST (h). This line became more defined during the next hour (i), but weakened (j) and disappeared by 10 LST (k). During this time, convergence was spatially large over and to the south of the Houston area, with the greatest coverage area of convergence occurred at 9 LST (j).

Also, at 10 LST (k), the majority of Galveston Bay was characterized by divergence, while downtown and downwind of Houston was associated with convergence. At this time, there existed an area of divergence located over west Houston. Divergence over the bay increased during the next several hours from late morning to mid-afternoon (k-p), reaching a peak in strength at 16 LST (q). There still existed areas of convergence near the shoreline during this period of divergence, however. Convergence over and near the Houston area also decreased during this time period, but to a much lesser extent. At 17 and 18 LST (r and s) local time, there was a large area of convergence just west of downtown Houston. This area was replaced by a large area of divergence at 20 LST (u). At 21 (t) LST, convergence began to increase over the Bay and downtown Houston. Convergence over the Bay increased during the overnight hours (v-x) while the convergence over the downtown Houston area remained fairly steady.

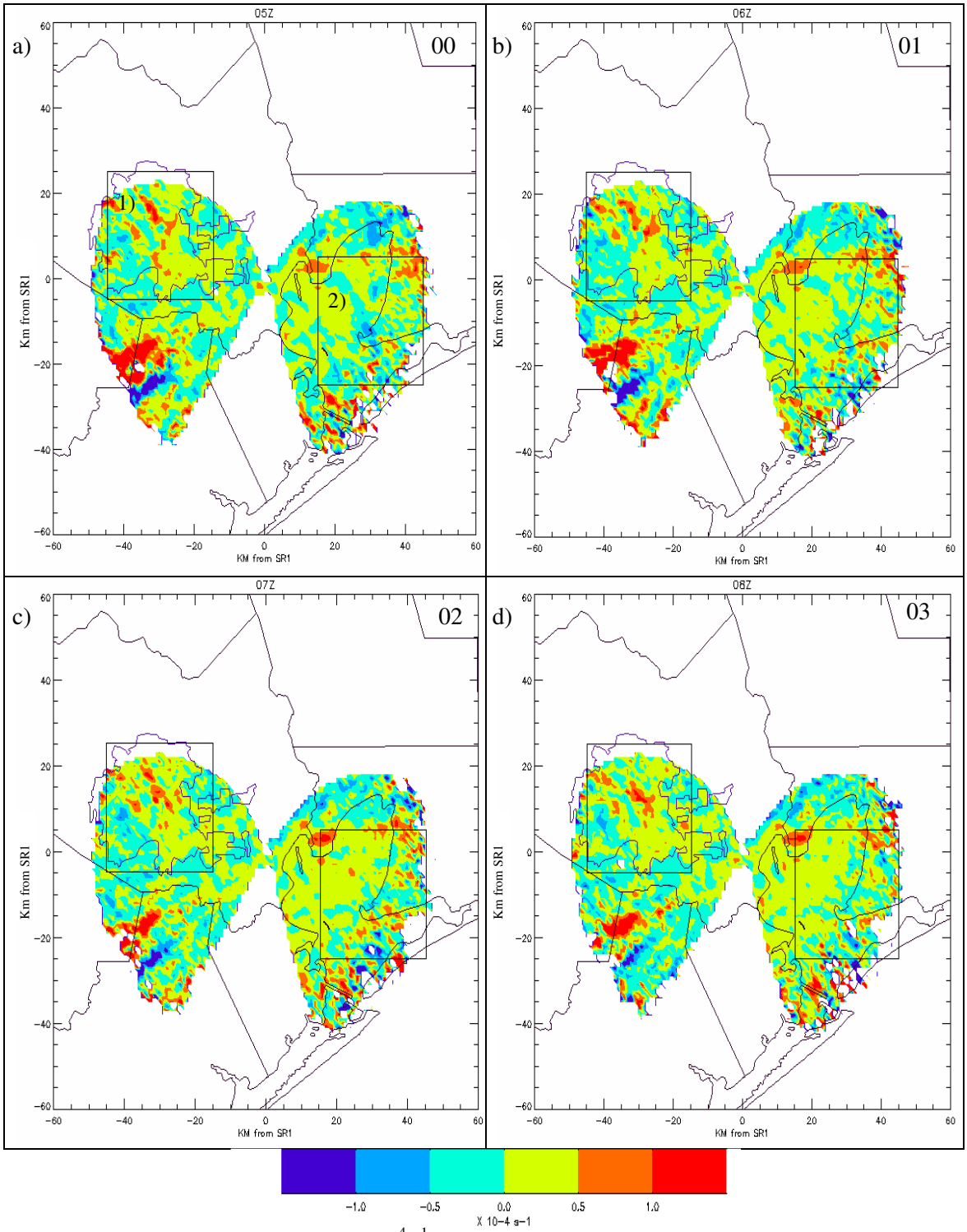

Figure 4.17. Average convergence ($10^{-4}s^{-1}$). (a-d) 00 to 03 LST. Convergence (divergence) is indicated by warm (cool) colors. Boxes are labeled in a. Boxes 2 and 3 are not present in the convergence averages due to lack of coverage. Times in the upper right corners are local.

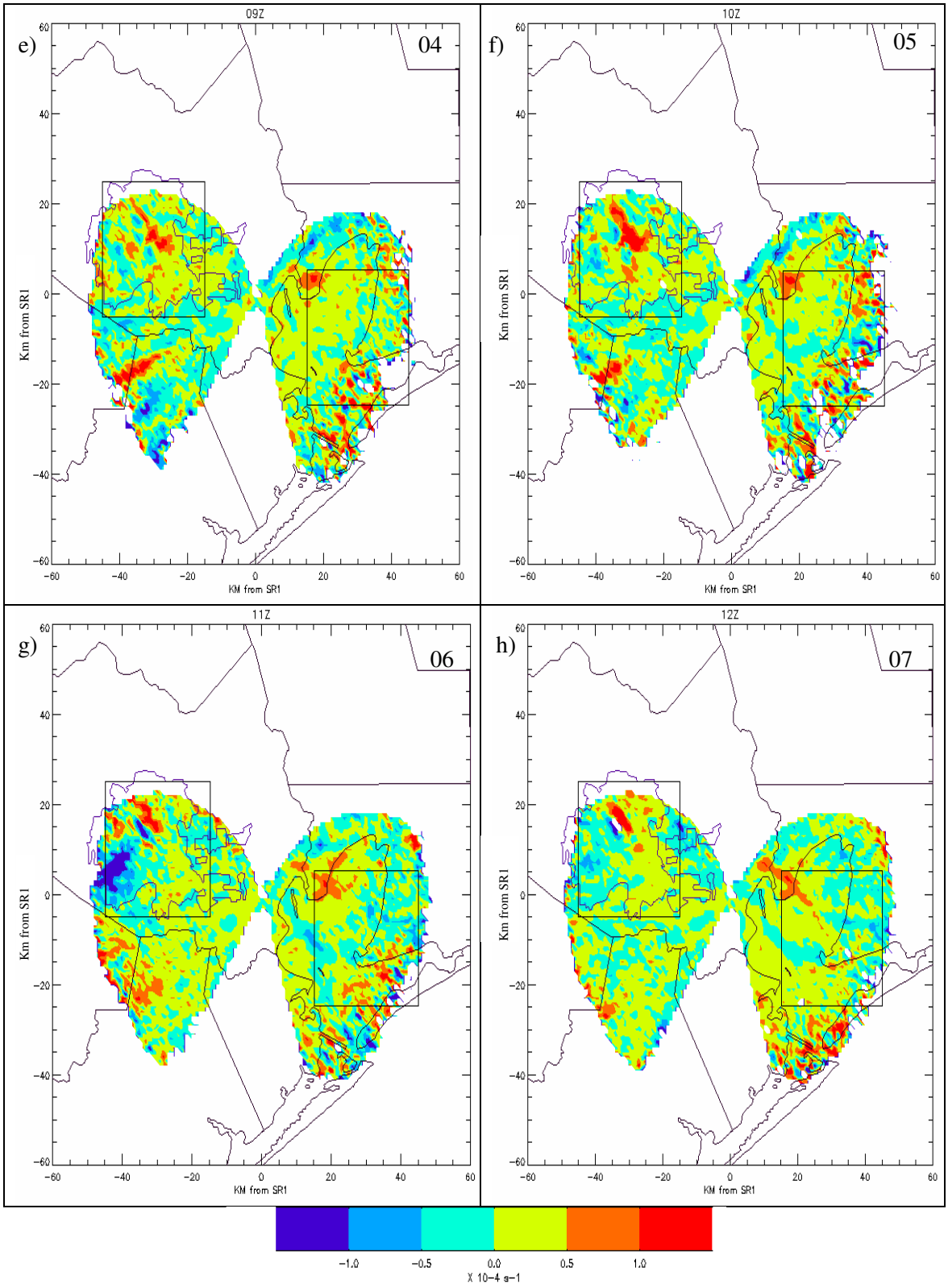

Figure 4.17 cont. (e-h) 04 to 07 LST.

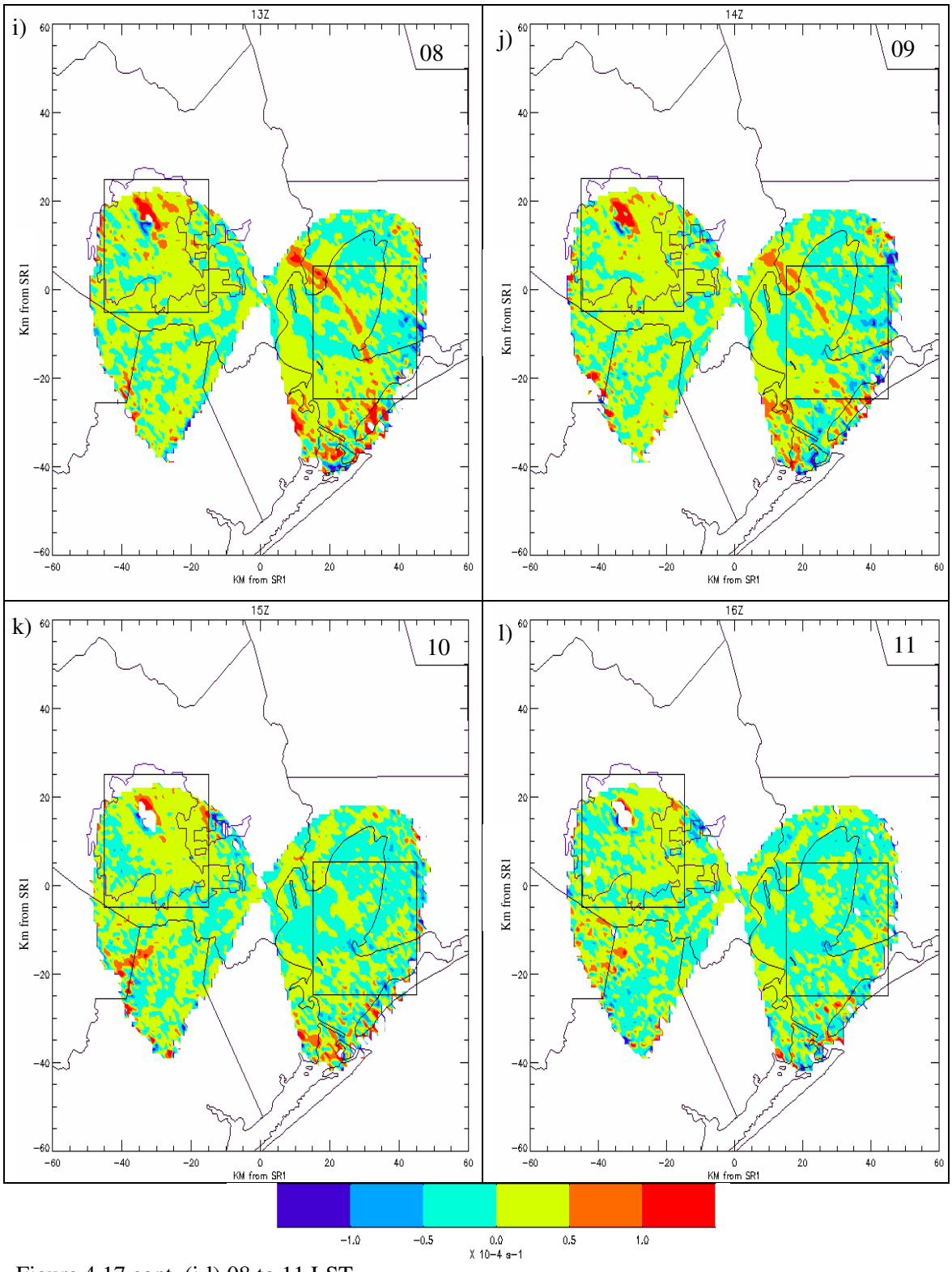

Figure 4.17 cont. (i-l) 08 to 11 LST.

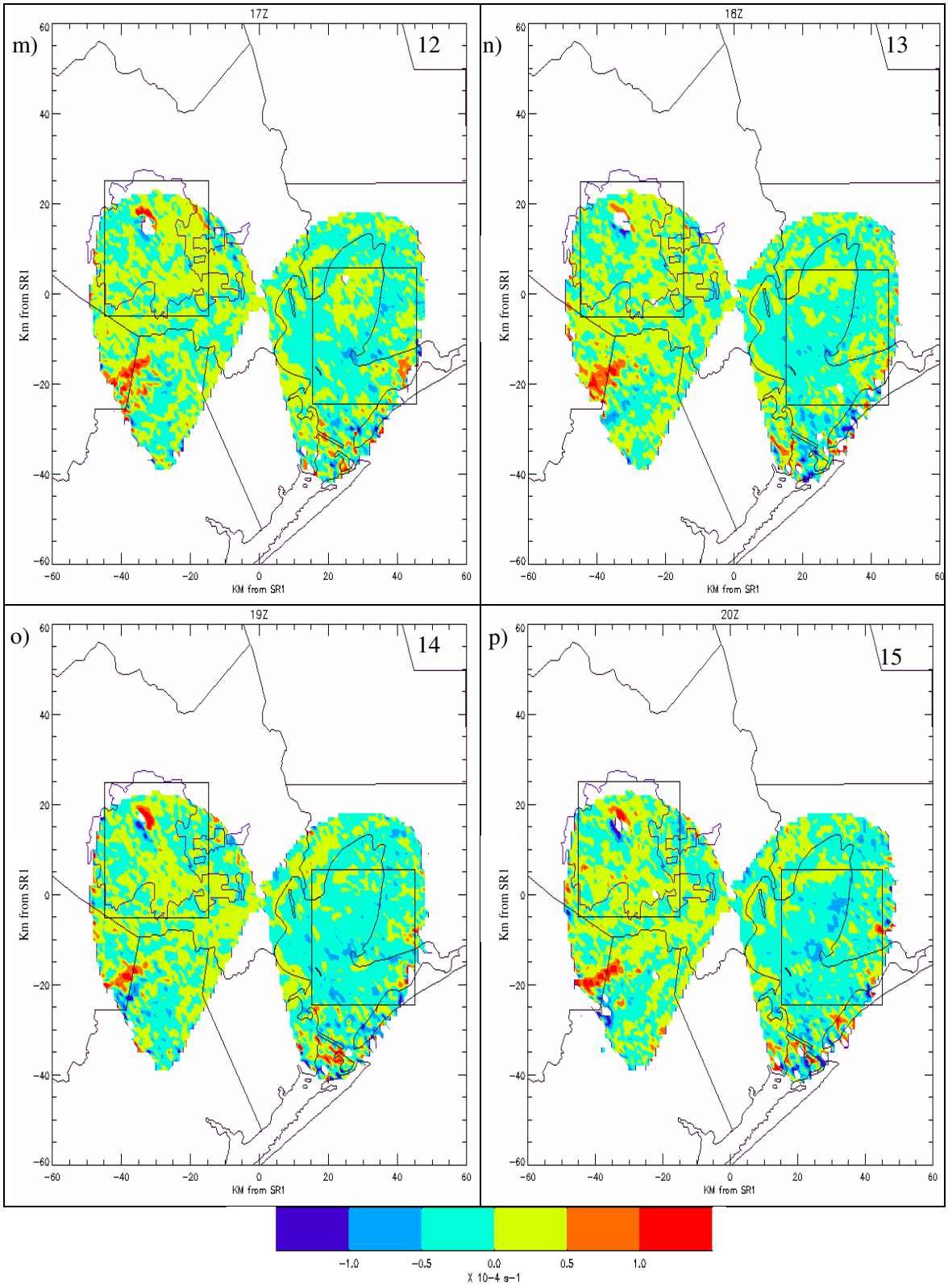

Figure 4.17 cont. (m-p) 12 to 15 LST.

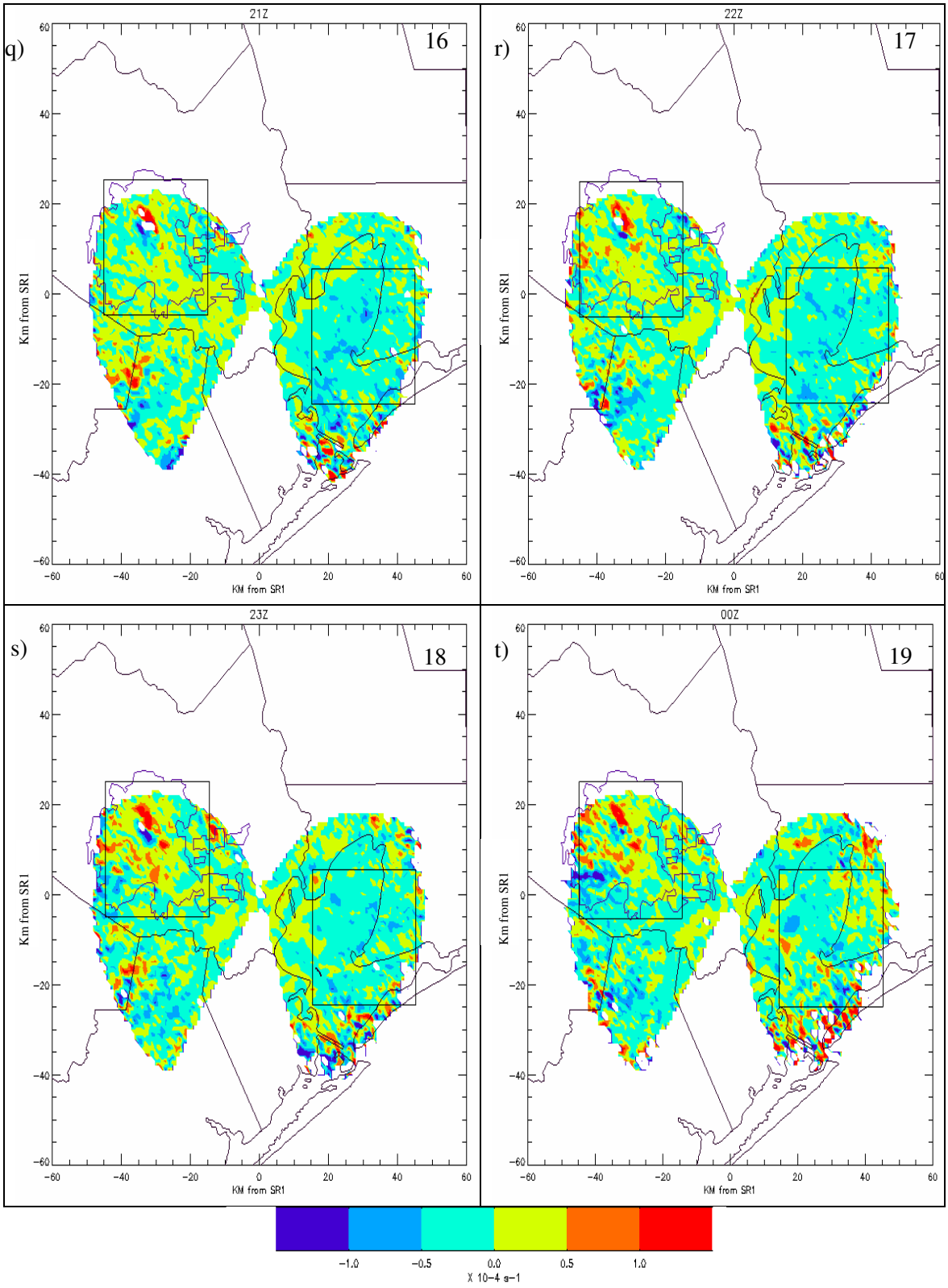

Figure 4.17 cont. (q-t) 16 to 19 LST.

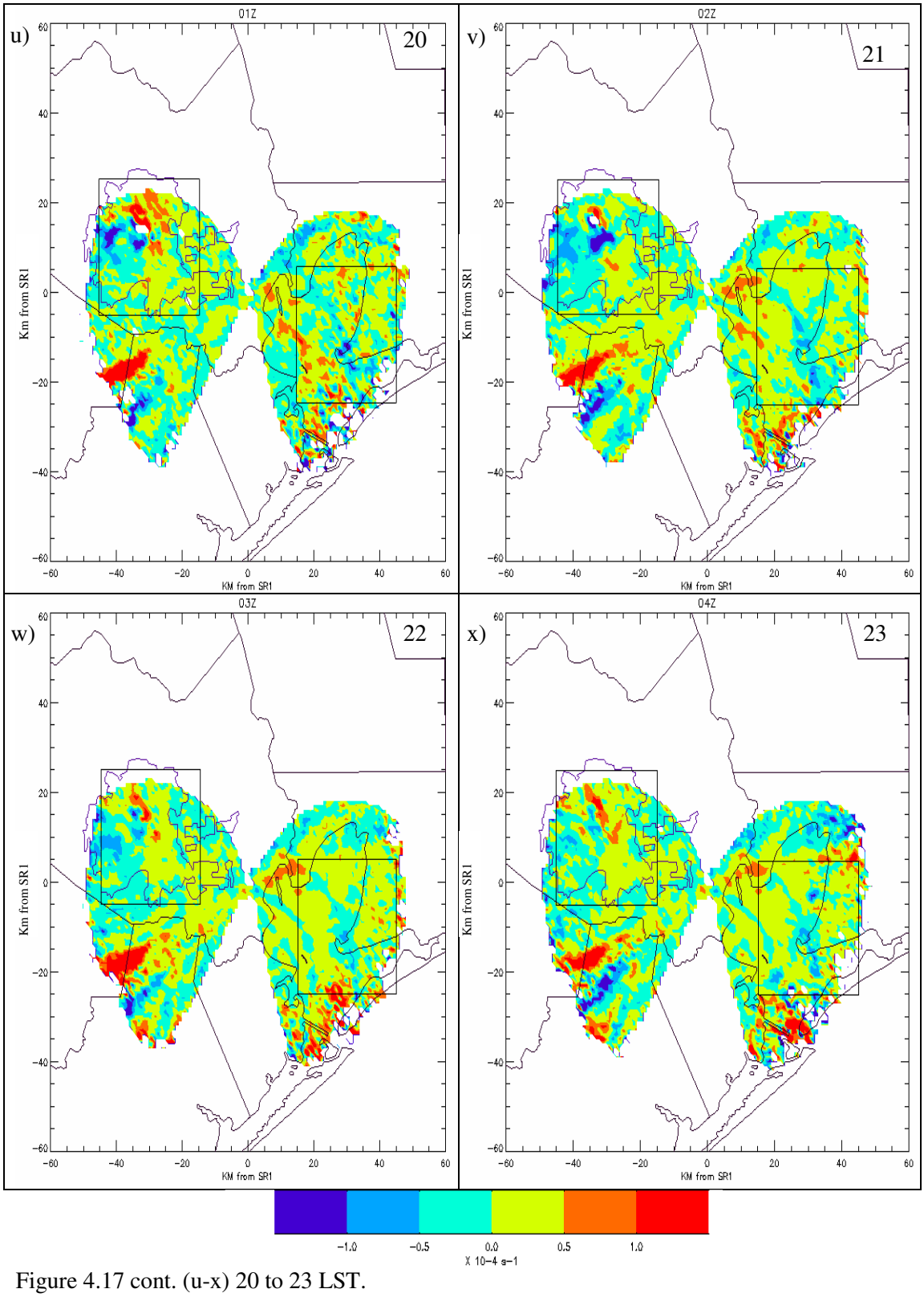

Figure 4.17 cont. (u-x) 20 to 23 LST.

Figure 4.18 presents a time series plot for each box and the domain. Both the domain and box 1 are presented with and without the filter for birds. The overall domain pattern was convergence from 20 LST overnight to 11 LST, followed by divergence. Box 1 shows continual convergence at all hours, except at times when birds are known to exist, 6 and 21 LST. Box 1, with the bird signal removed, greatly decreases the divergence associated with the bird signal, though it does not remove it completely. The convergence rose from midnight and peaked at 9 LST at 0.25 X $10^{-4}s^{-1}$. Convergence then fell and stayed steady until 17 LST, at which point convergence slowly began to increase. Box 1 convergence was greater than the domain average at all times, with the greatest difference occurring at 8 and 9 LST. The average for Box 4 was convergent from 20 LST through the overnight hours until approximately 9 LST, at which time divergence began. The convergence that occurred during the overnight hours was approximately of the same order of magnitude as the convergence in box 1 until dawn, at which time, the convergence in box 1 continued to decrease while the convergence in box 4 decreased.

Table 4.3 presents the Wilcoxon Rank-Sum test between each box and the domain. Average convergence over box 1 (Houston) shows the trend of being significantly greater from the hours of 8 to 20 LST, significantly lower at 21 and 22 LST, and not significantly different from 23 overnight to 3 LST. Box 4 (Galveston Bay) shows the trend of being significantly lower from 8 to 19 LST, not significant at 20 and 21 LST, and significantly greater from 1 to 5 LST.

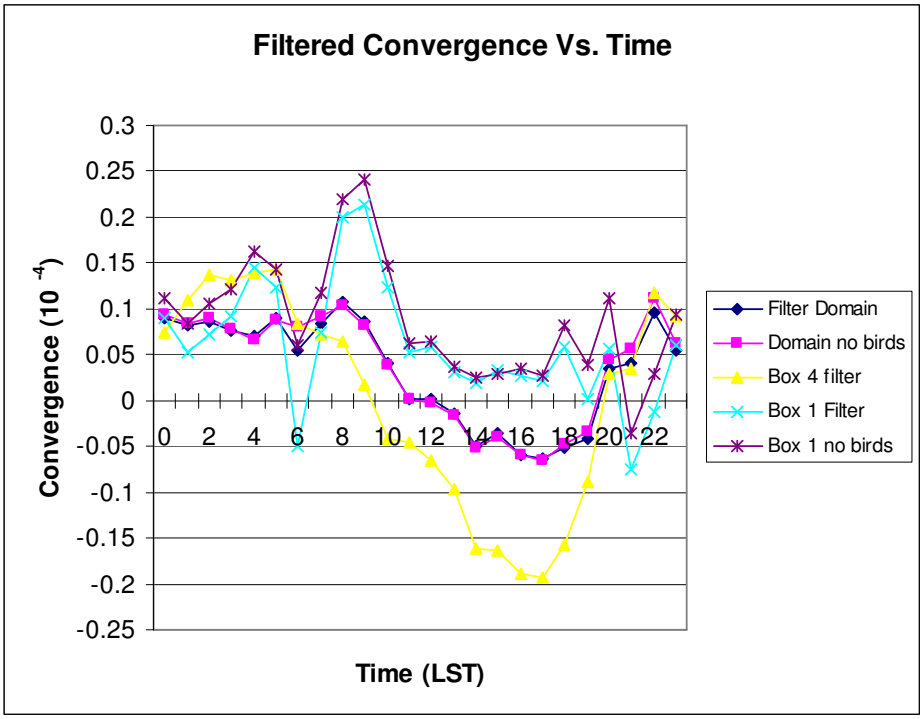

Figure 4.18. Time series of convergence (10^{-4} s^{-1}) for the domain, bird edited domain, box 1, bird edited box 1, and box 4.

Table 4.3. Hourly Wilcoxon Rank-Sum at 5% significance level results for box 1 and box 4 average convergence. N is not significantly different, H is significantly higher, and L is significantly lower as compared to the overall domain shown in Figure 4.17.

Hour (LST)	0	1	2	3	4	5	6	7	8	9	10	11	12	13	14	15	16	17	18	19	20	21	22	23
Box 1	N	N	N	N	H	N	L	N	H	H	H	H	H	H	H	H	H	H	H	H	H	L	L	N
Box 4	N	H	H	H	H	H	N	N	L	L	L	L	L	L	L	L	L	L	L	L	N	N	H	H

.

The total average convergence is presented in Figure 4.19. Two areas of known artifacts are clearly visible in the total average, a couplet over northwest Houston, and the radial convergence and divergence located in the southwest portion of the dual-Doppler lobe. These areas are believed to be bad and should be ignored. Average convergence was located over downtown Houston, while average divergence was present over west Houston. This latter feature may or may not be real, due to the strong presence of birds during dawn and dusk hours. Divergence appears to be dominant over the Bay except near the north and west coastline. The Wilcoxon Rank-Sum test reveals that the mean of box 1 is significantly higher, and the mean of box 4 is significantly lower, at the 5% level, than the domain mean.

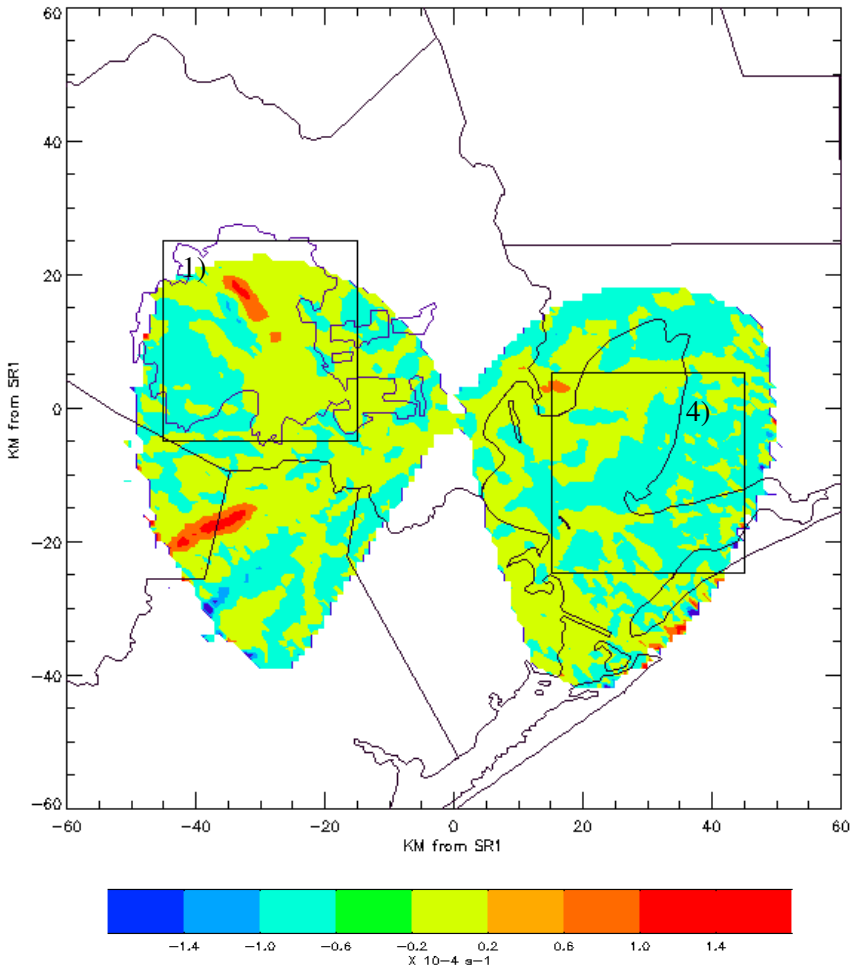

Figure 4.19. Total averaged convergence ($10^{-4}s^{-1}$). Warm (cool) colors represent mean convergence (divergence). Boxes represent the areas used for the Wilcoxon rank sum comparison.

4.2.3 *Two km Reflectivity*

The diurnal variation of low-level horizontal reflectivity structure at 2 km is presented in Figure 4.20. At midnight LST (a), the highest reflectivity values were southwest of downtown Houston, and south of the city, near the shoreline. Reflectivities generally remained weak during the next couple hours (b and c) with only isolated

pockets of high reflectivities being present. At 3 LST (d) the highest reflectivities were located off the Galveston coastline. At 4 LST (e) more significant reflectivities were located southeast of downtown Houston and west of Galveston Bay. At 5 LST (f) convection was located over the north part of Galveston Bay, north of Galveston Bay, and over downtown, with the strongest convection located west of Galveston Bay. At 6 LST (g) convection was located over most of Galveston Bay and west of Galveston Bay. At 7 LST (h) convection increased near and off of the shore, and increased in strength at 8 LST (i). Convection increased spatially over the next several hours from morning to mid-afternoon (j-p), with minima in convection apparent over Galveston Bay and high reflectivity values frequently located over and northwest of the Houston area. At 16 LST (q), a lack of convection off shore of the Galveston Bay is apparent. By 17 LST (r) the decrease in convection spread to cover the areas north of Galveston Bay. Clearing continued over most of the domain during the next several evening hours (s-v), with most of the convection located over and to the south of the Houston area. Convection was over the eastern and northern part of the domain at 22 LST (w) and continued to central part of the domain at 23 LST (x).

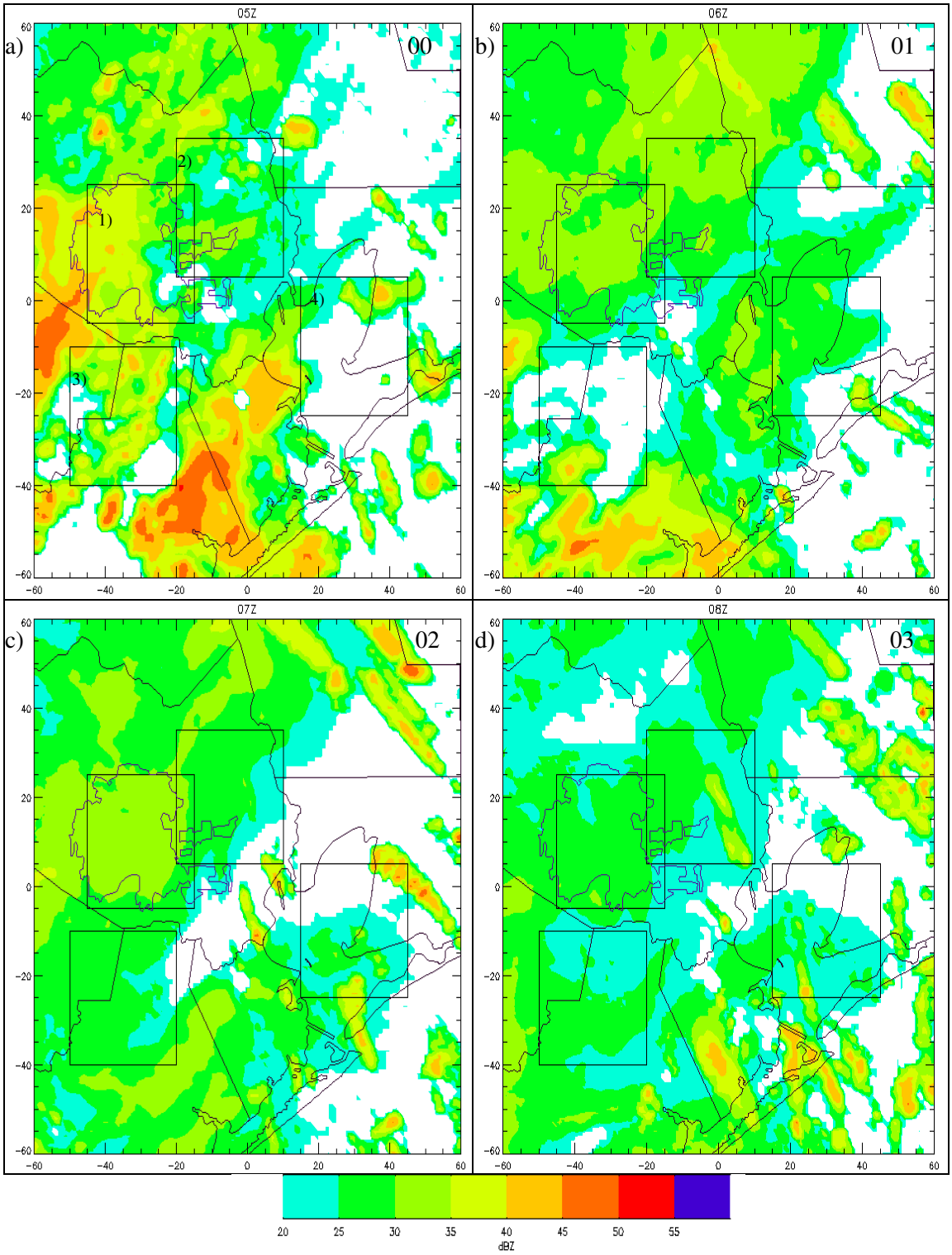

Figure 4.20. Average reflectivity (dBZ) at 2 km. (a-d) 00 to 03 LST. Distance is kilometers from SR1. Boxes are labeled in a. Times in the upper right corners are local.

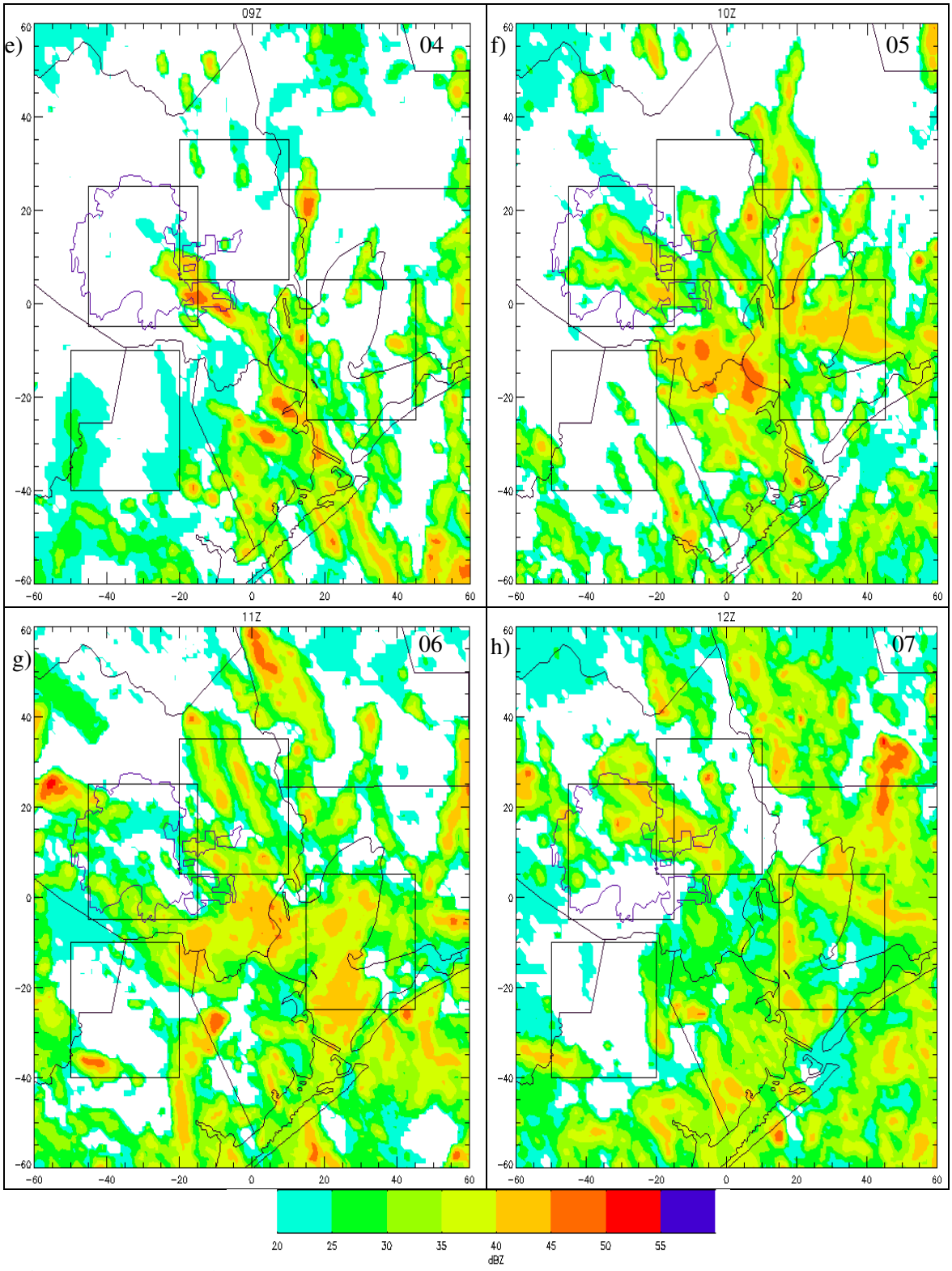

Figure 4.20 cont. (e-h) 04 to 07 LST.

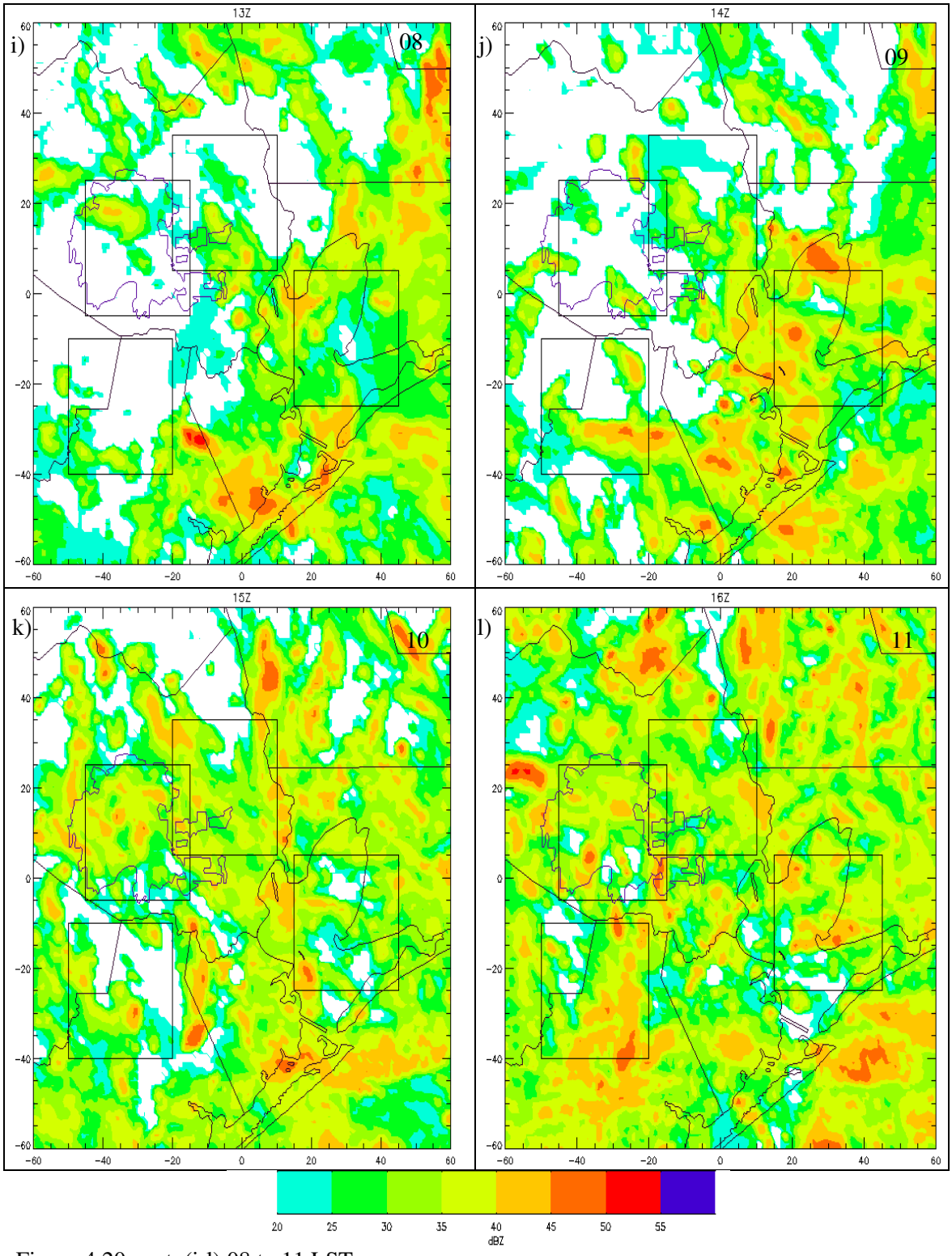

Figure 4.20 cont. (i-l) 08 to 11 LST.

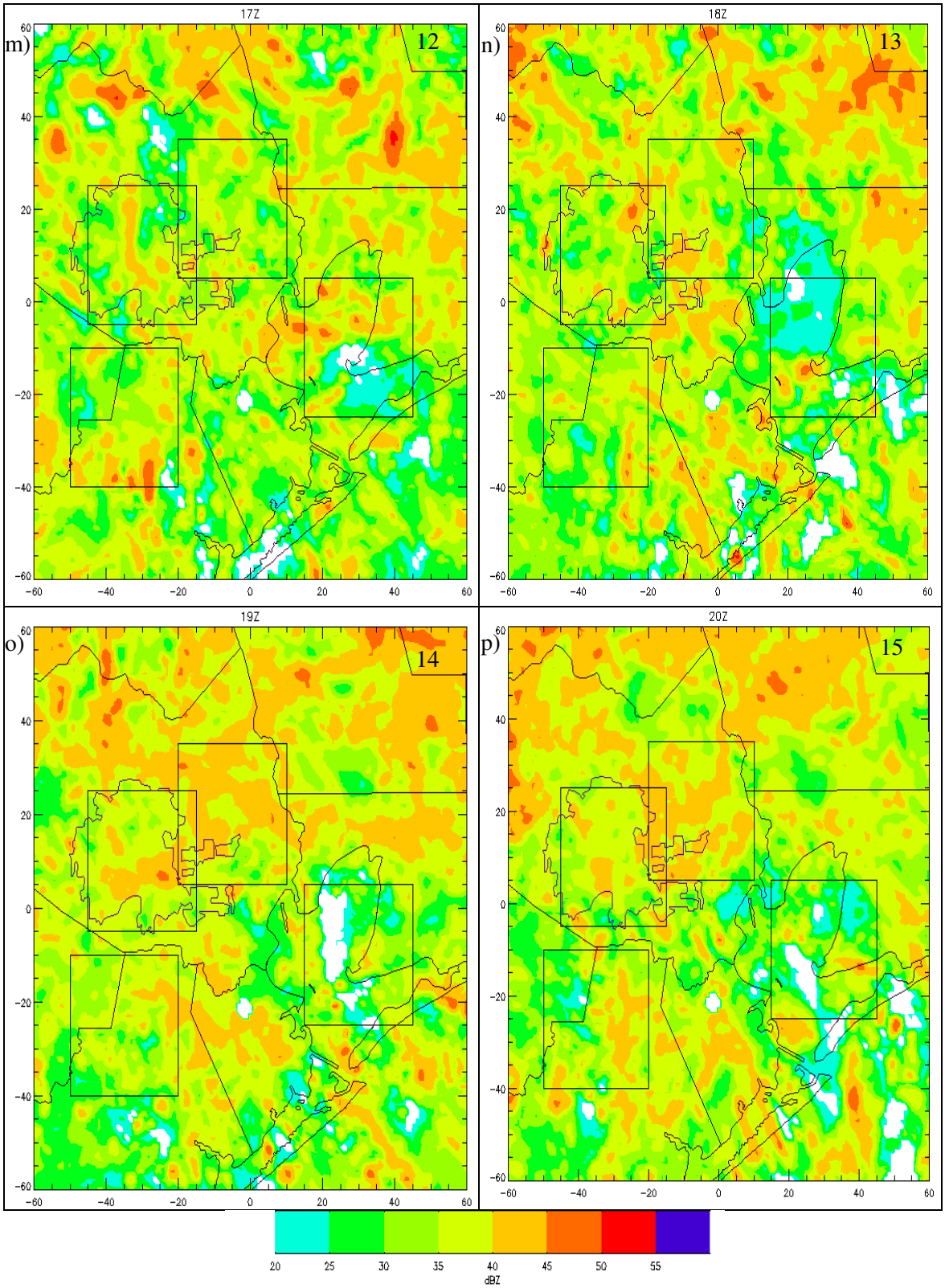

Figure 4.20 cont. (m-p) 12 to 15 LST.

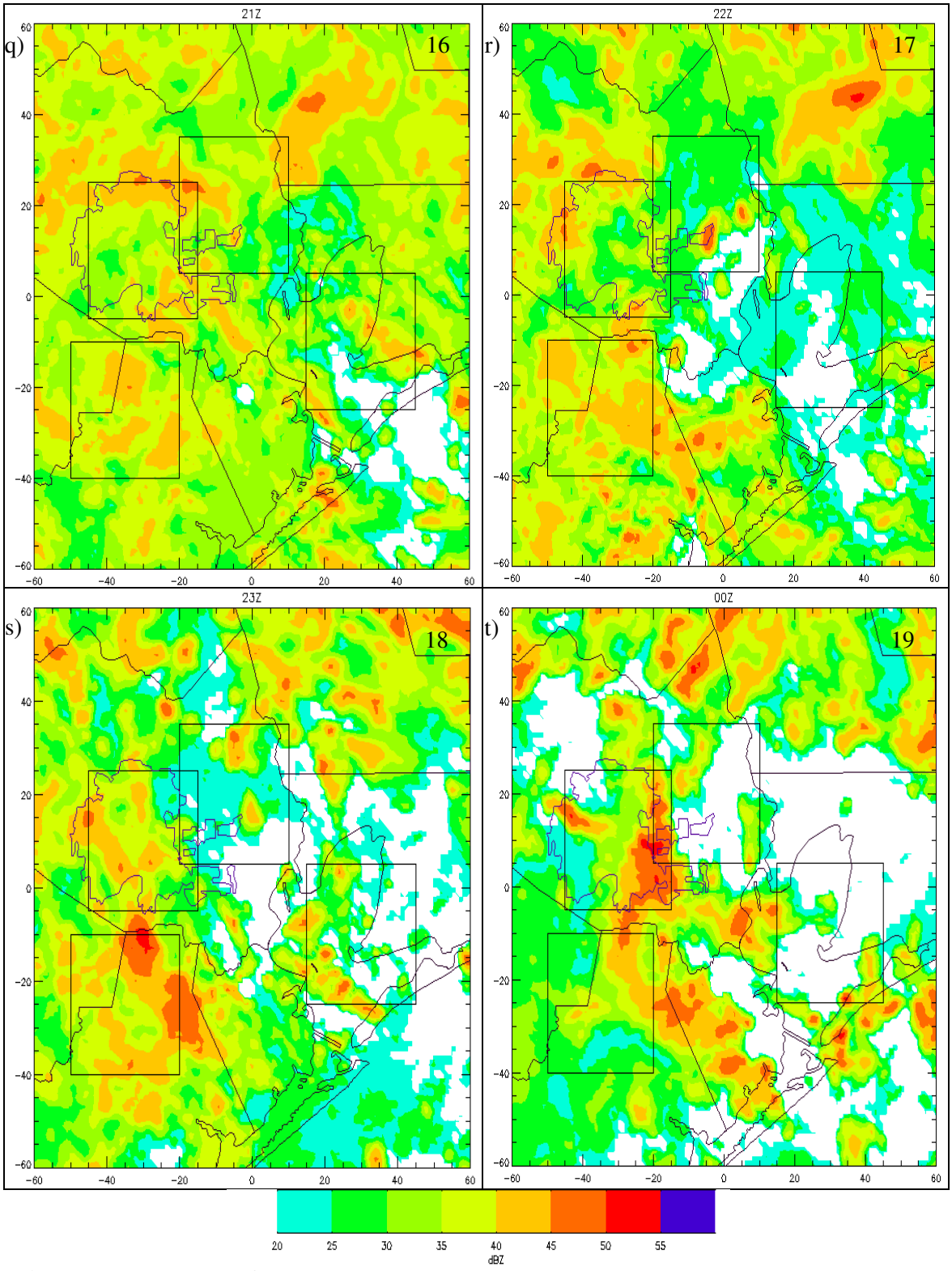

Figure 4.20 cont. (q-t) 16 to 19 LST.

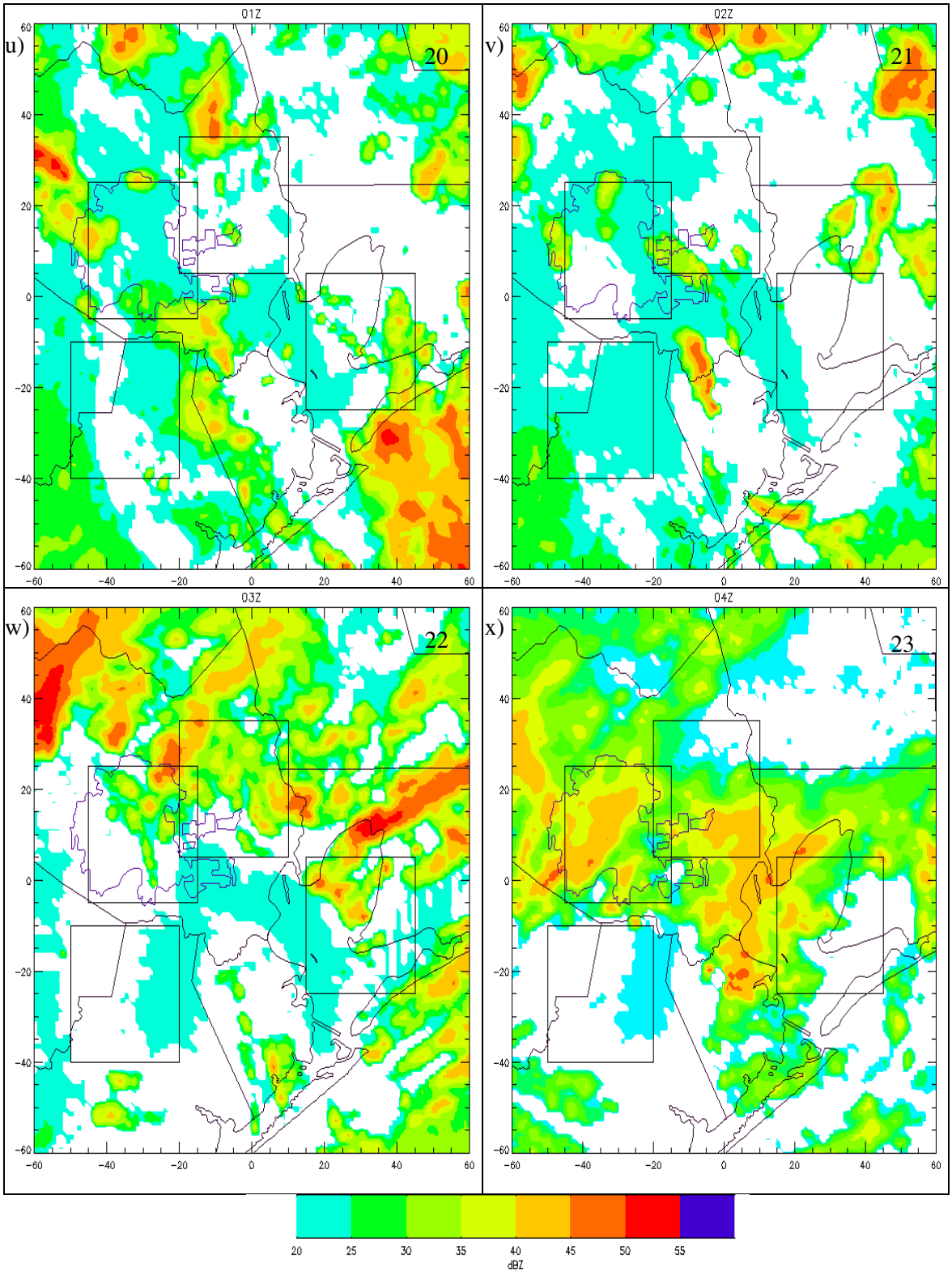

Figure 4.20 cont. (u-x) 20 to 23 LST.

Figure 4.21 is the corresponding percentage of frequency of occurrence of the convection presented in Figure 4.18. Due to the fact that the total count of files was near 550 and there were near 10-12 files per hour, 2 percent is roughly equal to one convection event. Most of the convection from midnight until 6 LST (a-g) appears to be isolated to single events by the low frequency. At 7 LST (h) the convection over Galveston Bay was most likely caused by a couple occurrences, as well as some of the convection located off of the coast. This trend appears to be the case for the next couple hours (i and j). At 10 LST (k), convection located at the northwest portion of Galveston Bay was most likely due to a couple of cases. Isolated cases appear to be the cause of the majority of convection at 11 LST (l) with the exception of an area of convection located just north of Galveston island, which appears to have been caused by a few events and a couple of events responsible for the convection east of Galveston Bay. At noon (m) and 13 LST (n), the most frequent occurrence of convection was located north and east of Galveston Bay. During the following three afternoon hours (o-q) a minimum was present over Galveston Bay. By 17 and 18 LST (r and s), the highest frequency of convection was located west of Houston. Storms at 19 LST (t) appear to be single events. The same is true for 20 LST (u), with the exception of an area just north of downtown which appears to be caused by two or more events. At 21 LST (v), convection east of Houston appears to have been caused by multiple events occurring over the same location. Convection during the next two hours (w and x) appears to have been caused by a single event.

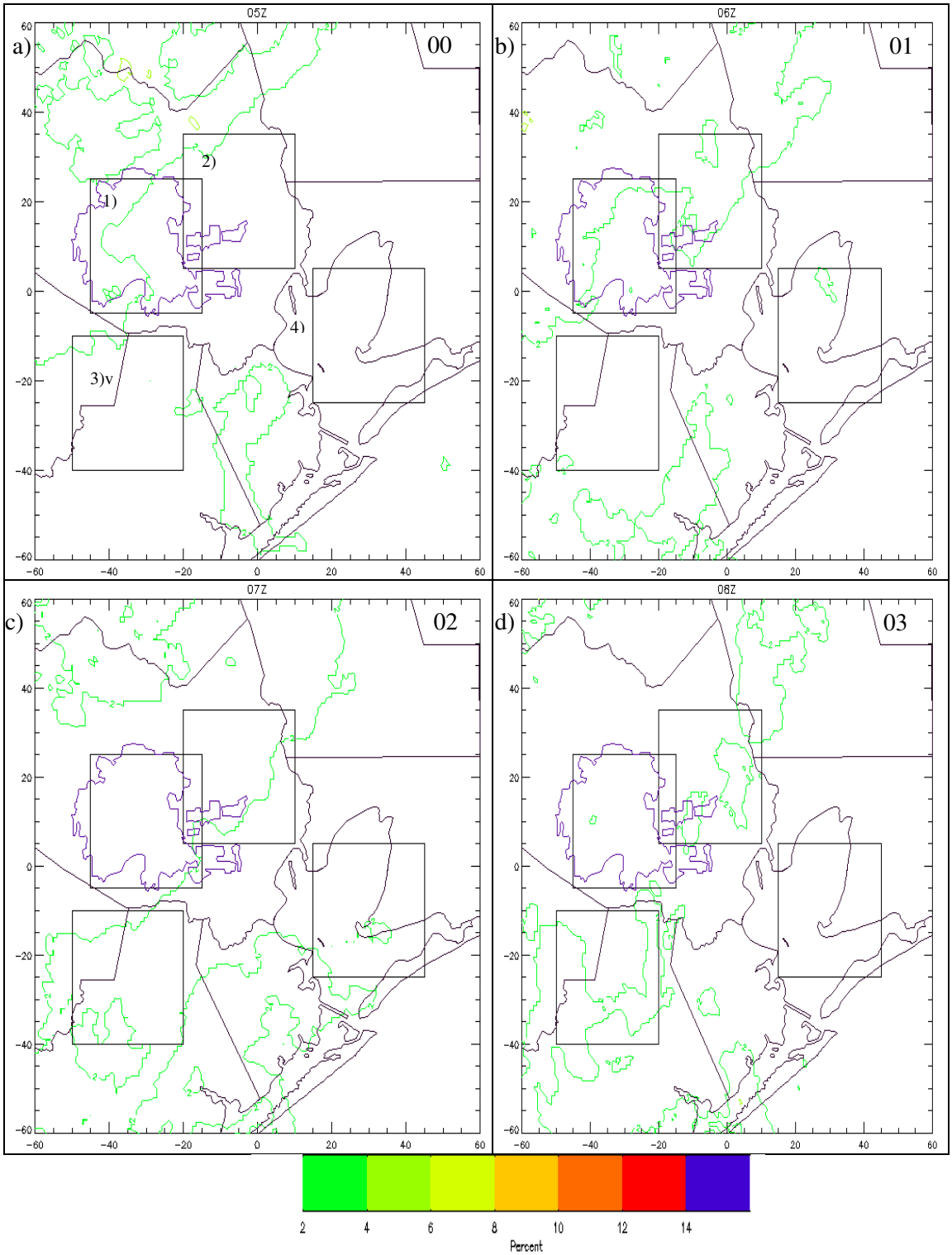

Figure 4.21. Frequency of occurrence of convection at 2 km. (a-d) 00 to 03 LST. Distance is kilometers from SR1. Boxes are labeled in a. Times in the upper right corners are local.

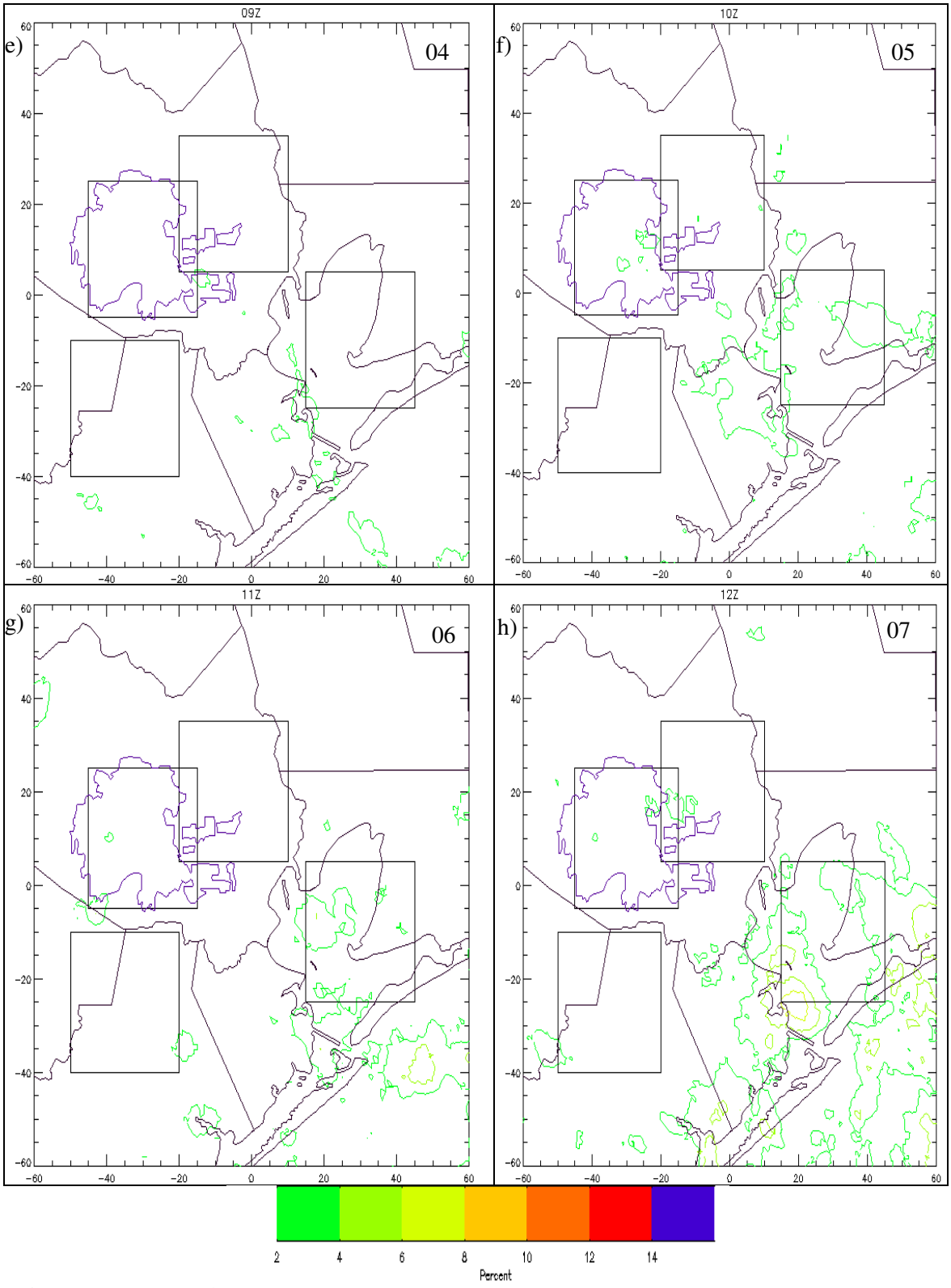

Figure 4.21 cont. (e-h) 04 to 07 LST.

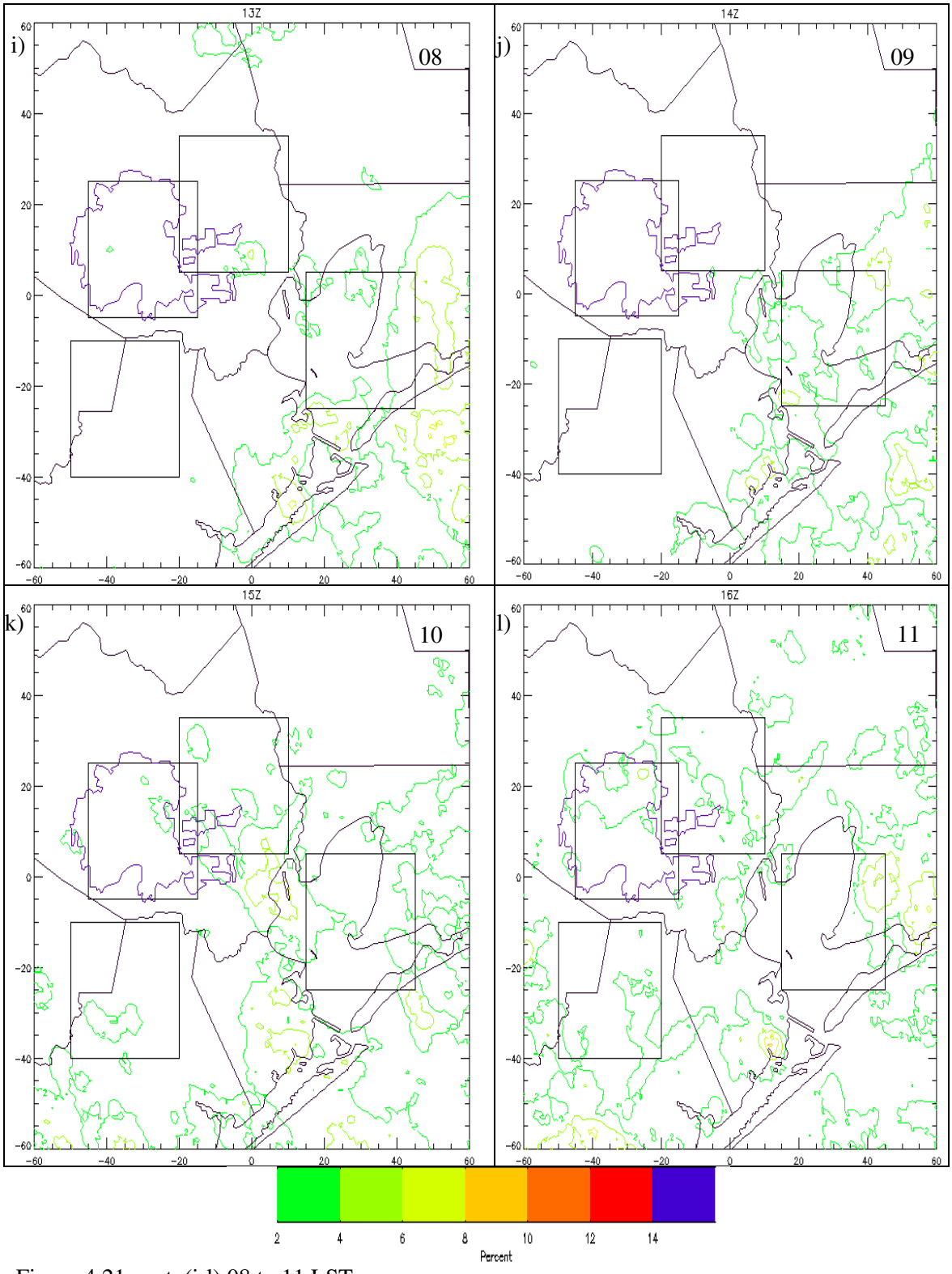

Figure 4.21 cont. (i-l) 08 to 11 LST.

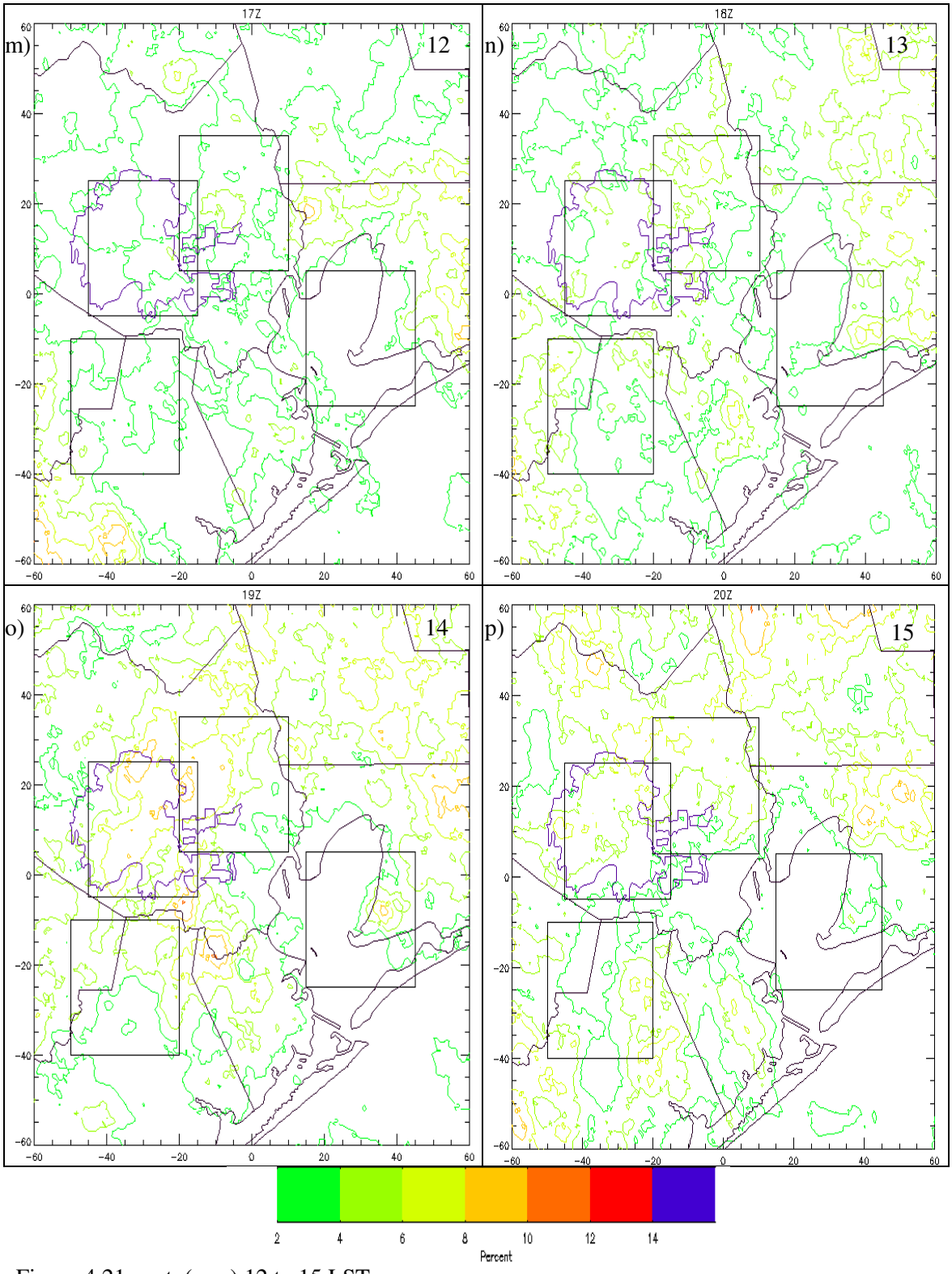

Figure 4.21 cont. (m-p) 12 to 15 LST.

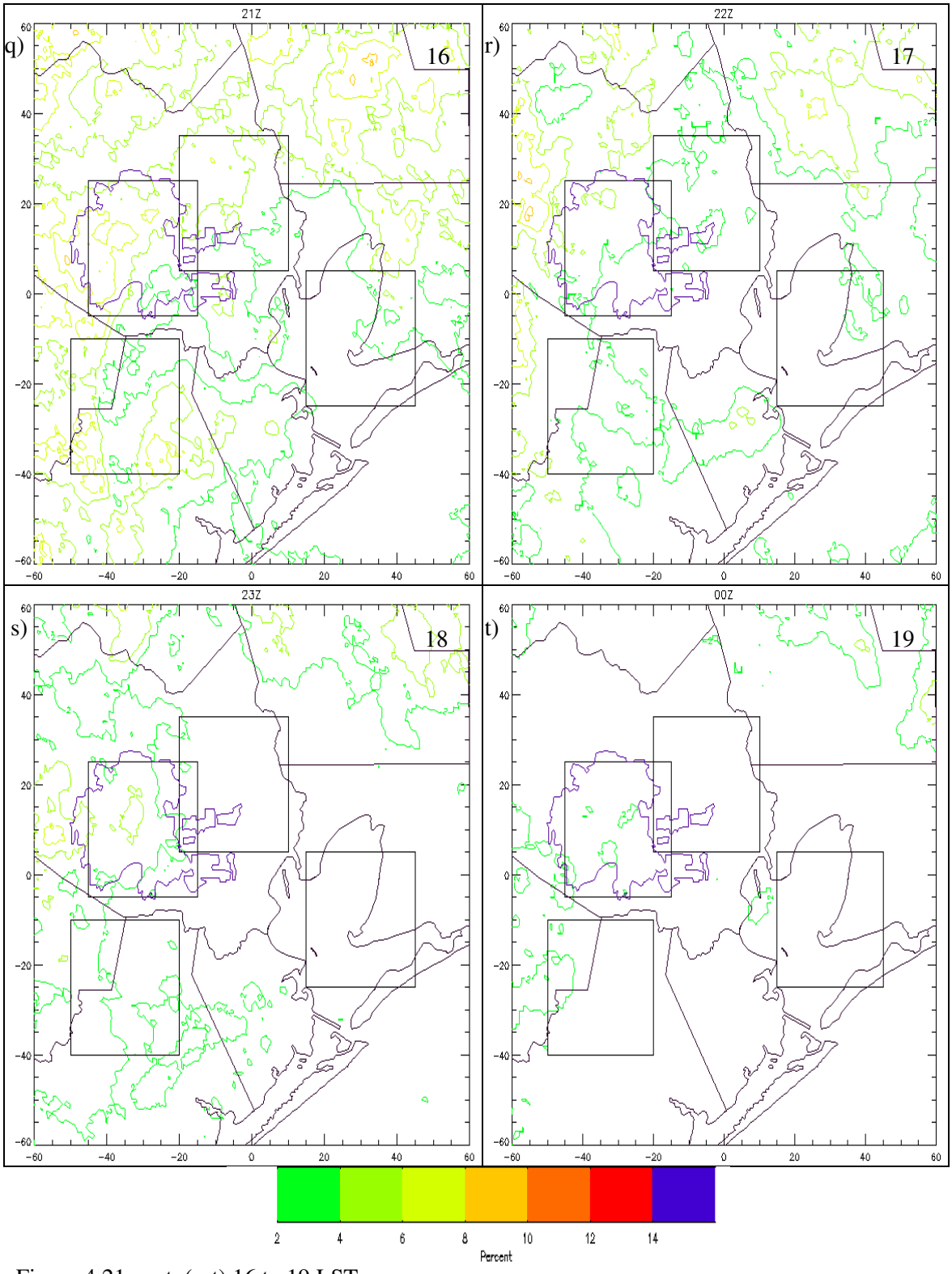

Figure 4.21 cont. (q-t) 16 to 19 LST.

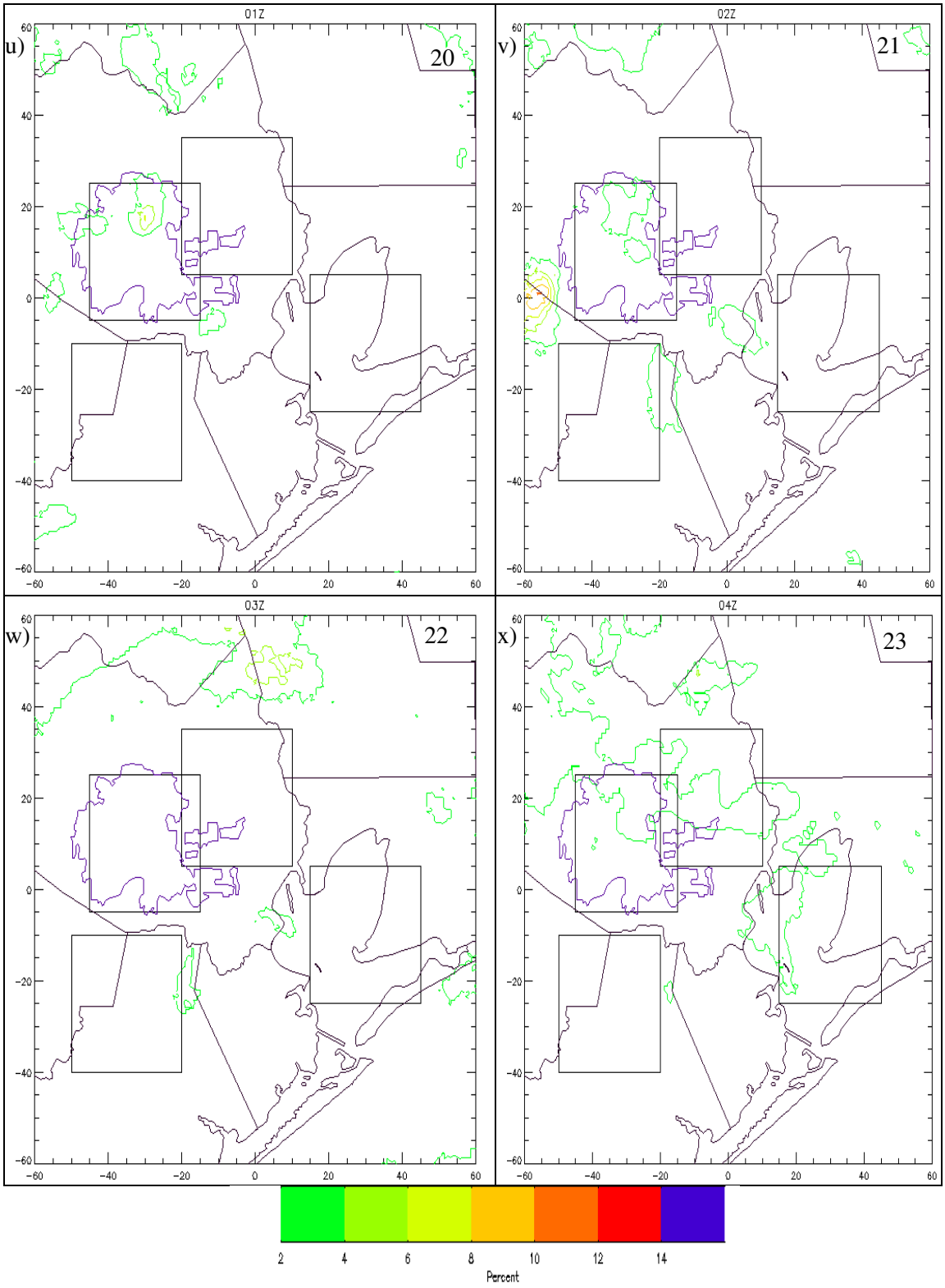

Figure 4.21 cont. (u-x) 20 to 23 LST.

Time series plots for average radar reflectivity over the four boxed areas and the entire domain are presented in Figure 4.22. The domain mean shows a decrease in convection intensity overnight to early morning, with the overall minimum in intensity occurring at 4 LST of 14 dBZ. Convective strength increased and then reached a peak of 36 dBZ at 14 LST. A second minimum of near 15 dBZ was evident at 22 LST. Convection in box 1 showed a similar pattern, but convection was stronger during the overnight hours (23-3 LST), weaker from 4-9 LST, and similar to slightly stronger than the domain mean from 12-19 LST. The box 2 pattern was very similar to box 1 with the exception that the box 2 mean decreased earlier in the day, at 17 LST, and reached a lower minimum of 10 dBZ slightly earlier at 20 LST. Box 3 was also similar to box 1 except that the diurnal maximum appeared to be delayed to the early evening (18 LST). Convective intensity was slightly higher than box 1 for the hours of 17 and 18 LST, and lower at 23 LST. The pattern in box 4 was more unique. Convection was weaker in the mean than the domain until 4 LST. Convective in box 4 rose to 30 dBZ at 5 LST and remained fairly steady until 16 LST, although there was a slight tendency for stronger convection to occur in the morning hours between 06 and 12 LST. Convective strength began to slowly decrease and remained lower than all other boxes, with one exception at 20 LST, until 21 LST.

Table 4.4 presents the Wilcoxon Rank-Sum results for each box. The mean for box 1 was significantly higher than the domain mean between 14 and 19 LST, and 23 to 3 LST. It was significantly lower for the times of 6 to 9 LST and 11 to 13 LST. The box 2 average was significantly lower than the domain average from 17 to 21 LST. Box 3 was

also very similar to box 1. However, box 3 was significantly lower than the domain average from 13 to 15 LST. Box 4 was only significantly higher than the mean from 4 to 9 LST, it was significantly lower at all other times.

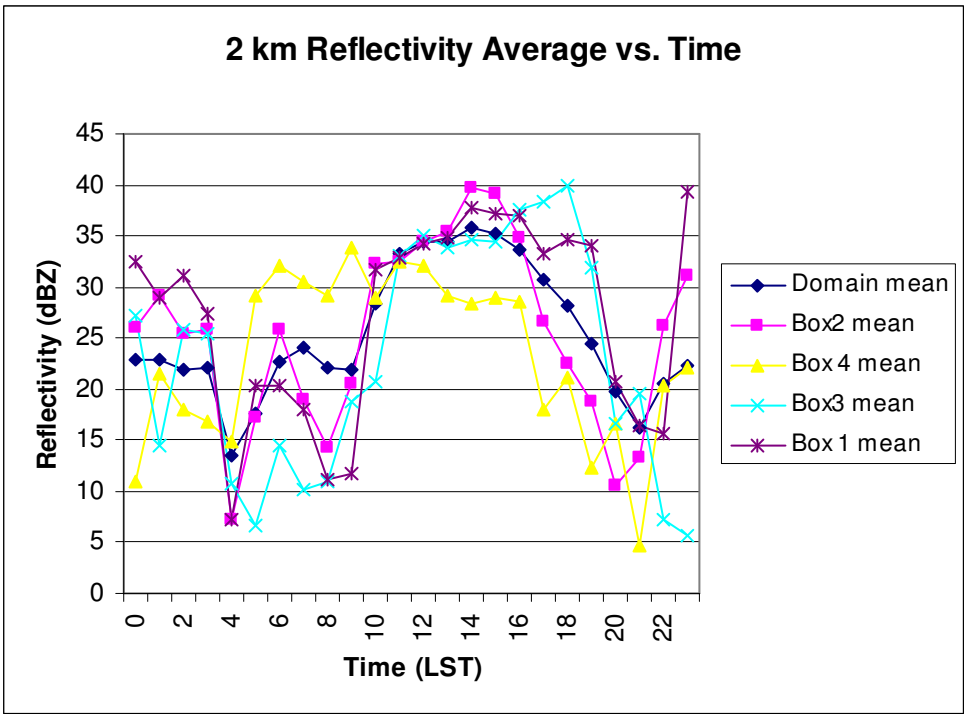

Figure 4.22. Time series plot of domain and box average reflectivity (dBZ) at 2 km.

Table 4.4. Hourly Wilcoxon Rank-Sum at 5% significance results for box average radar reflectivity, which was used as a proxy for convective intensity, at 2 km. N indicates not significantly different, H is significantly higher, and L is significantly lower than the domain mean.

Hour (LST)	0	1	2	3	4	5	6	7	8	9	10	11	12	13	14	15	16	17	18	19	20	21	22	23
Box 1	H	H	H	H	L	H	L	L	L	L	H	L	L	L	H	H	H	H	H	H	N	N	L	H
Box 2	N	H	H	H	L	N	H	L	L	L	H	L	L	H	H	H	N	L	L	L	L	L	H	H
Box 3	H	L	N	H	L	L	L	L	L	L	L	H	H	L	L	L	H	H	H	H	L	H	L	L
Box 4	L	L	L	L	H	H	H	H	H	H	L	L	L	L	L	L	L	L	L	L	L	L	L	N

Figure 4.23 presents time series of the domain and box averages for the frequency of convection at 2 km. Domain frequency was about 5 or 6 percent (about 2 to 3 events) from midnight until a minimum of near 2 percent (1 event) at 4 LST. From this time, domain average convective frequency increased to a maximum of near 18 percent at 14 LST. The convective frequency then began to drop and reached a steady level of near 4 percent at 20 LST until midnight. The overall pattern in box 1 was similar to the domain average. The frequency after midnight was slightly higher than the domain average, about 7-11 percent. The convective frequency then dropped to about 2 percent until 10 LST, at which point it began to rise. Box 1 convective frequency reached a maximum of 33 percent at 14 LST, which is the largest value of any of the regions. After this time, convective frequency in box 1 began to decrease. Convective frequency in box 2 was nearly identical to box 1. The maximum in box 2 was not as high as box 1, only 27

percent, and the frequency in box 2 decreased more rapidly than box 1, and reached a fairly steady minimum of 3 to 5 percent at 18 LST. Convective frequency in box 3 was also very similar to box 1. The maximum occurred slightly later, at 16 LST, and was lower, 21 percent. The convective frequency in box 4 was much lower than the frequency in all other boxes and exhibited a markedly different diurnal cycle. Box 4 frequency was very low, about 2 to 4 percent from midnight until 5 LST. At 5, the frequency was higher than any other box. The maximum for box 4 was at 7 LST at 11 percent. The frequency over box 4 slowly declined over the course of the day and reached a steady minimum of 2 percent at 18 LST until 22 LST.

Table 4.5 presents the results of the Wilcoxon Rank-Sum test for the domain and all boxes. The mean for box 1 was significantly higher than the domain mean for almost all hours except 5 to 12 LST. Box 2 significance was generally similar to box 1. However, the mean for box 2 was significantly lower than the domain mean from 16 to 20 LST. Box 3 was different from box 1 during the hours of 22 LST overnight to 2 LST, at which times it was either significantly lower, or not significantly different, from the domain mean. Box 4 was only significantly higher than the domain mean between the hours of 5 to 9 LST.

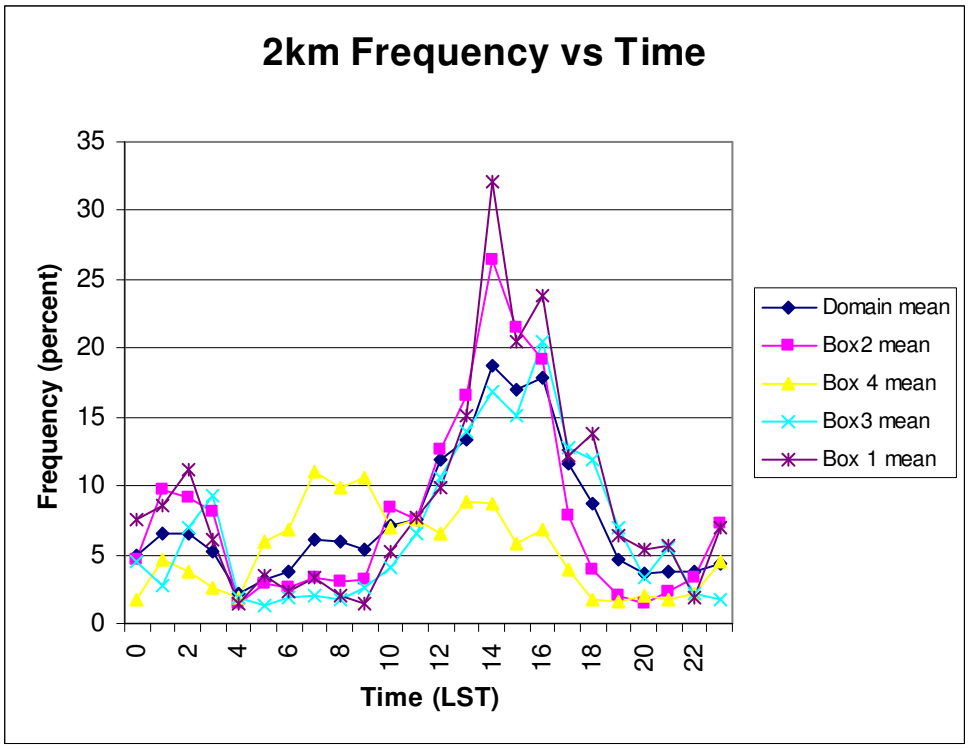

Figure 4.23. Time series plot of domain and box convective frequency at 2 km.

Table 4.5. Hourly Wilcoxon Rank-Sum at the 5% significance level results for box average convective frequency at 2 km. N indicates not significantly different, H is significantly higher, and L is significantly lower than the domain mean.

Hour (LST)	0	1	2	3	4	5	6	7	8	9	10	11	12	13	14	15	16	17	18	19	20	21	22	23
Box 1	H	H	H	H	L	H	L	L	L	L	L	N	L	H	H	H	H	H	H	H	H	H	H	H
Box 2	H	H	H	H	L	N	L	L	L	L	H	H	H	H	H	H	L	L	L	L	L	H	H	H
Box 3	N	L	N	H	N	L	L	L	L	L	L	L	H	H	L	L	H	H	H	H	N	H	L	L
Box 4	L	L	L	L	L	H	H	H	H	H	N	L	L	L	L	L	L	L	L	L	L	L	L	N

The total average reflectivity at 2 km is presented in Figure 4.24. The highest reflectivity was located in the northwest and northeast portions of the domain. Enhanced reflectivity was also located near downtown, northeast of Houston, south of Houston, and along the northern and northwest shoreline of Galveston Bay. The lowest values of reflectivity occurred in the southern portion of Galveston Bay and the southwest corner of the domain. The results of the Wilcoxon Rank-Sum test shows that the means of box 1, box 2, and box 3 were significantly greater than the domain mean, and box 4 was significantly lower than the domain mean.

The total average convective frequency at 2 km is shown in Figure 4.25. The highest frequency of convection occurred downtown, east of Galveston Bay, west of Galveston Bay, and also in the north and northeast portion of the domain. The lowest frequency of convection occurred over and offshore of Galveston Bay. Another minimum also occurred southwest of Houston. The Wilcoxon Rank-Sum results show that the mean of box 1 was significantly greater than the domain mean, box 2 was not significantly different from the mean, and the means of box 3 and box 4 were significantly less than the domain mean.

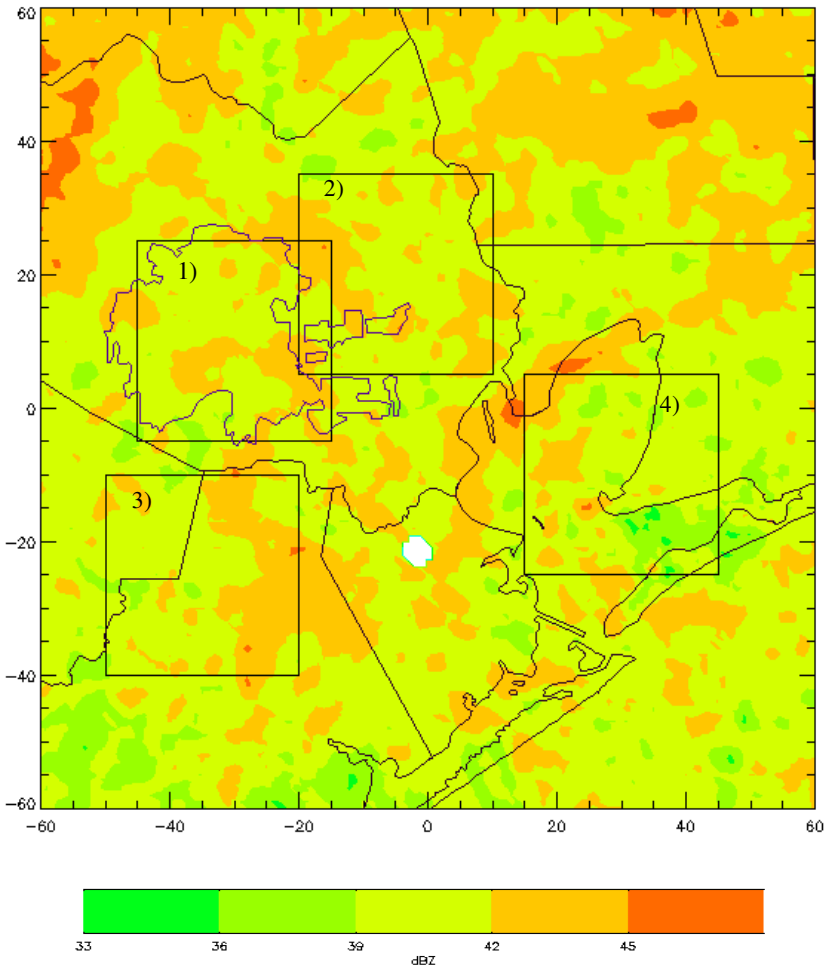

Figure 4.24. Averaged reflectivity (dBZ) at 2 km. Blank circle is the location of the radar cone of silence.

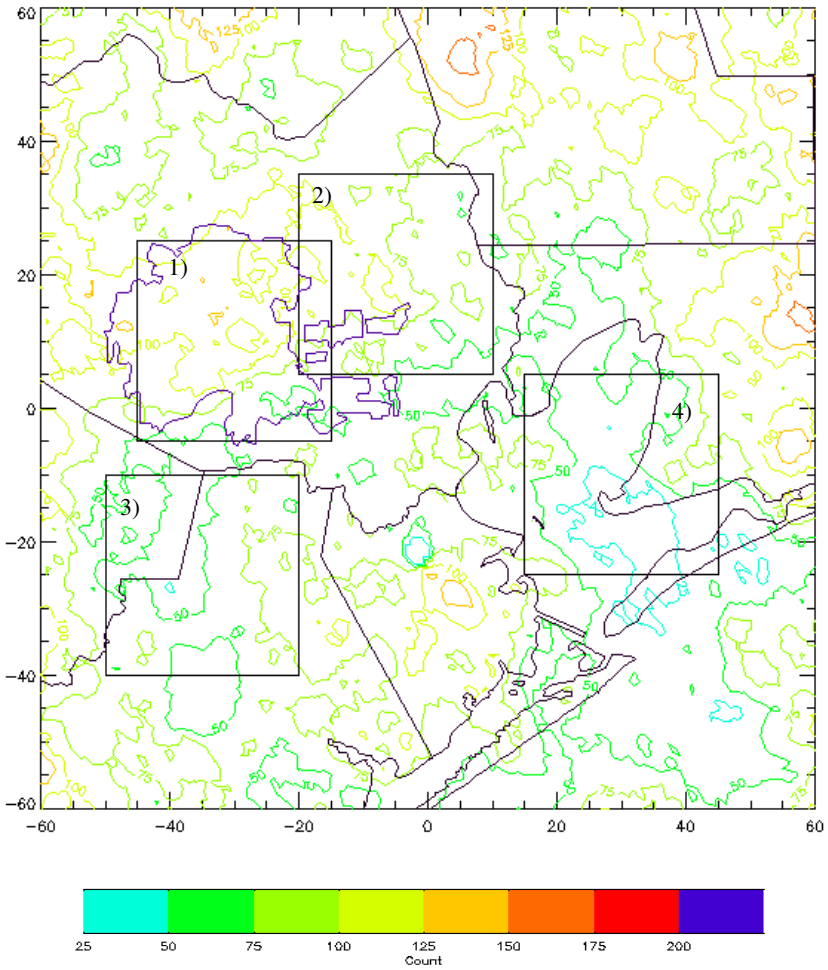

Figure 4.25. Counts of the frequency of occurrence of convection.

4.2.4 *Seven km Reflectivity*

The diurnal variation of mean radar reflectivity at 7 km over the study domain is presented in Figure 4.26. At midnight local time (a), high values of reflectivity were located in the southern portion of the domain, near the Texas shoreline with the Gulf of Mexico. There was also a small area of greater than 40 dBZ reflectivity located over the

northern portion of Galveston Bay. During the following two hours (b and c), no areas of enhanced reflectivity were present. At 3 LST (d) elevated areas of enhanced reflectivity were present off shore of and near Galveston Bay. At 4 LST and 5 LST (e and f), areas of large reflectivity were located over the northern part of Galveston Bay and over south and west Houston. At 6 LST (g), reflectivities of 45 dBZ were located over the south and northwest shoreline of Galveston Bay. Areas of elevated reflectivity were located over and near Galveston Bay for the next three morning hours (h–j). At 10 LST (k) the areas of greatest reflectivity were located north of Galveston Bay, east of Houston, and over west Houston. At 11 and 12 LST (l and m) high levels of reflectivity were present over most of the domain. However, at 12 LST (m), there was virtually no convection at 7 km located over the central and southern portions of the Galveston Bay. At 13 and 14 LST (n and o) the highest levels of reflectivity were located over and northeast of Houston. At 15 LST (p) the highest reflectivities were west of Houston. By 16 LST (q) the highest reflectivities were located south of Houston, reaching 50 dBZ at 17 LST (r). Areas greater than 50 dBZ were present south, over, and northeast of Houston at 18 LST (s). At 19 and 20 LST (t and u) reflectivity was much reduced over the entire domain, with the highest values located off of the Galveston Bay shore and north and northwest of Houston. By 21 LST (v) most areas of high reflectivity were located near the northern border of the domain. At 22 and 23 LST (w and x) high values of reflectivity were located northwest of Houston and the north portion of Galveston Bay with values reaching 60 dBZ at 23 LST (w).

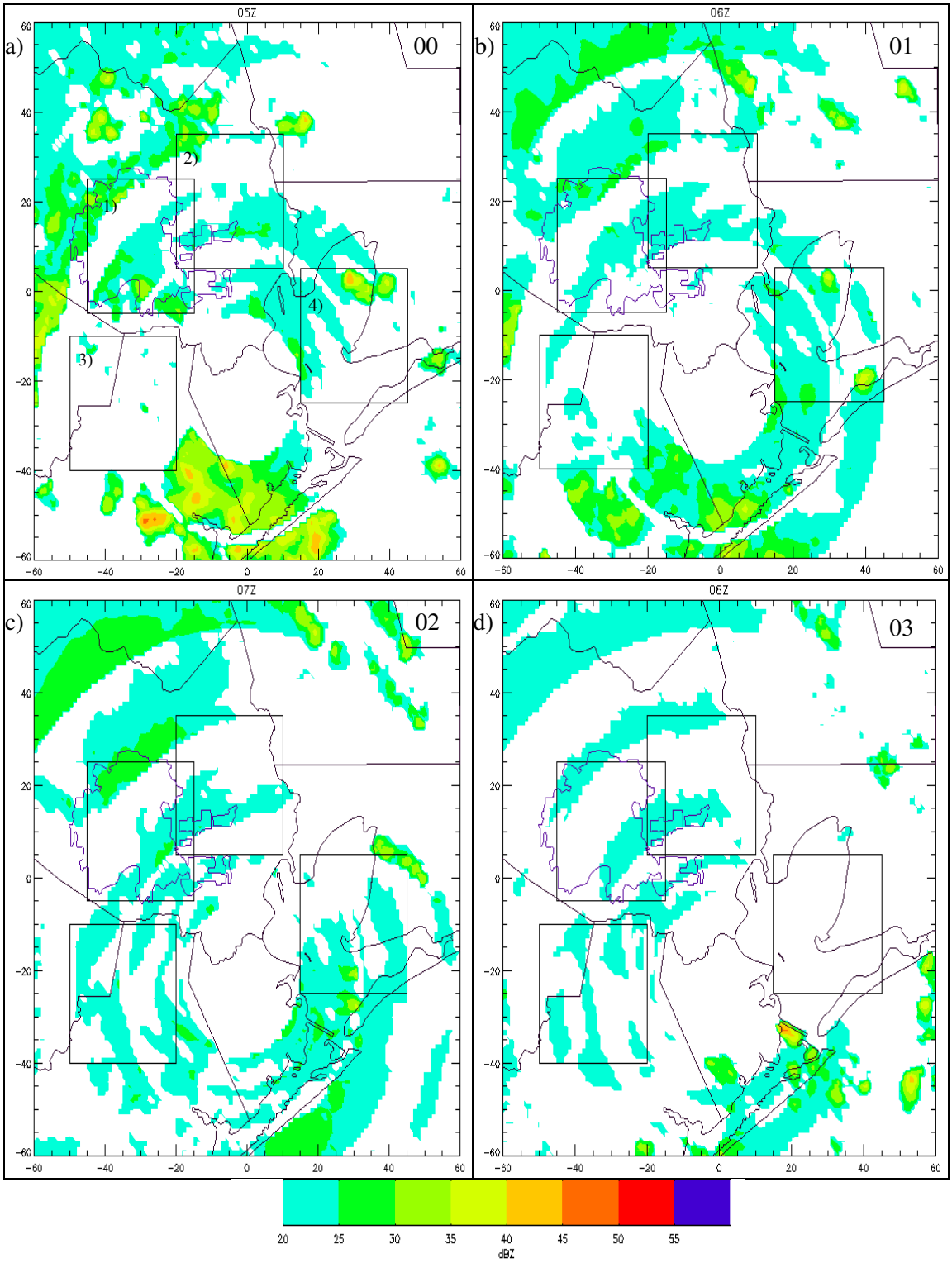

Figure 4.26. Average radar reflectivity at 7 km. (a-d) 00 to 03 LST. Boxes are labeled in a. Times in the upper right corners are local. Blank circle is location of the radar cone of silence.

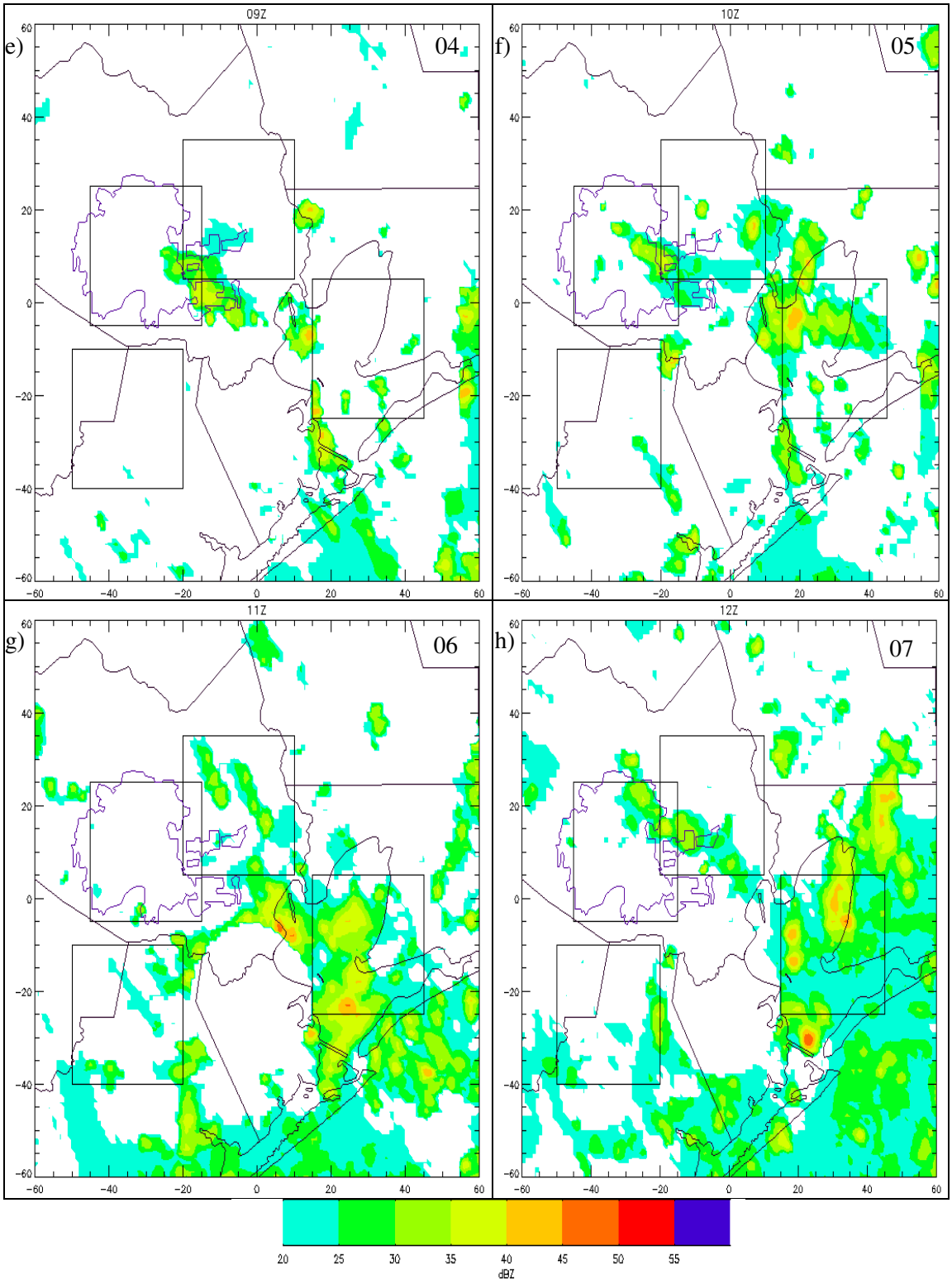

Figure 4.26 cont. (e-h) 04 to 07 LST.

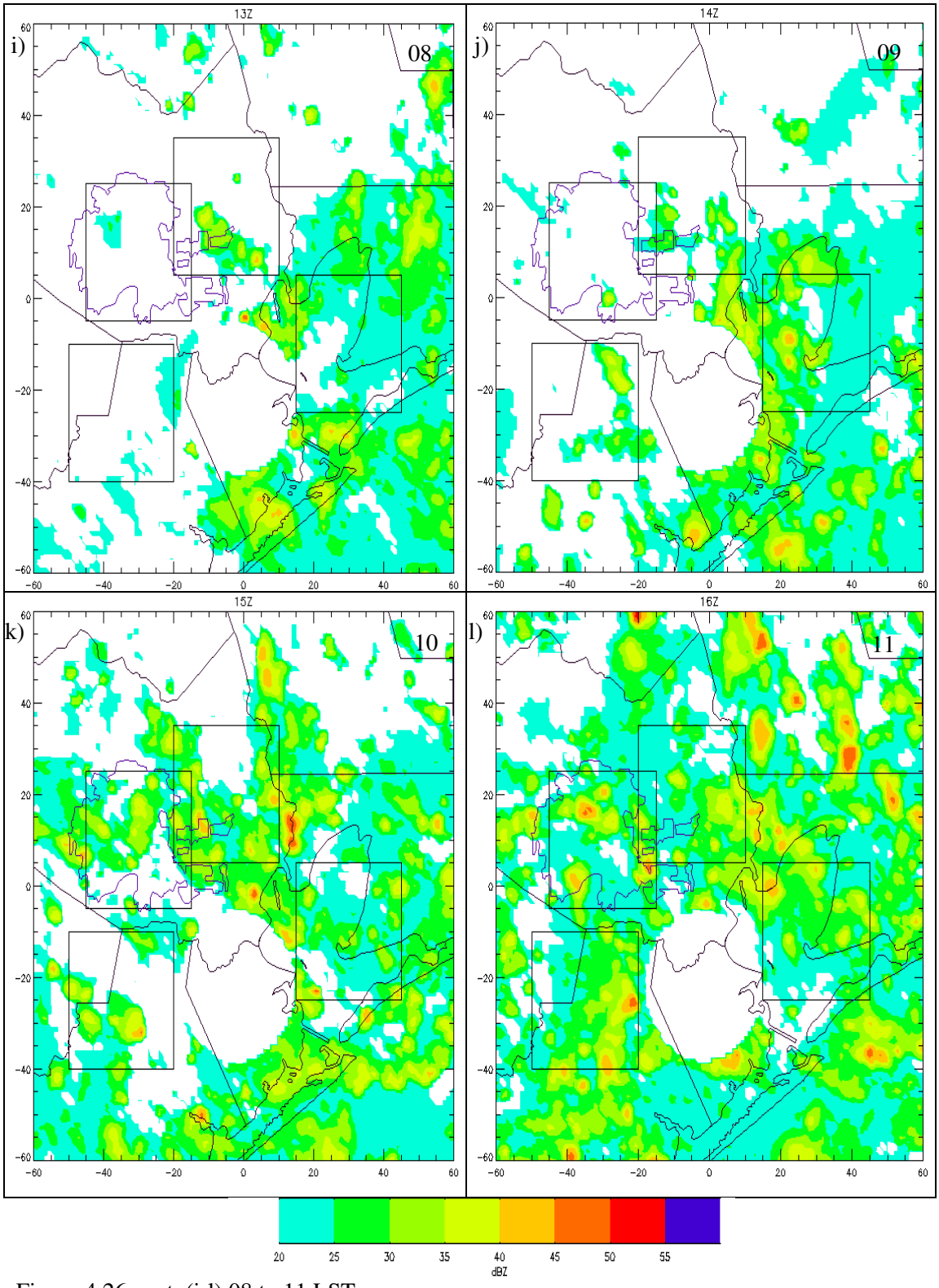

Figure 4.26 cont. (i-l) 08 to 11 LST.

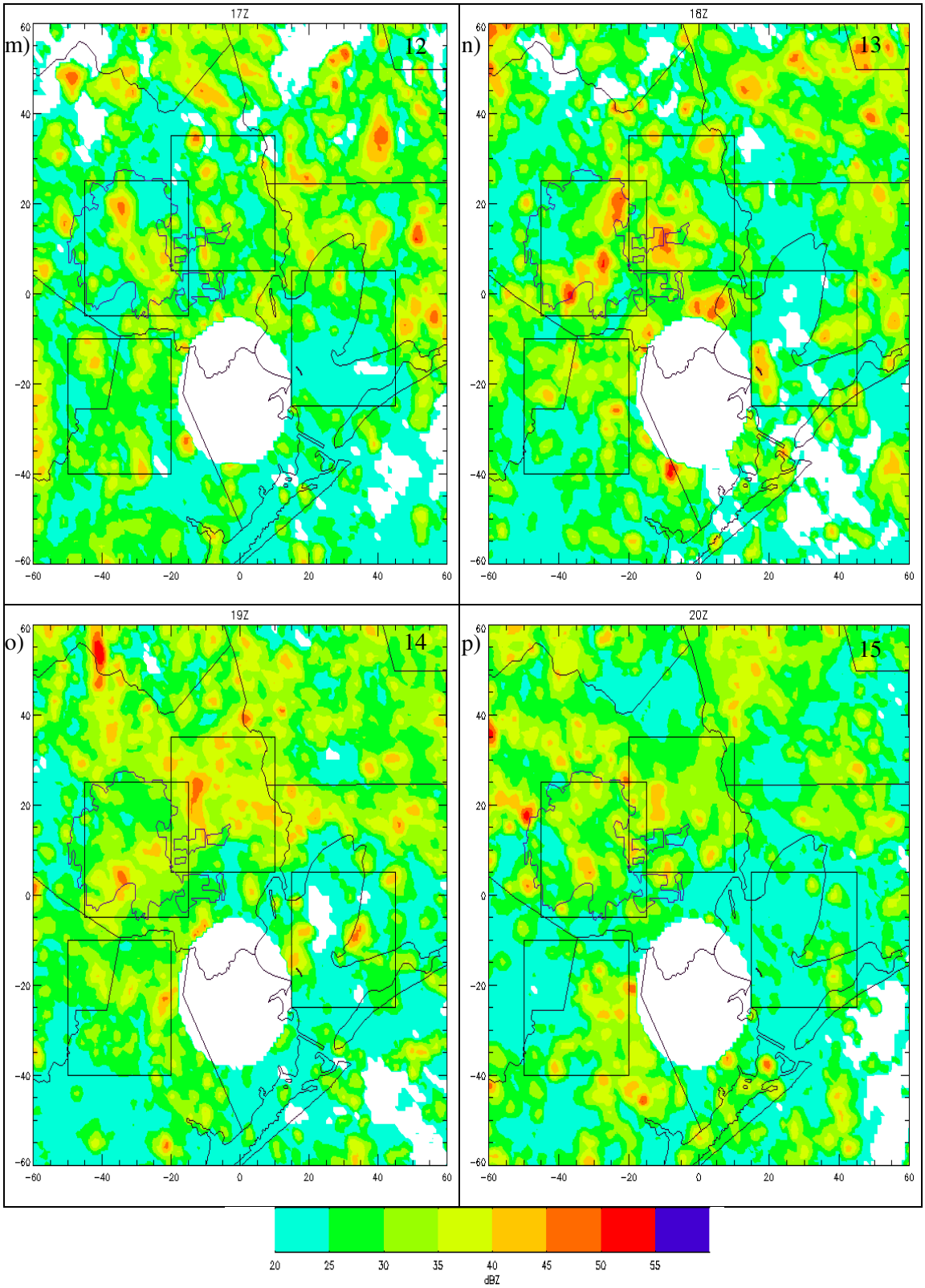

Figure 4.26 cont. (m-p) 12 to 15 LST.

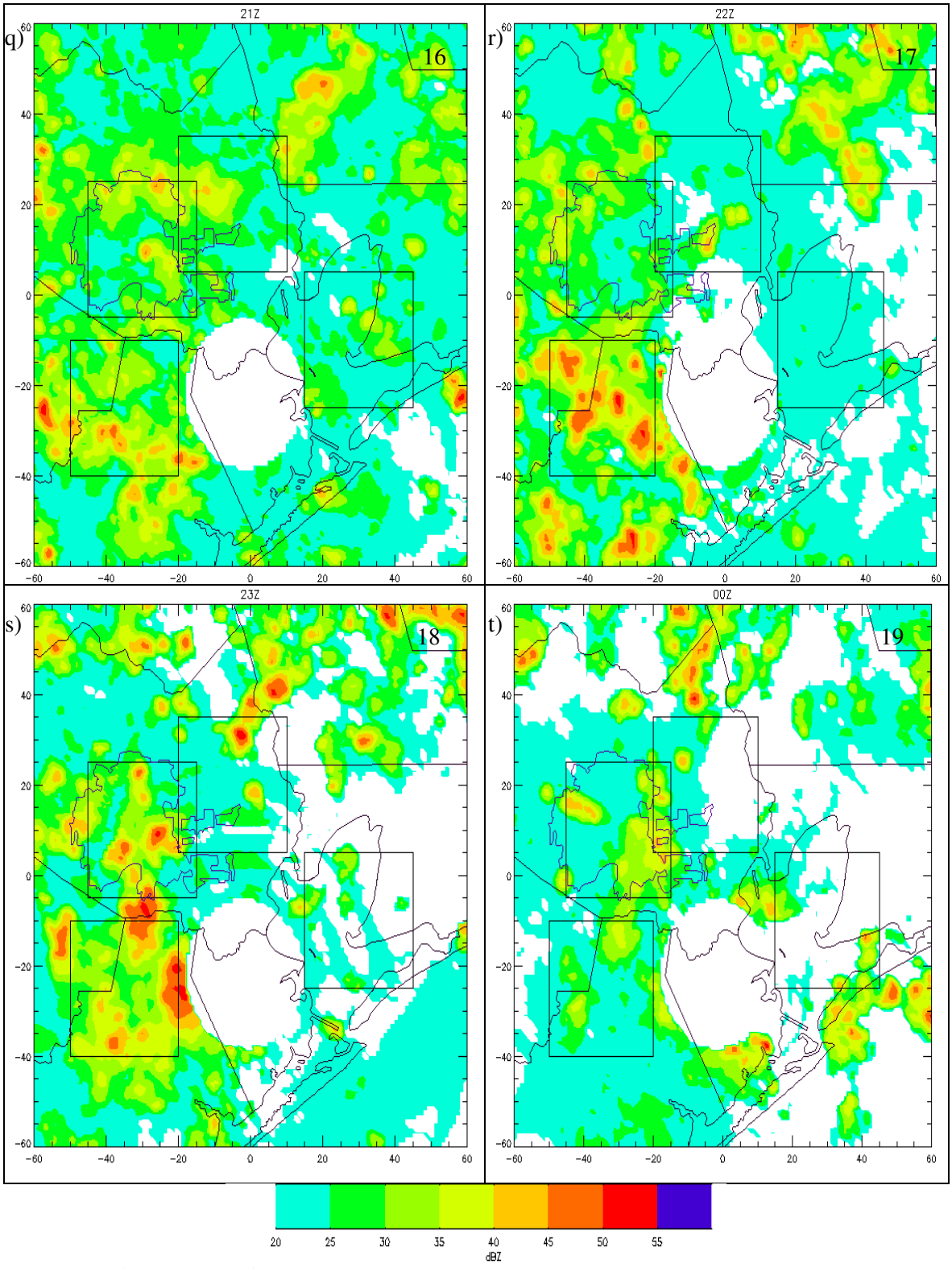

Figure 4.26 cont. (q-t) 16 to 19 LST.

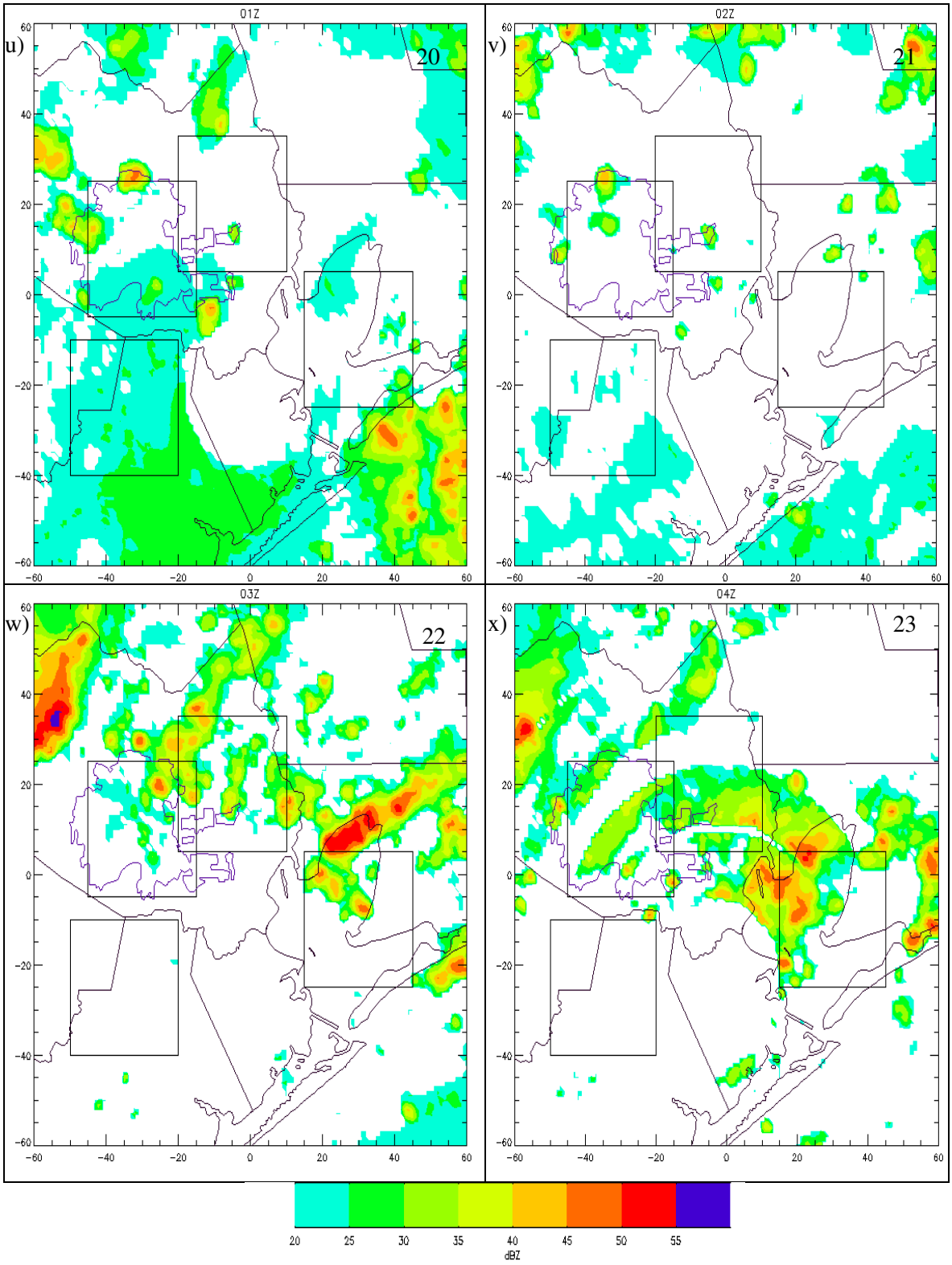

Figure 4.26 cont. (u-x) 20 to 23 LST.

Figure 4.27 presents vigorous (i.e., > 30 dBZ) convective frequency at 7 km. At midnight local time (a) the highest frequency of above 30 dBZ echo occurred in the south part of the domain near the coast. During the following four early morning hours (b-e), there was little present in the way of high reflectivities at 7 km. At 5 LST (f) low counts of high reflectivity aloft were present over northern Galveston Bay. At 6 and 7 LST (g and h), the highest reflectivities aloft were present over Galveston Bay. At 8 LST (i), there was an area of high reflectivity located over Galveston Island. Vigorous convection at 7 km was located mainly near the Galveston Island and north Galveston Bay coastlines at 9 and 10 LST (j and k). By 11 LST (l) areas of strong reflectivity aloft were scattered across much of the domain, with the largest counts located near the north shore of Galveston Bay. At 12 LST (m) the areas of strong convection at 7 km were located north and northeast of Galveston Bay and also over downtown Houston.

The spatial extent increased over the next few hours (n–p), with high frequencies of vigorous convection aloft located east of the Bay and east of downtown Houston at 13 LST (n), northeast, downtown, and south of Houston at 14 LST (o), and south and northeast of Houston at 15 LST (p). At 16 LST (q), the highest frequencies of large reflectivity at 7 km were located over North Houston and south of Houston. At 17 and 18 LST (r and s) enhanced convective frequencies aloft were lower and the largest values were located south of and over downtown Houston at 18 LST (s). By 19 LST (t), only a few areas of high reflectivities were present, over downtown and near the north Galveston Bay shoreline. Over the next two hours (u and v) there were almost no areas of high reflectivity aloft present. At 22 and 23 LST (w and x) a few areas of vigorous convection aloft were found in the northwest corner of the domain, near downtown Houston, and near the Galveston Bay.

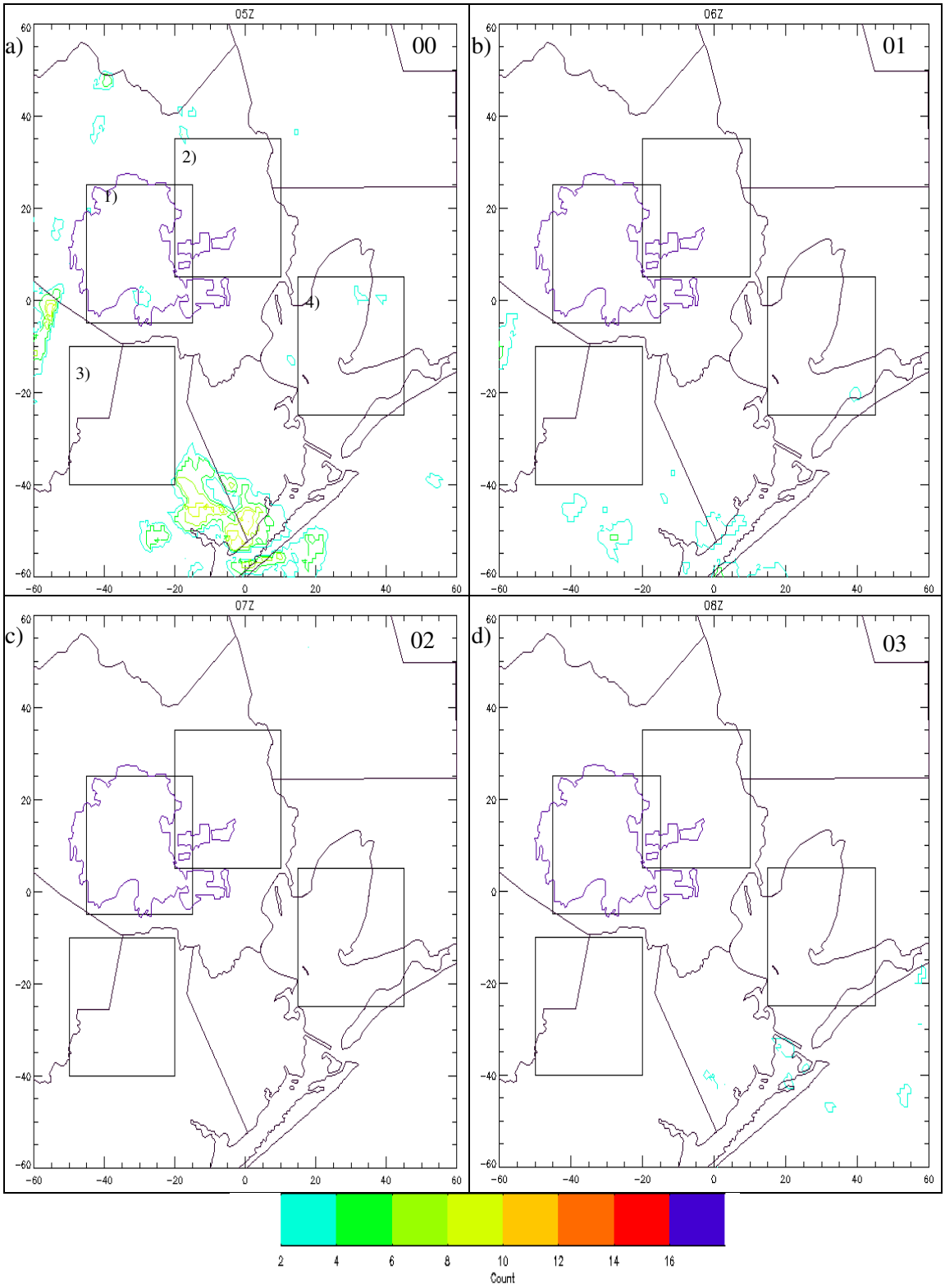

Figure 4.27. Counts of greater than 30 dBZ at 7 km. (a-d) 00 to 03 LST. Boxes are labeled in a. Times in the upper right corners are local.

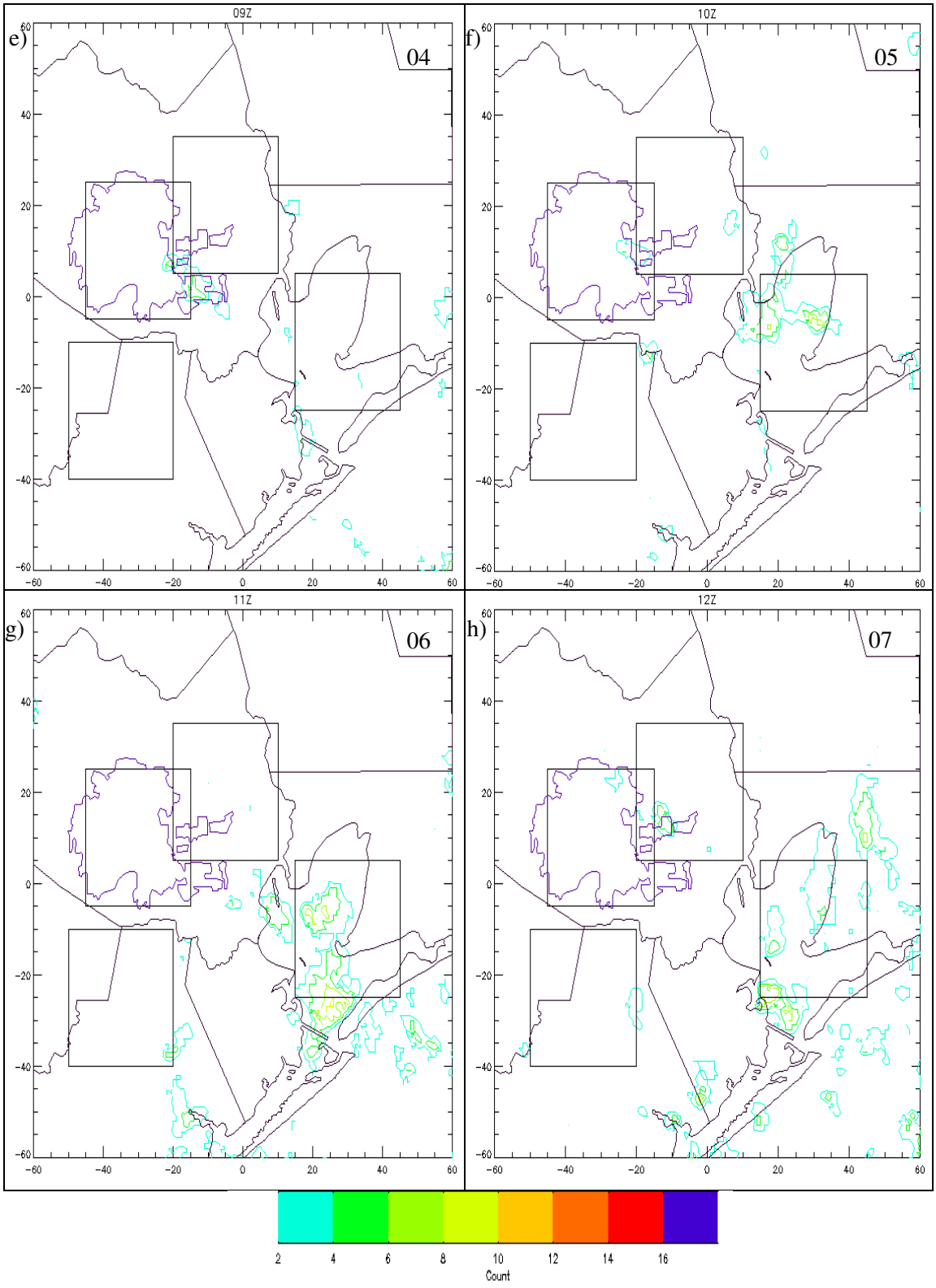

Figure 4.27 cont. (e-h) 04 to 07 LST.

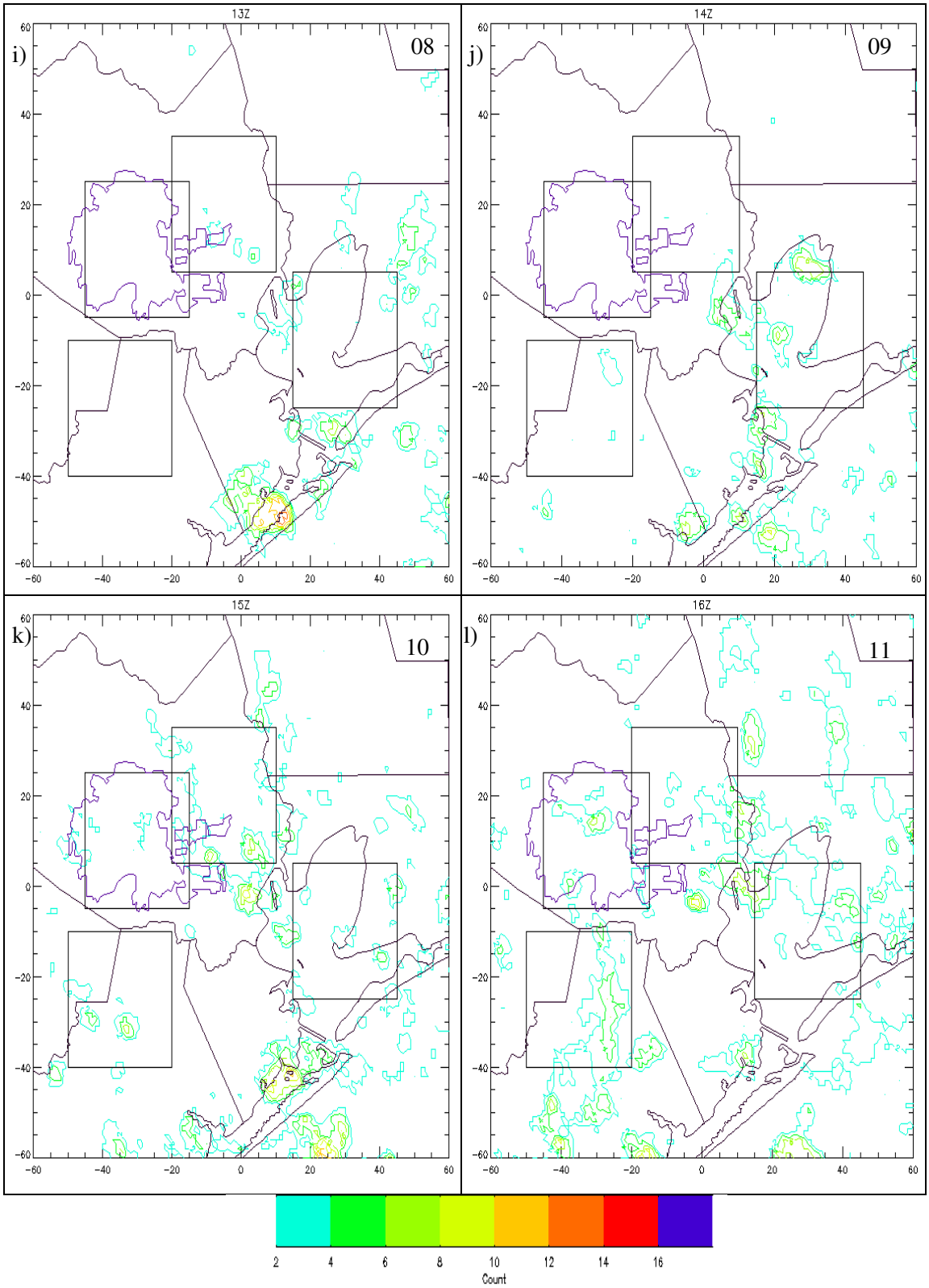

Figure 4.27 cont. (i-l) 08 to 11 LST.

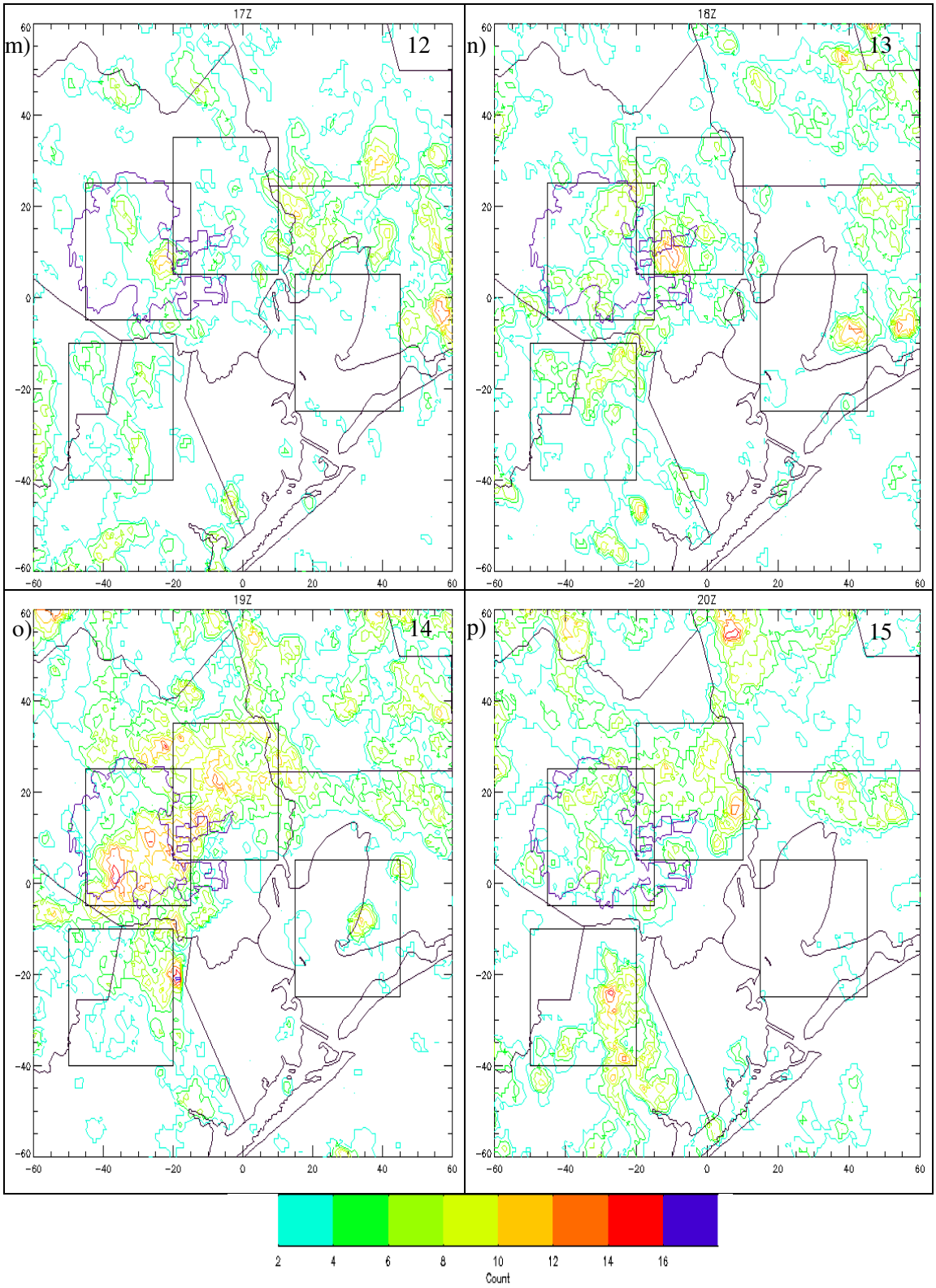

Figure 4.27 cont. (m-p) 12 to 15 LST.

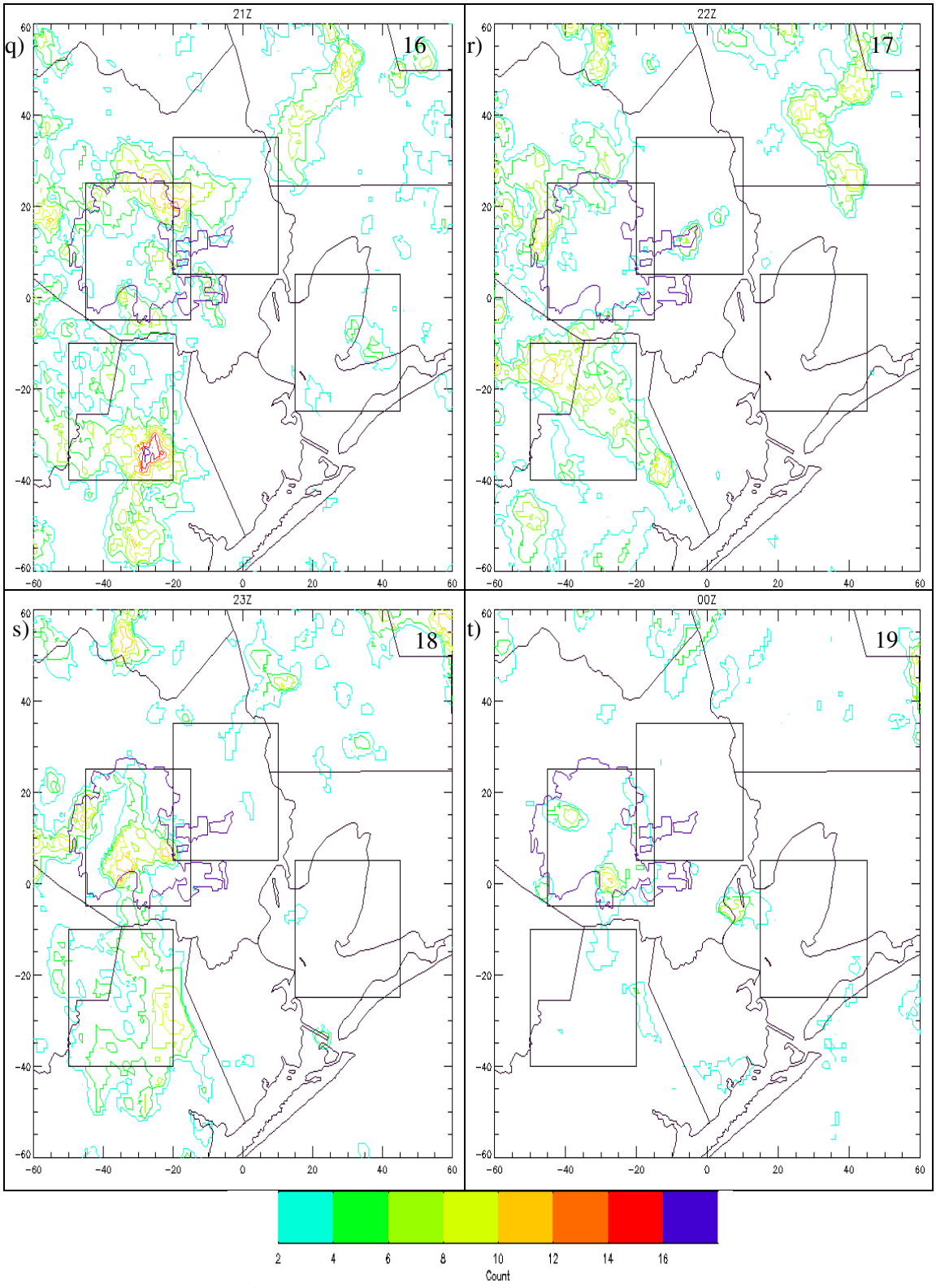

Figure 4.27 cont. (q-t) 16 to 19 LST.

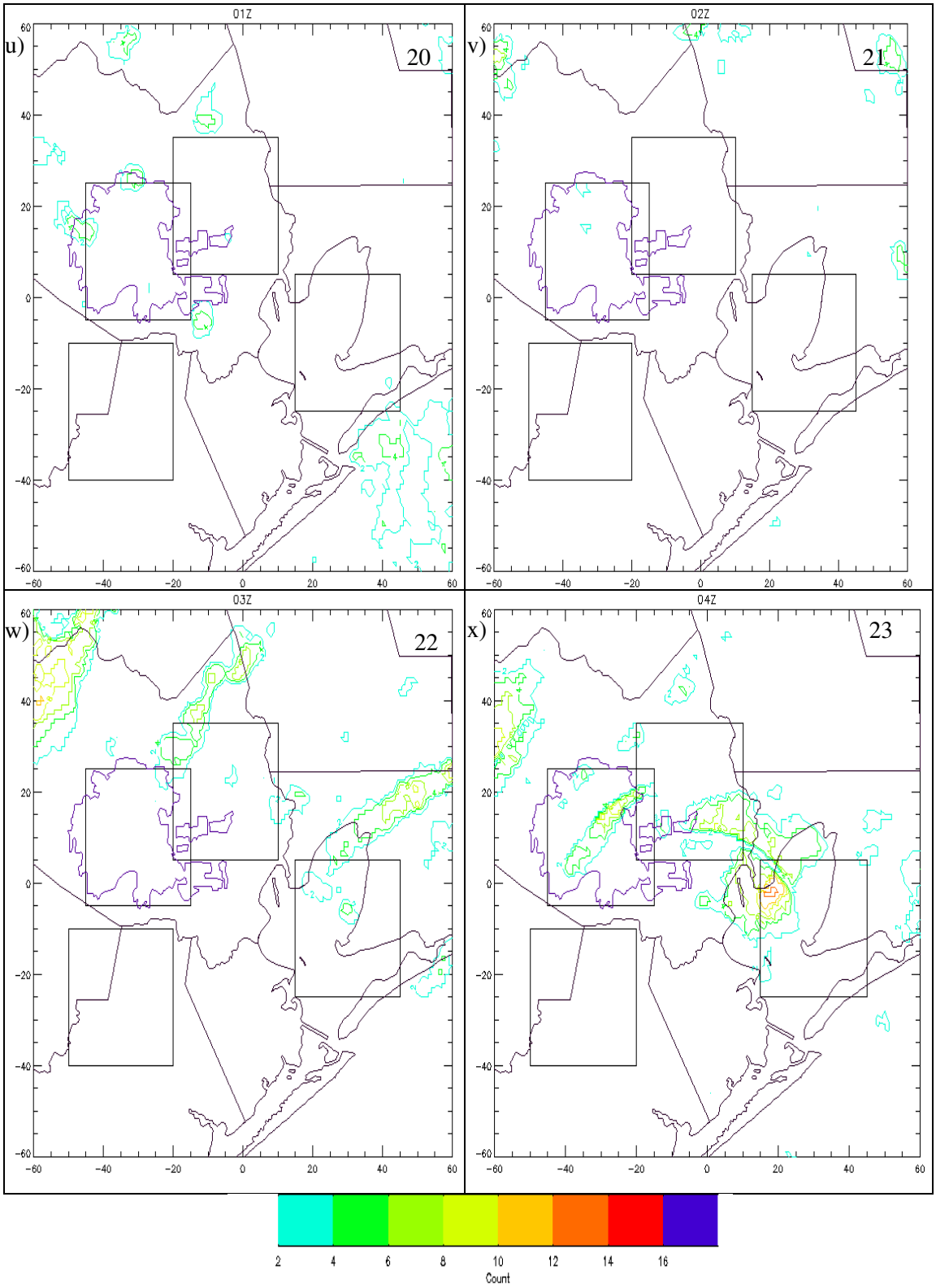

Figure 4.27 cont. (u-x) 20 to 23 LST.

A time series plot for 7 km average reflectivity is presented in Figure 4.28. The domain mean averaged around 10 dBZ near midnight. The domain average hit a minimum in average reflectivity at 4 LST, and began to rise to a maximum of 28 dBZ at 14 LST. Reflectivity values then decreased steadily until 21 LST. The box 1 pattern was very similar to the domain mean. Box 1 values were approximately 5 dBZ higher at midnight and then dropped off to 0 to 5 dBZ during the time span of 4 to 9 LST. The peak of about 32 dBZ in 7 km reflectivity occurred at 14 LST. Reflectivity values did not begin to drop until 19 LST, after which there was a small increase in reflectivity values. Box 2 was very similar to box 1 values, with the nearly the same overall pattern. Box 2 mean reflectivity aloft reached a maximum of 35 dBZ at 14 LST. However, box 2 mean reflectivity values at 7 km decreased rapidly after the peak. Box 3 was also very similar to box 1; however, the peak of 35 dBZ was reached later at 18 LST, after which there was a rapid decrease in reflectivity, reaching 0 dBZ at 22 LST. The box 4 mean reflectivity value aloft was similar to the other boxes near midnight, but average reflectivity rose much earlier in the day. A peak of near 27 dBZ was reached at 7 LST in the morning. Mean reflectivity values at 7 km remained fairly steady until 16 LST, at which point they decreased to 0 dBZ by 21 LST.

Table 4.6 presents the results of the Wilcoxon Rank-Sum test for 7 km mean reflectivity. The mean for box 1 was significantly higher than the domain mean between the hours of 12 and 19 LST, and was significantly lower between 6 and 9 LST. Box 2 was similar, but was only significantly higher between 12 and 16 LST, and was significantly lower between 19 to 21 LST and 7 to 9 LST. Box 3 was significantly

higher from 11 to 14 LST and 16 to 20 LST, and was significantly lower from 4 to 10 LST. Box 4 was significantly higher from 5 to 11 LST and was significantly lower from 12 to 21 LST.

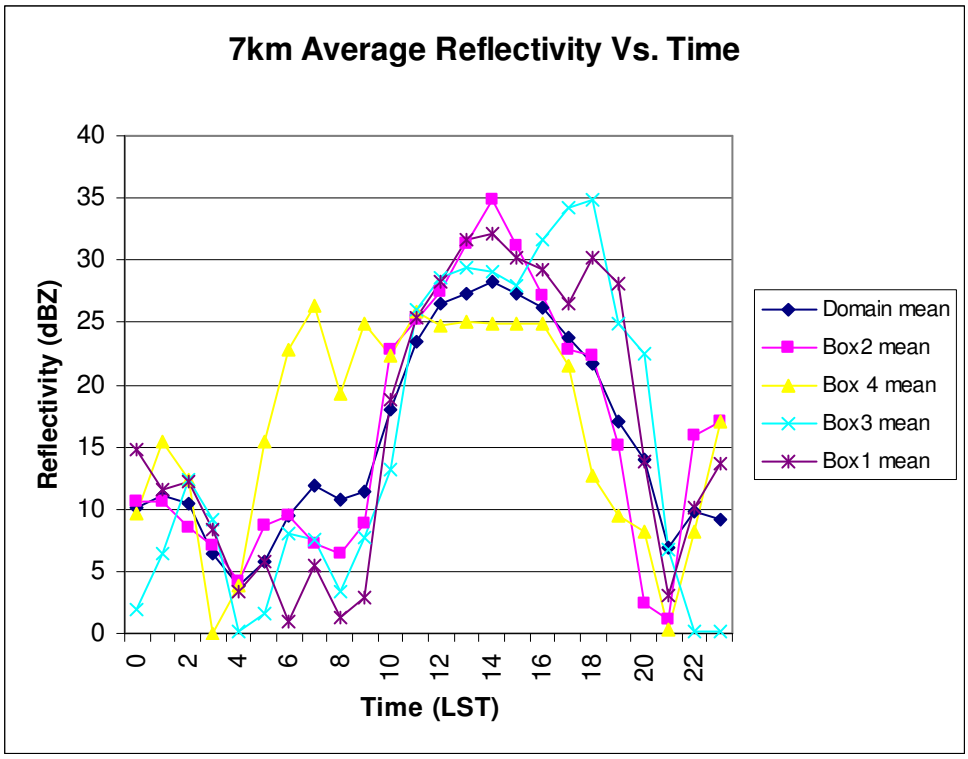

Figure 4.28. Time series of domain and box averaged reflectivity (dBZ) at 7 km.

Table 4.6. Hourly Wilcoxon Rank-Sum at the 5% significance level results for box average reflectivity at 7 km. N indicates not significantly different, H is significantly higher, and L is significantly lower than the domain mean.

Hour (LST)	0	1	2	3	4	5	6	7	8	9	10	11	12	13	14	15	16	17	18	19	20	21	22	23
Box 1	H	N	H	H	N	N	L	L	L	L	H	N	H	H	H	H	H	H	H	H	L	L	N	H
Box 2	N	L	L	N	N	H	N	L	L	L	H	N	H	H	H	H	H	L	N	L	L	L	H	H
Box 3	L	L	H	H	L	L	L	L	L	L	L	H	H	H	H	N	H	H	H	H	H	N	L	L
Box 4	N	H	H	L	N	H	H	H	H	H	H	H	L	L	L	L	L	L	L	L	L	L	H	N

A diurnal time-series of convective frequency for reflectivity values above 30 dBZ is presented in Figure 4.29. The plot shows that the count was near zero for all boxes and the domain between midnight and 4 LST. The domain count remained near zero until 9 LST and then slowly increased to a peak of near 2.5 at 14 LST, and slowly began to decrease after that time. Box 1 also did not increase until after 9 LST, but increased rapidly and reached a peak of near 6.5 at 14 LST. Box 1 then decreased, but has another small peak at 19 LST, after which the frequency decreased to near zero at 21 LST. Box 2 was almost identical to box 1, but did not achieve a second peak and dropped to near zero by 17 LST. Box 3 increased slowly after 9 LST and reached a peak of near 4 at 16 LST. Counts for box 3 stayed fairly steady until after 18 LST, when counts dropped to near zero. Box 4 counts began to rise after 4 LST, and remained fairly steady between 0.5 and 1 until 17 LST.

Table 4.7 presents the results of the Wilcoxon Rank-Sum test for convective frequency for reflectivities above 30 dBZ. The box 1 mean was significantly higher than the domain mean between 12 and 19 LST and was significantly lower between 6 and 9 LST. Box 2 was significantly higher between 13 and 16 LST, significantly lower between 6 and 9 LST, and was not significantly different from the domain mean between 2 and 5 LST. Box 3 was significantly higher between 11 and 14 LST and 16 and 19 LST, and was significantly lower between 20 overnight to 2 LST and 4 and 10 LST. Box 4 was significantly higher between 5 and 7 LST, was significantly lower between 12 and 21 LST, and was not significantly different between 1 and 4 LST.

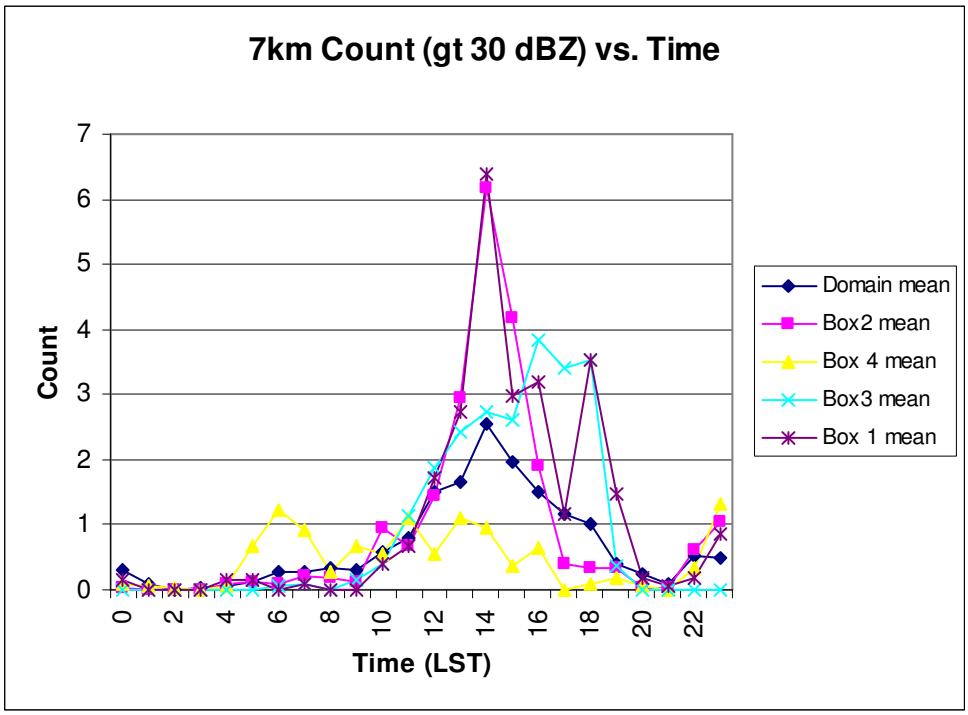

Figure 4.29. Time-series of domain and box average convective frequency for reflectivities above 30 dBZ at 7km.

Table 4.7. Hourly Wilcoxon Rank-Sum at the 5% significance level results for box average convective frequency above 30 dBZ at 7 km. N indicates not significantly different, H is significantly higher, and L is significantly lower than the domain mean.

Hour (LST)	0	1	2	3	4	5	6	7	8	9	10	11	12	13	14	15	16	17	18	19	20	21	22	23
Box 1	N	L	N	N	H	N	L	L	L	L	N	N	H	H	H	H	H	H	H	H	L	N	L	H
Box 2	L	L	N	N	N	N	L	L	L	L	H	N	N	H	H	H	H	L	L	N	L	L	H	H
Box 3	L	L	N	N	L	L	L	L	L	L	L	H	H	H	H	N	H	H	H	H	L	L	L	L
Box 4	L	N	N	N	N	H	H	H	N	H	N	H	L	L	L	L	L	L	L	L	L	L	N	H

Figure 4.30 presents the total average reflectivity at 7 km. Highest reflectivity values were located downtown and northwest of Houston, on the west edge of the cone of silence, along the north coast of Galveston Bay, and in the northeast and northwest portions of the domain. The lowest reflectivities were located in the southern portion of Galveston Bay and in the southern portion of the domain, mainly off of the coast over the Gulf of Mexico. The results of the Wilcoxon Rank-Sum test reveal that the mean of boxes 1, 2, and 3 were significantly higher than the domain mean while the mean of box 4 was significantly lower than the domain mean.

Figure 4.31 presents a total count of the occurrence of reflectivity above 30 dBZ at 7 km. The highest counts occurred over downtown, northwest, and northeast of Houston. West of the radar cone of silence there was another large area of high frequency. Moderate and high counts were located in the northeast and northwest portions of the domain. The lowest frequencies occurred over the southern portion of Galveston Bay,

over the Gulf of Mexico, and north of the east half of Galveston Bay. The results of the Wilcoxon Rank-Sum test show that the means of boxes 1, 2, and 3 were significantly higher than the domain mean while the mean of box 4 was significantly lower.

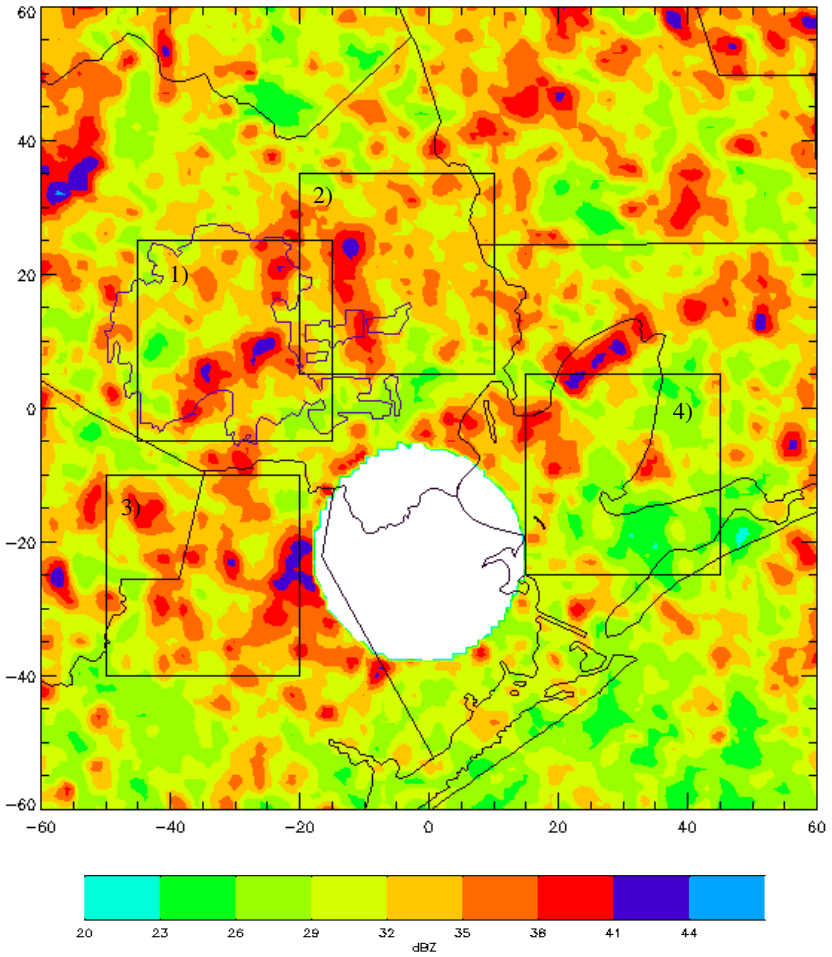

Figure 4.30. Total average reflectivity (dBZ) at 7km. Blank area is radar cone of silence.

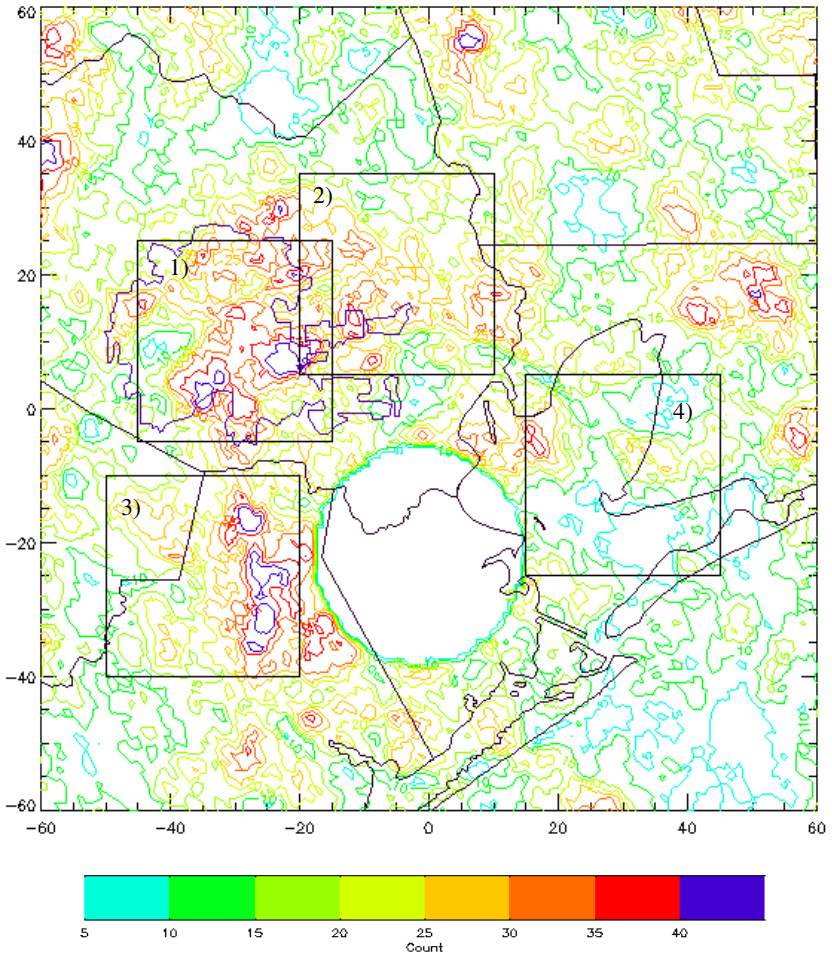

Figure 4.31. Average count of frequency of convection for reflectivities above 30 dBZ at 7 km.

4.2.5 *Average Cumulative Rainfall*

Figure 4.32 presents the diurnal variation of average cumulative rainfall. At midnight (a) the heaviest rainfall was located west of Houston and south of Houston near the coast. At 1 LST (b) the only significant rain was located in the southwest corner of the domain. During the next couple of hours (c and d) there were no significant areas of

rainfall. Beginning at 4 LST (e) small areas of moderate rainfall amounts were located near Houston and near the Galveston Island coast. Over the next couple of hours (f and g) most rainfall was located northwest of the Galveston Bay and over the northern portion of the Bay. At 7 LST (h) the heaviest rainfall was located northeast of Galveston Bay. At 8 LST (i) the heaviest rainfall was located inland of the coast south of Houston. At 9 LST (j) areas of moderate rainfall were located over the northern part of Galveston bay and south of Houston. At 10 LST (k) there were areas of light rainfall located in many locations all over the domain. A similar pattern was present over the next several hours from late morning to mid-afternoon (l-p), with the highest amounts of rainfall located in the northern part of the domain. At 16 LST (q) moderate areas of rainfall were located north of downtown Houston and north of Galveston Bay. At 17 LST (r) areas of rainfall were located in northwest Houston, east of Houston, and south of Houston. During the next hour (s) large amounts of rainfall were located south of Houston and lighter amounts were located in downtown Houston. At 19 LST (t) heavy amounts of rainfall were located over east Houston and south of the Houston area. At 20 LST (u) the heaviest amounts of rainfall occurred off of the Texas coast south of the Galveston Bay. At 21 LST (v) there was only a small area of rainfall located west of Galveston Bay. At 22 LST (w) high rain totals were located northwest of Houston and northeast of Galveston Bay. By 23 LST (x) high rain amounts were located in the downtown area and northwest of Galveston Bay.

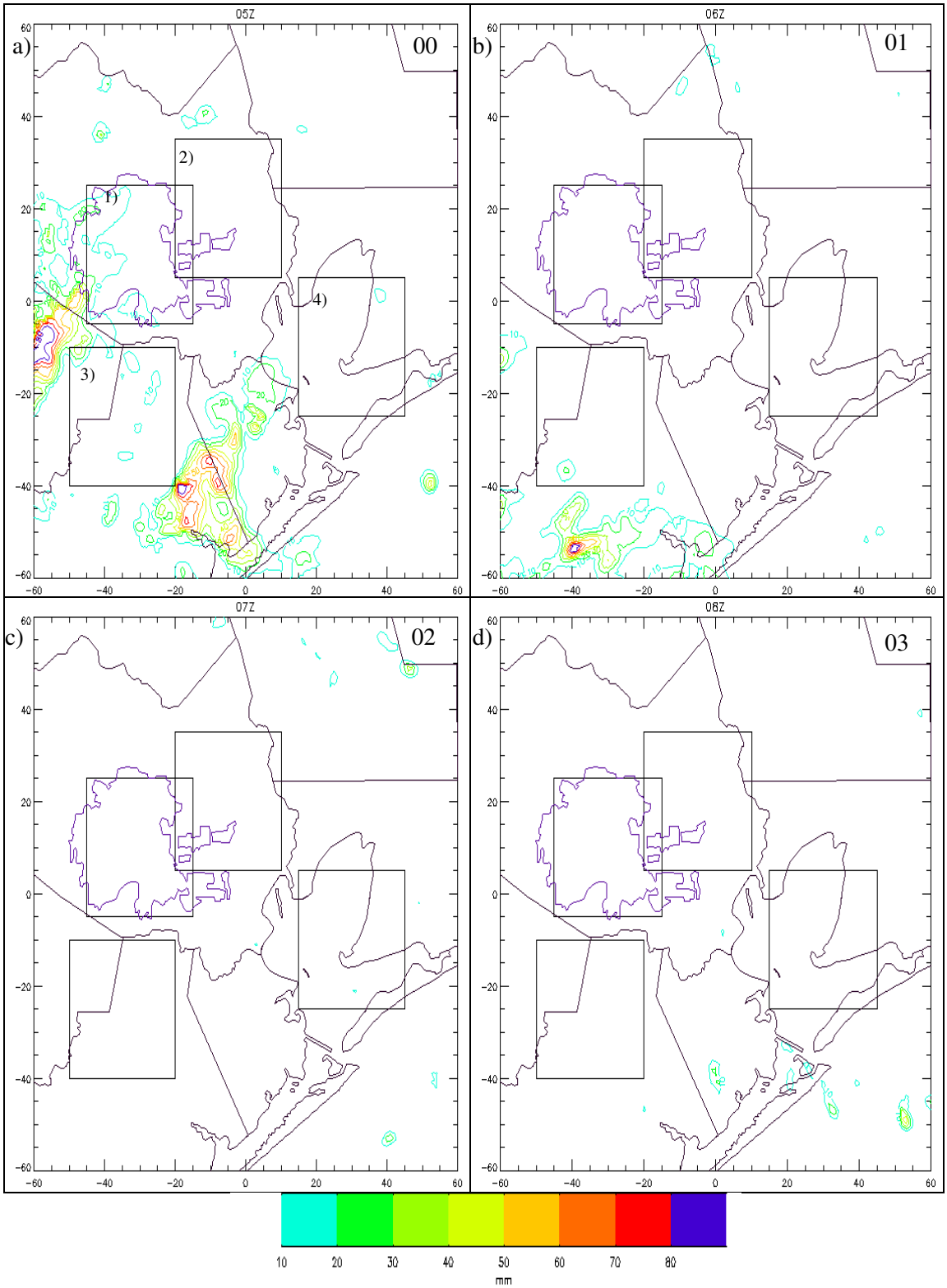

Figure 4.32. Average cumulative rainfall (mm). (a-d) 00 to 03 LST. Boxes are labeled in a. Times in the upper right corners are local.

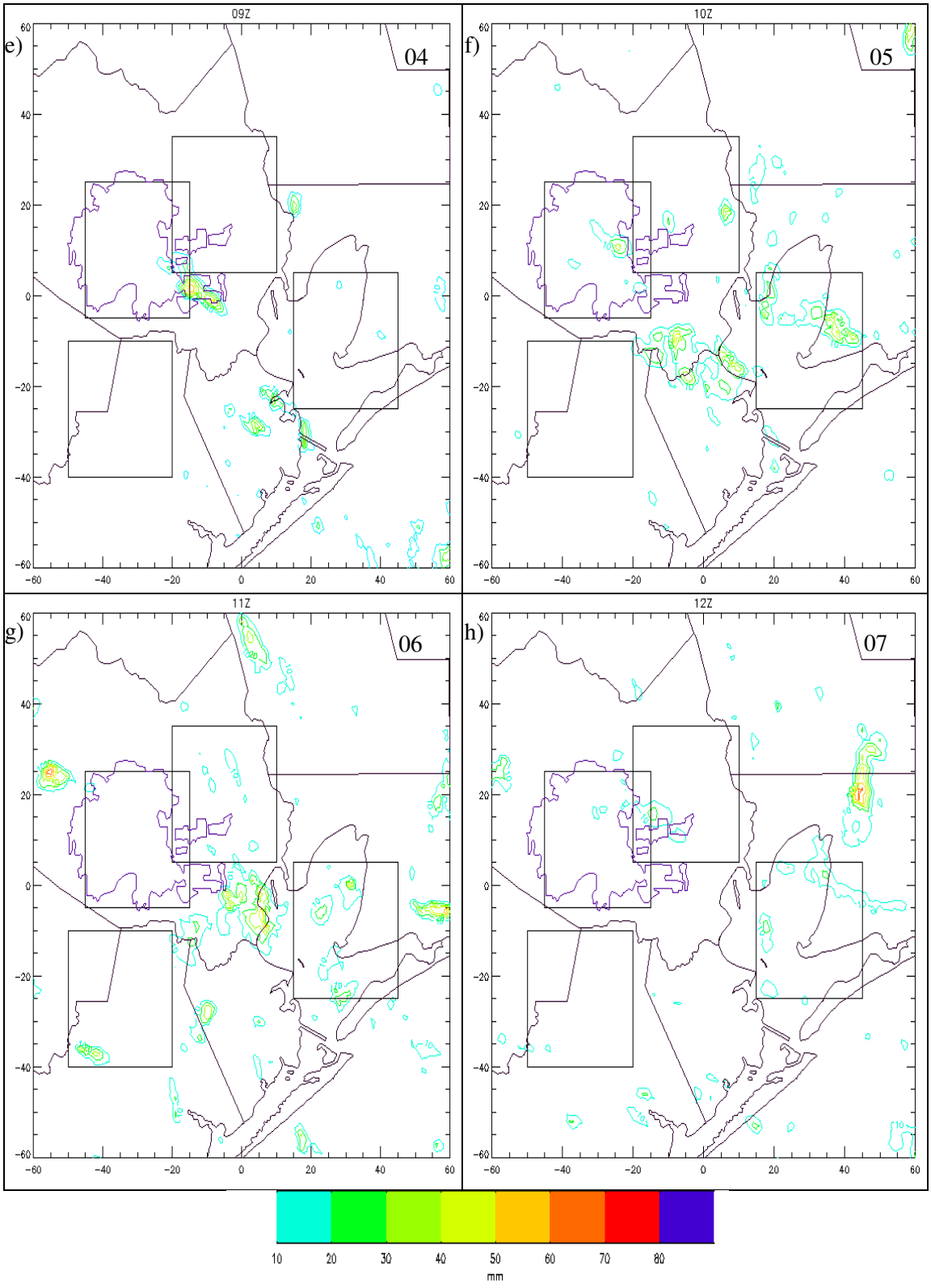

Figure 4.32 cont. (e-h) 04 to 07 LST.

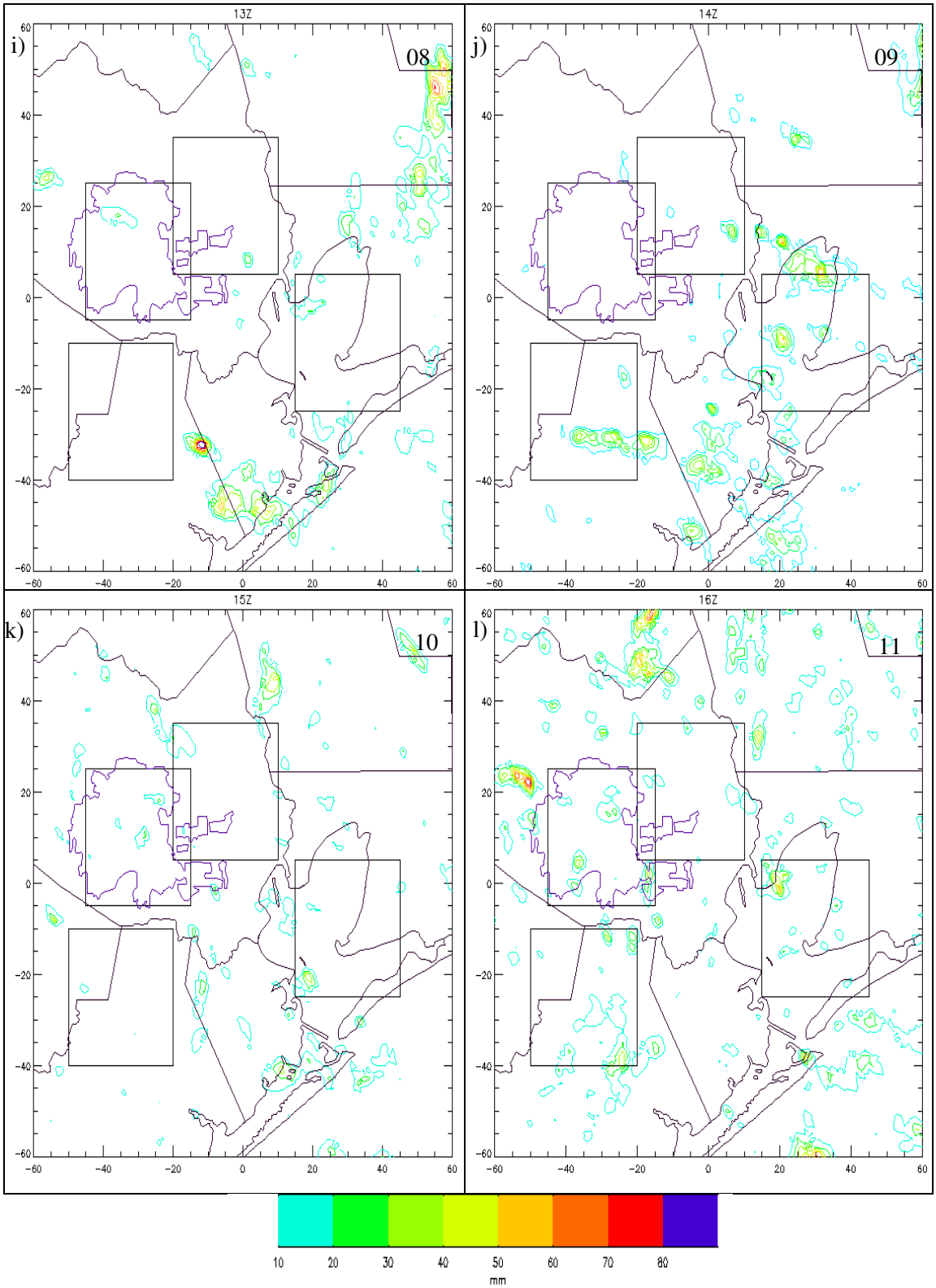

Figure 4.32 cont. (i-l) 08 to 11 LST.

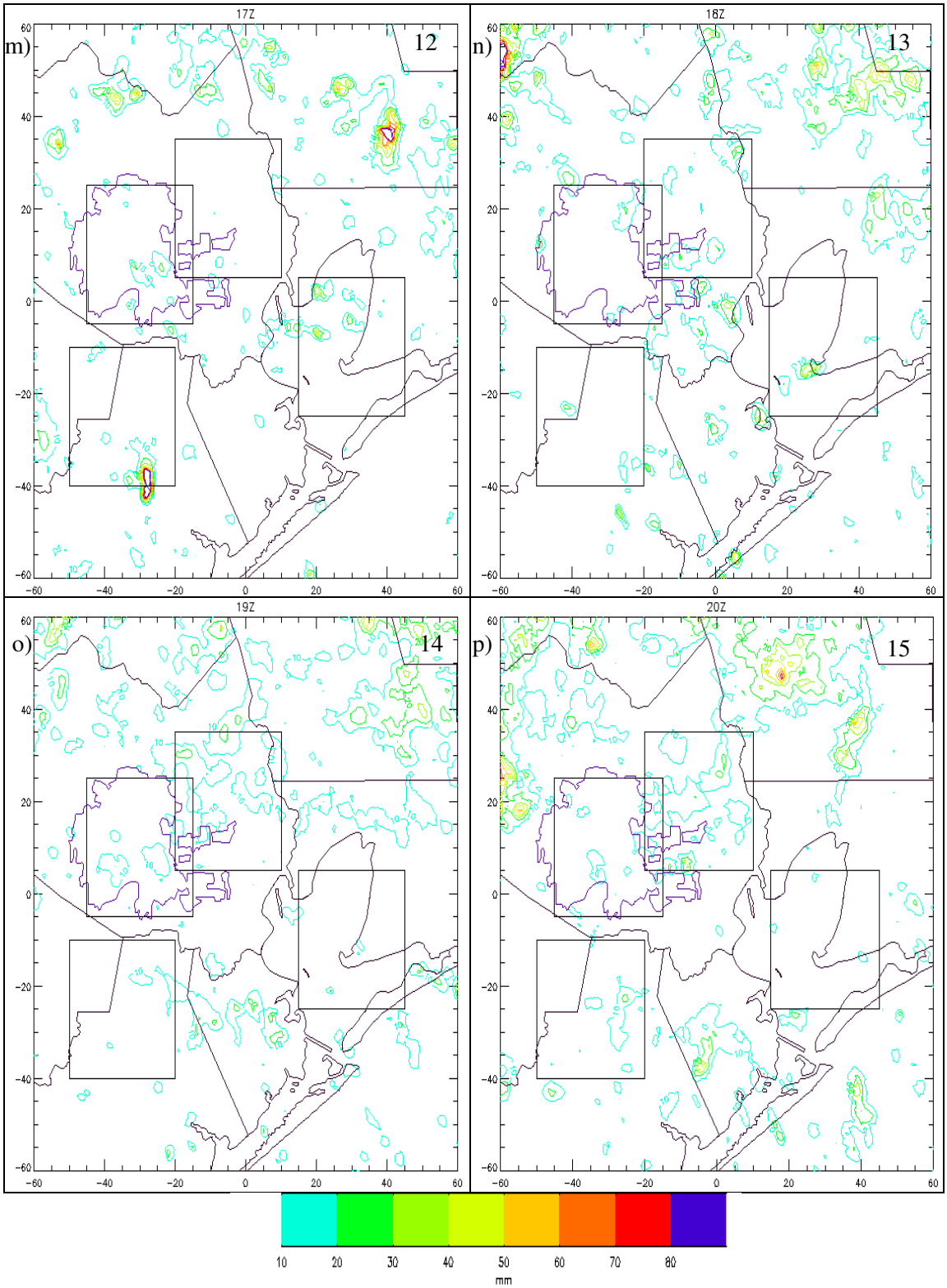

Figure 4.32 cont. (m-p) 12 to 15 LST.

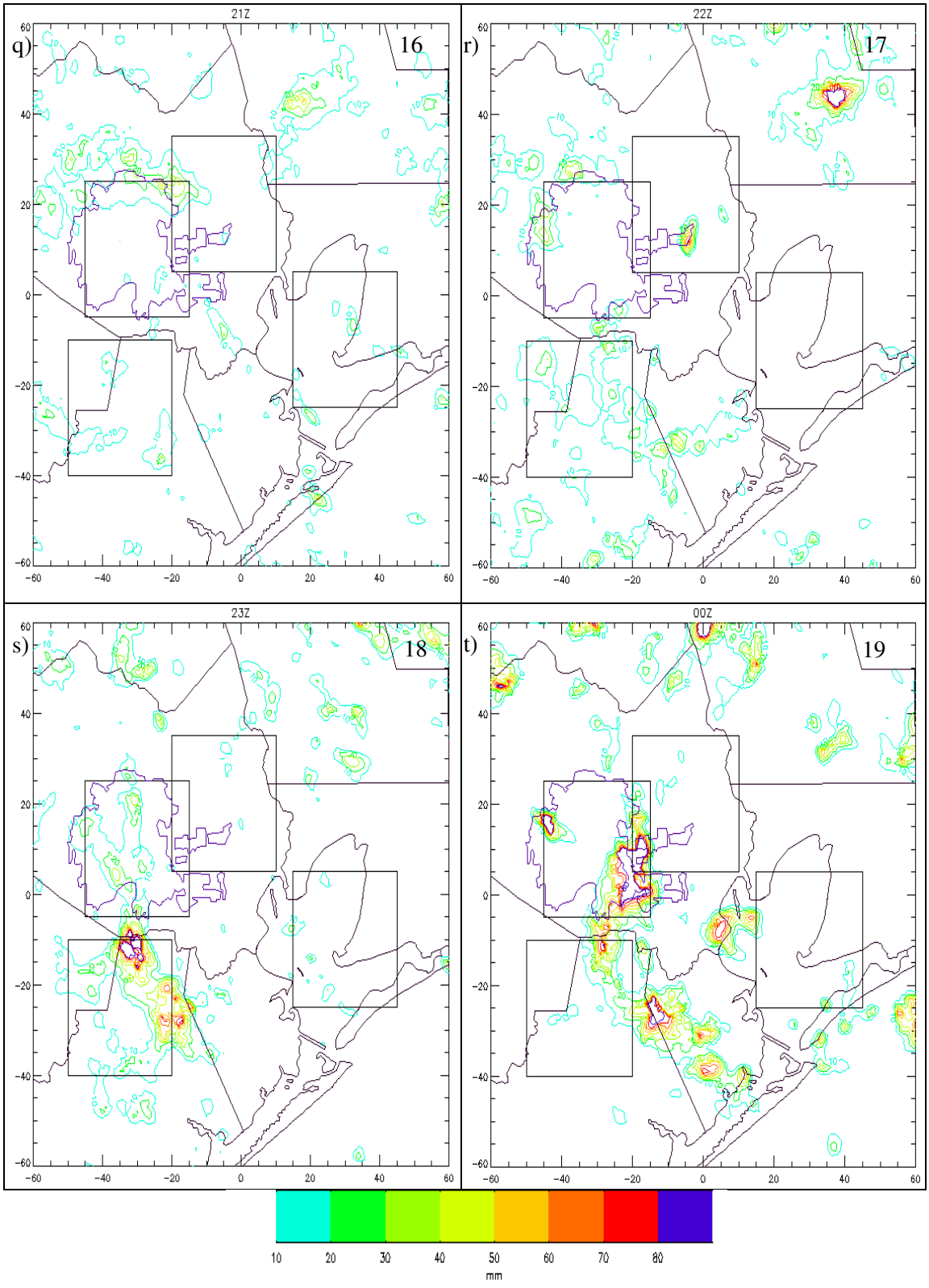

Figure 4.32 cont. (q-t) 16 to 19 LST.

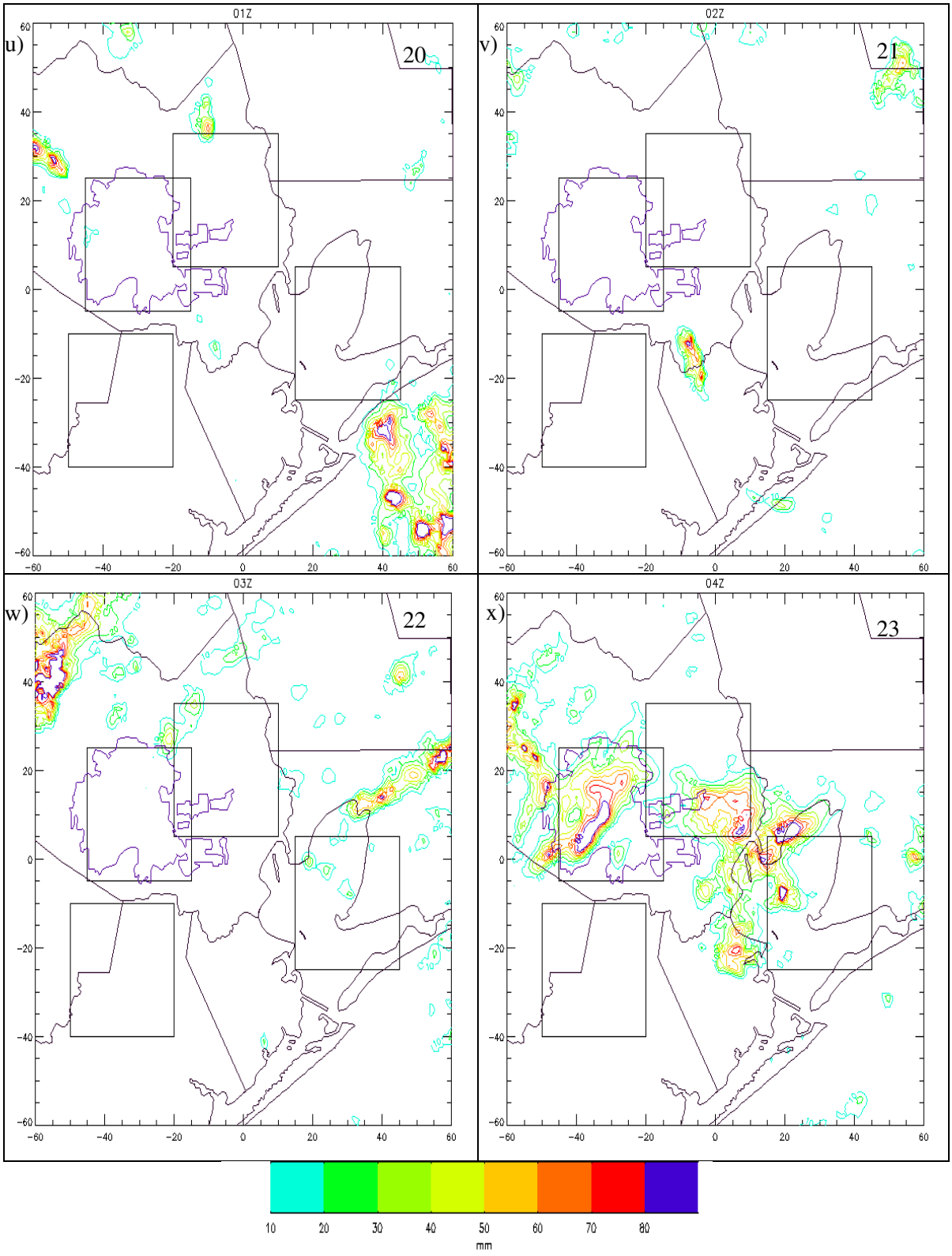

Figure 4.32 cont. (u-x) 20 to 23 LST.

Figure 4.33 presents a time series of average cumulative rainfall for each box and the domain. The domain average slowly rose after 4 LST, after a minimum of near 1 mm. The domain average reached a steady average of near 5 mm by 11 LST and did not drop until 20 LST. A peak of 7 mm was reached again at 23 LST. The box 1 pattern was similar, but was characterized by larger values at 16, 18, and 19 LST, at which time a peak of 20 mm average rainfall was reached. A second peak of 24 mm occured at 23 LST after dropping to near 0 between 20 and 22 LST. The average in box 2 was higher at 14 and 15 LST than box 1. A first peak of 8 mm occurred at 15 LST, and a second peak of 16 mm occurred at 23 LST. The pattern in box 3 was also similar to box 1 and box 2. Box 3 reached a peak value of 17 mm at 18 LST. Box 4 values rose from near zero to about 5 mm at 5 LST. The average value remained near 3 mm and decreased to near zero by 21 LST.

Table 4.8 presents the results of the Wilcoxon Rank-Sum tests for average cumulative rainfall in each box. The box 1 mean was significantly higher than the domain mean from 14 to 19 LST and 23 LST to 3 LST and was significantly lower from 6 to 9 LST. Box 2 was significantly higher from 13 to 15 LST and 22 to 3 LST, and was significantly lower from 7 to 12 and 17 to 21 LST. Box 3 was significantly higher from 16 to 19 LST and significantly lower from 4 to 10 and 13 to 15 LST. Box 4 was significantly higher from 4 to 9 LST and significantly lower for all but one hour from 10 to 3 LST.

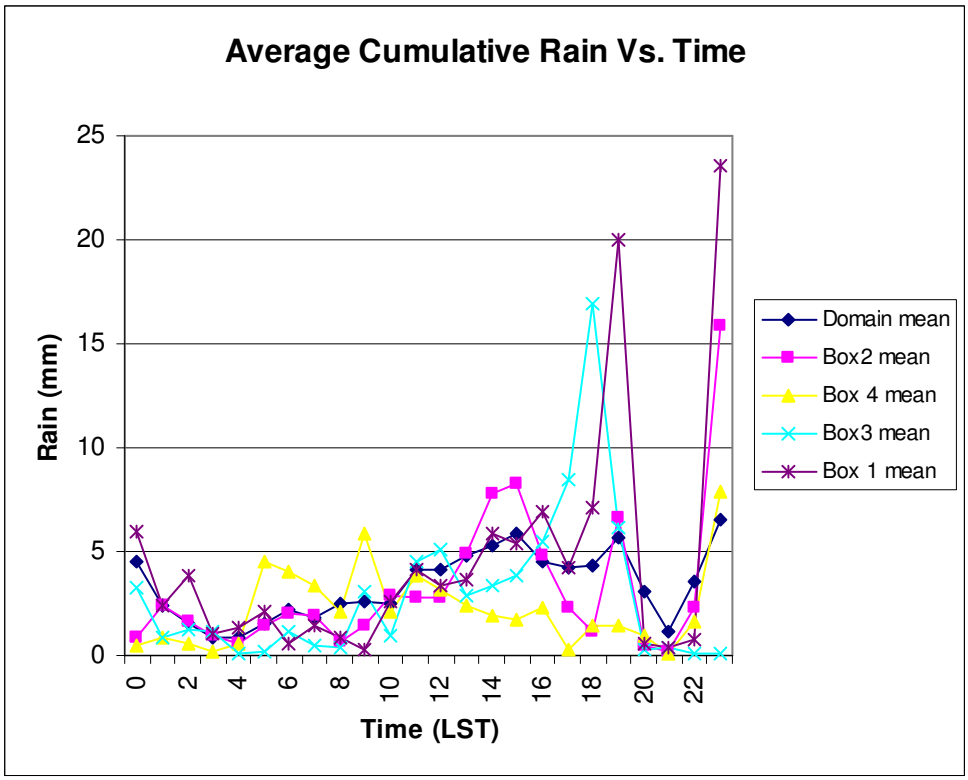

Figure 4.33. Time series of domain and box average cumulative rainfall (mm).

Table 4.8. Hourly Wilcoxon Rank-Sum results at the 5% significance level for box average cumulative rainfall. N indicates not significantly different, H is significantly higher, and L is significantly lower than the domain mean.

Hour (LST)	0	1	2	3	4	5	6	7	8	9	10	11	12	13	14	15	16	17	18	19	20	21	22	23
Box 1	H	H	H	H	L	H	L	L	L	L	H	H	L	N	H	H	H	H	H	H	N	N	L	H
Box 2	N	H	H	H	L	N	H	L	L	L	L	L	L	H	H	H	N	L	L	L	L	L	H	H
Box 3	H	L	H	H	L	L	L	L	L	L	L	N	H	L	L	L	H	H	H	H	L	H	L	L
Box 4	L	L	L	L	H	H	H	H	H	H	L	L	L	L	L	L	L	L	L	L	L	L	L	N

Figure 4.34 presents the total average cumulative rainfall. The total average cumulative rainfall shows the highest values were in the northwest and northeast corners of the domain. Maximums of 14 mm occurred over downtown Houston. Increased values were also present northeast and northwest of Houston. The portion of the domain directly south of Houston also show local maximum values. Low average cumulative rainfall was located over the southern portion of Galveston Bay. The northern portion of the Bay showed an increase in the amount of rainfall, especially along the northern coast. The results of the Wilcoxon Rank-Sum test shows that the means of boxes 1, 2, and 3 were significantly higher than the domain mean while the mean of box 4 was significantly lower.

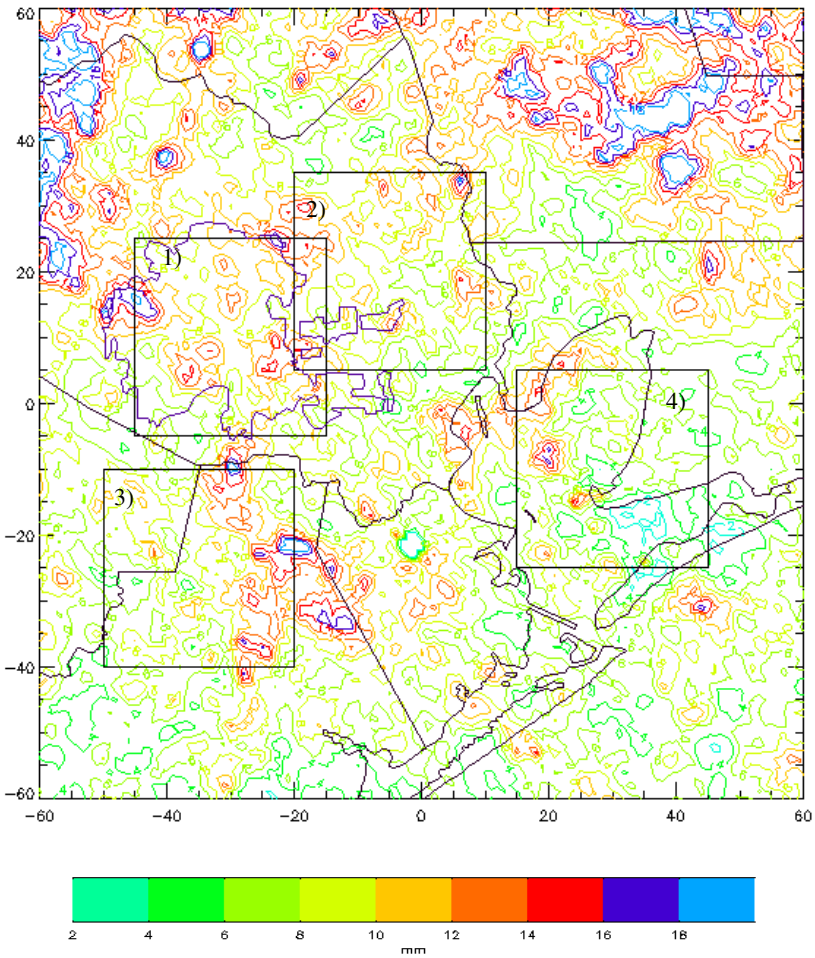

Figure 4.34. Total average cumulative rainfall (mm). Blank circle at X = -1 km and Y = -21 km is the radar cone of silence.

4.2.6 *Average Cloud-to-Ground Lightning*

Figure 4.35 presents the diurnal variation of mean CG lightning density. At midnight (a) the only CG lightning that was present was located along the coast line south of Houston. Between the hours of 1 and 4 LST (b-e) no CG lightning was present in the domain. Between 5 and 7 LST (f-h) isolated areas of CG lightning were located over Galveston Bay. Between 8 and 10 LST (i-k) CG lightning was located near or off

the coast south of Houston. At 11 LST (l) the largest area of average CG lightning was located over the northern Galveston Bay. By 12 LST (m) the presence of CG lightning had increased spatially, with the highest values located to the east of Galveston Bay. At 13 LST (n) the mean CG lightning density maximum was located over and east of Houston. At 14 LST (o) the majority of CG lightning was located over downtown Houston and northeast of Houston. Lightning was also located to the west and northeast of Galveston Bay. By 15 LST (p) there were numerous areas of CG lightning throughout the domain. At 16 LST (q) there were two large areas of maximum CG flash density, over northeast Houston and in the southwest corner of the domain. During the next hour (r) only the lightning in the southwest corner of the domain was present. At 18 LST (s) a large area of average lightning was located south of Houston, and there was also lightning located over downtown Houston. During the next three hours (t-v) the average CG flash density decreased from the previous hours, with lightning almost completely absent from the domain at 21 LST. At 22 LST (w) the largest area of CG lightning was located in the northwest corner of the domain. At 23 LST (x) large amounts of ground flashes were located to the northwest of Houston and over north Galveston Bay.

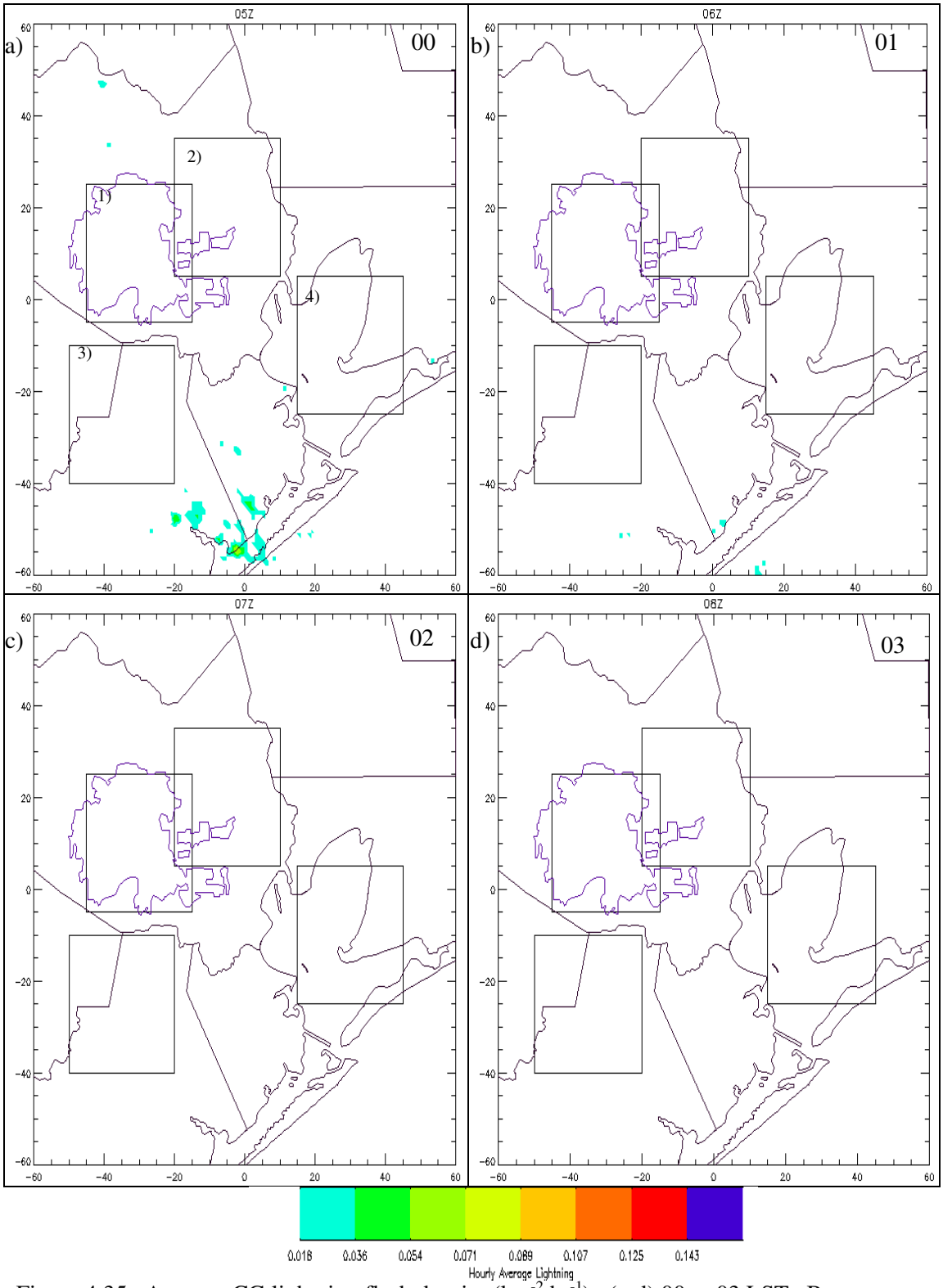

Figure 4.35. Average CG lightning flash density (km^{-2} hr^{-1}). (a-d) 00 to 03 LST. Boxes are labeled in a. Times in the upper right corners are local.

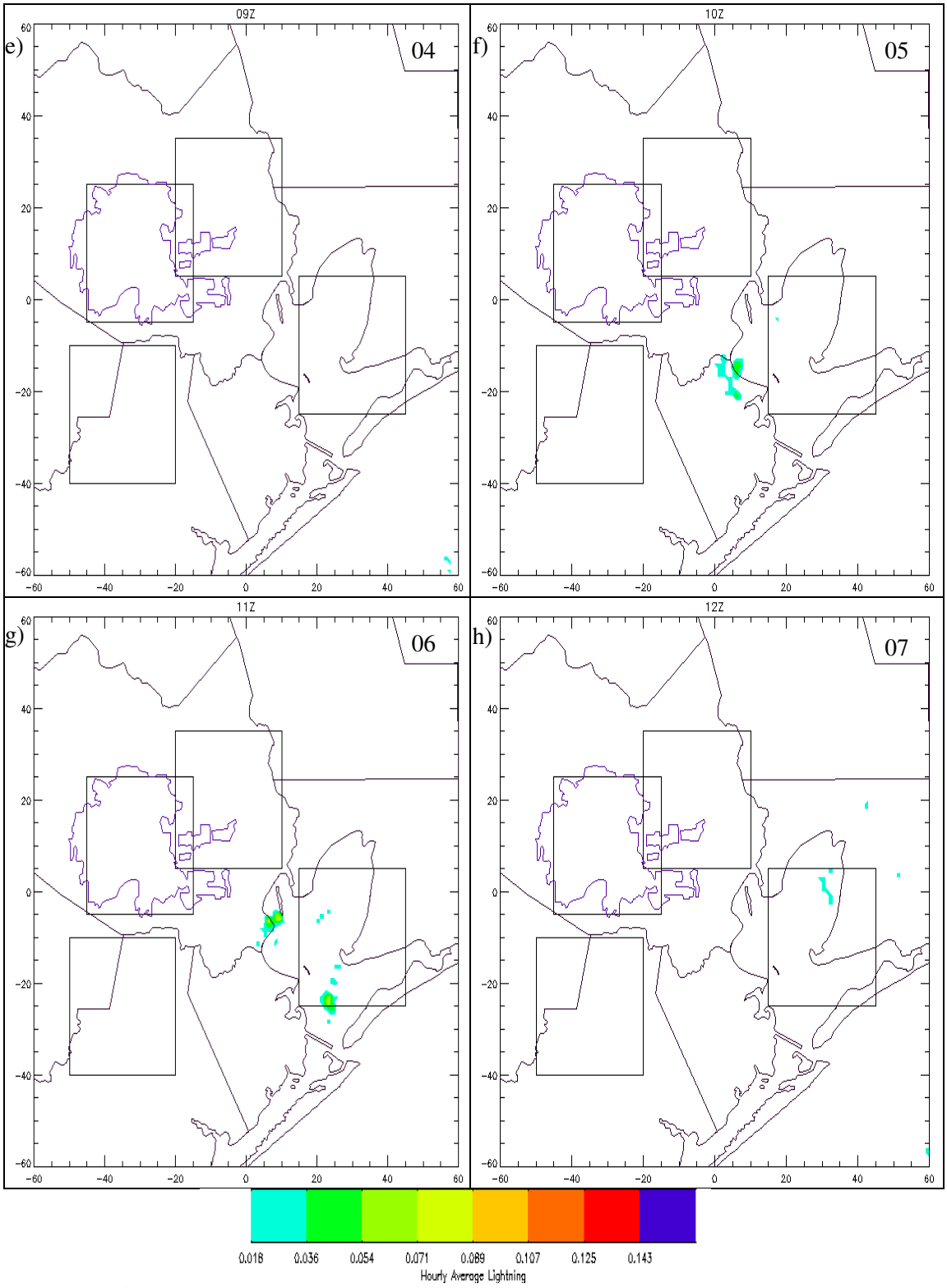

Figure 4.35 cont. (e-h) 04 to 07 LST.

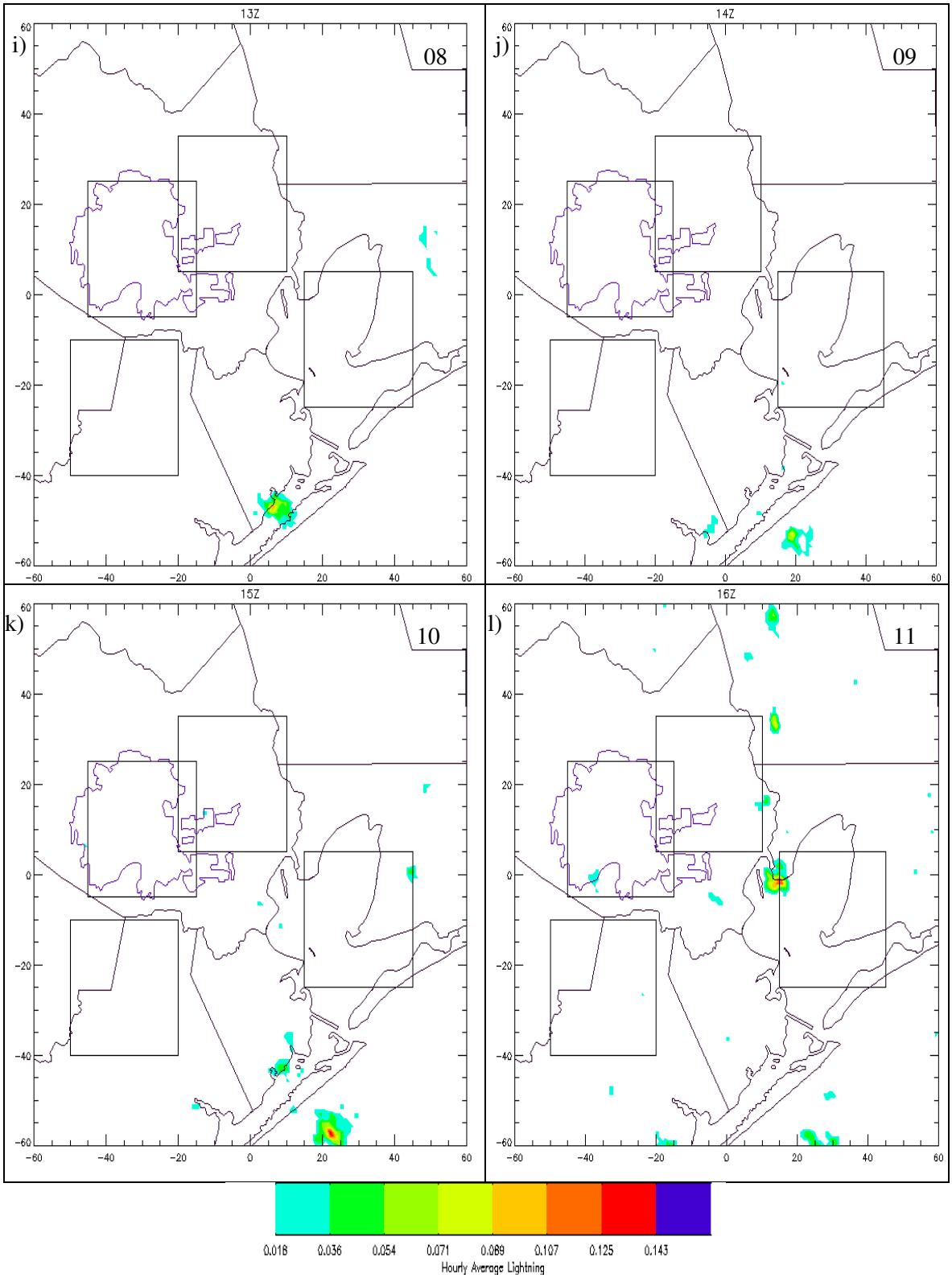

Figure 4.35 cont. (i-l) 08 to 11 LST.

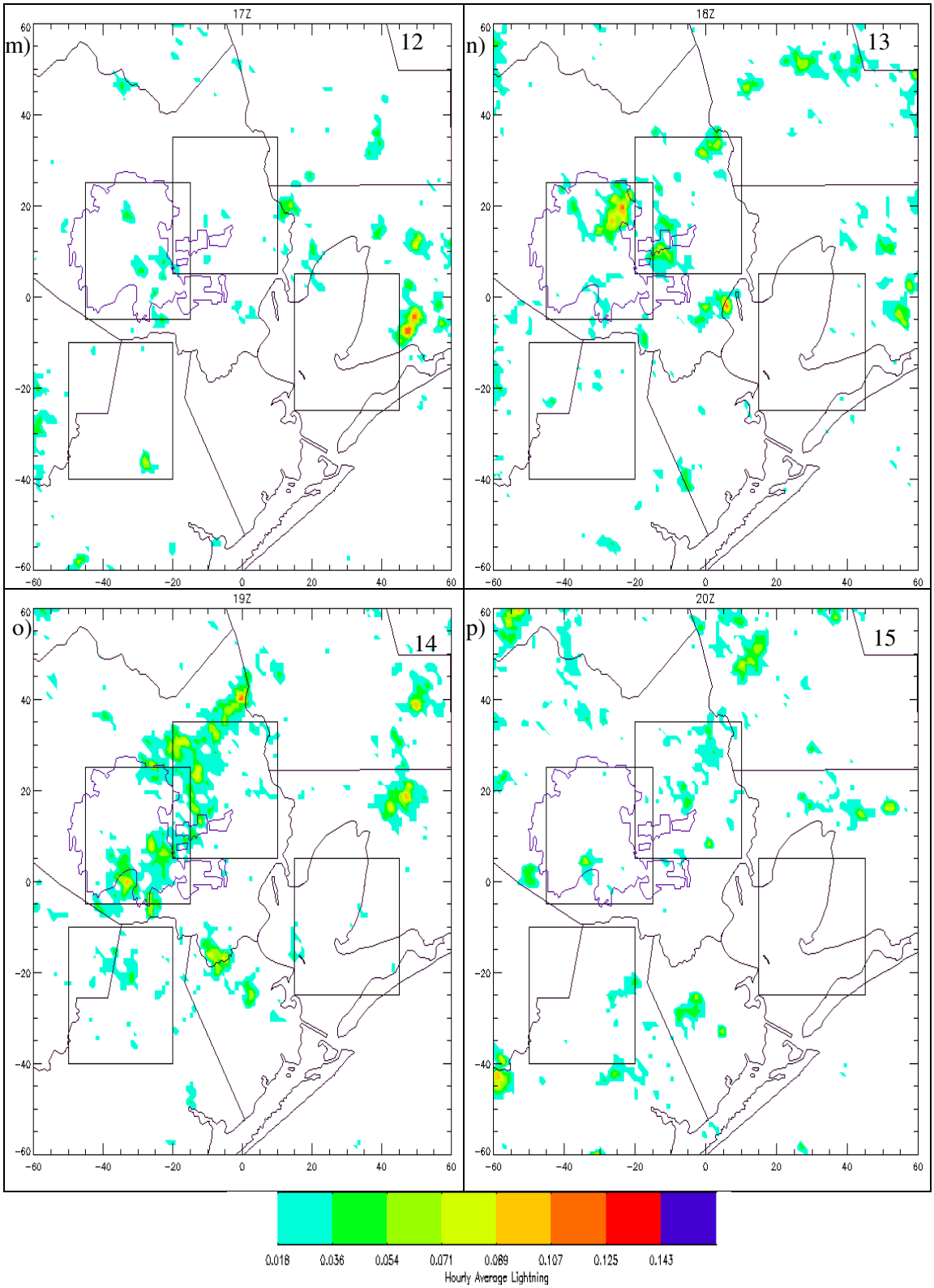

Figure 4.35 cont. (m-p) 12 to 15 LST.

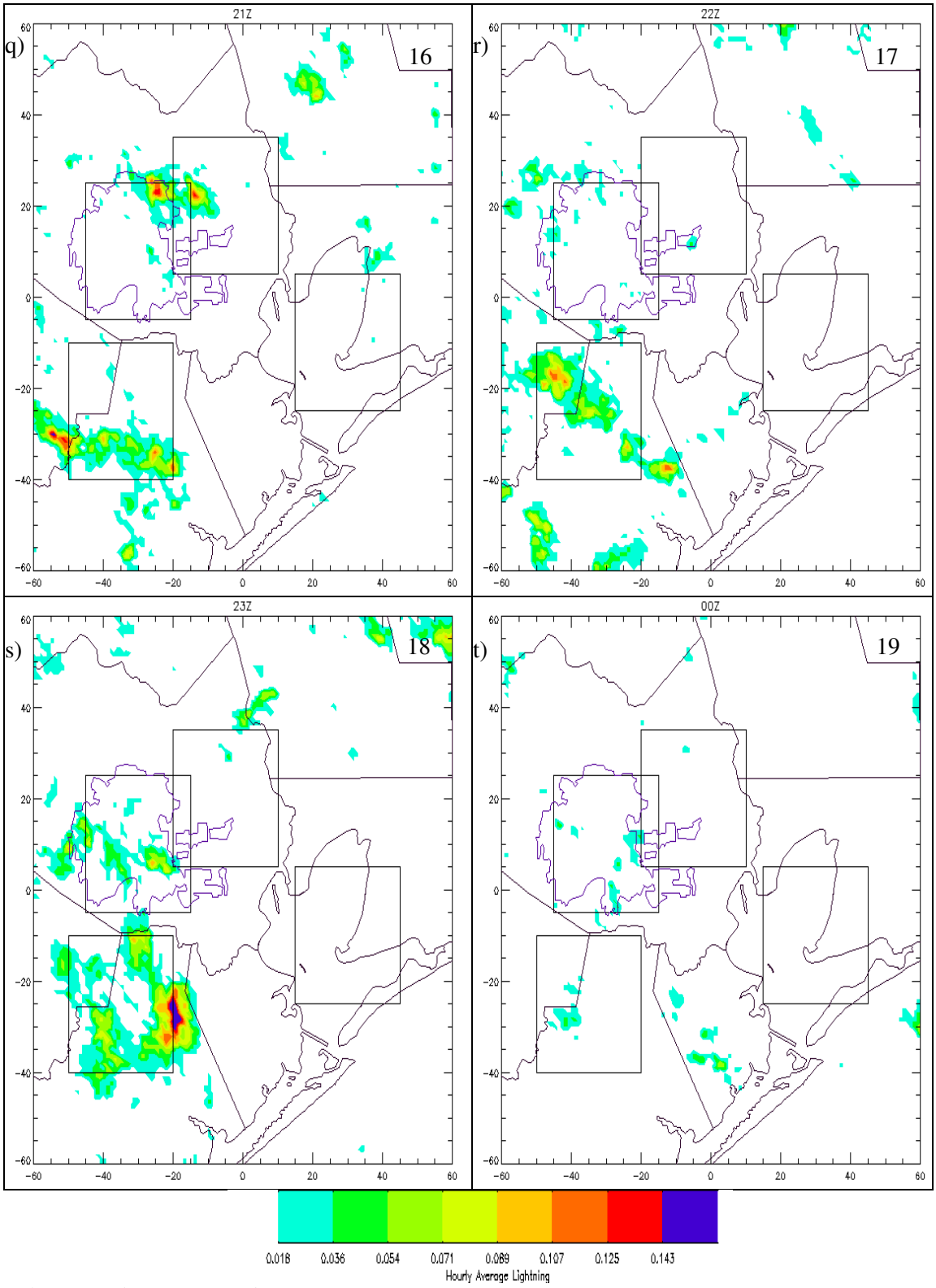

Figure 4.35 cont. (q-t) 16 to 19 LST.

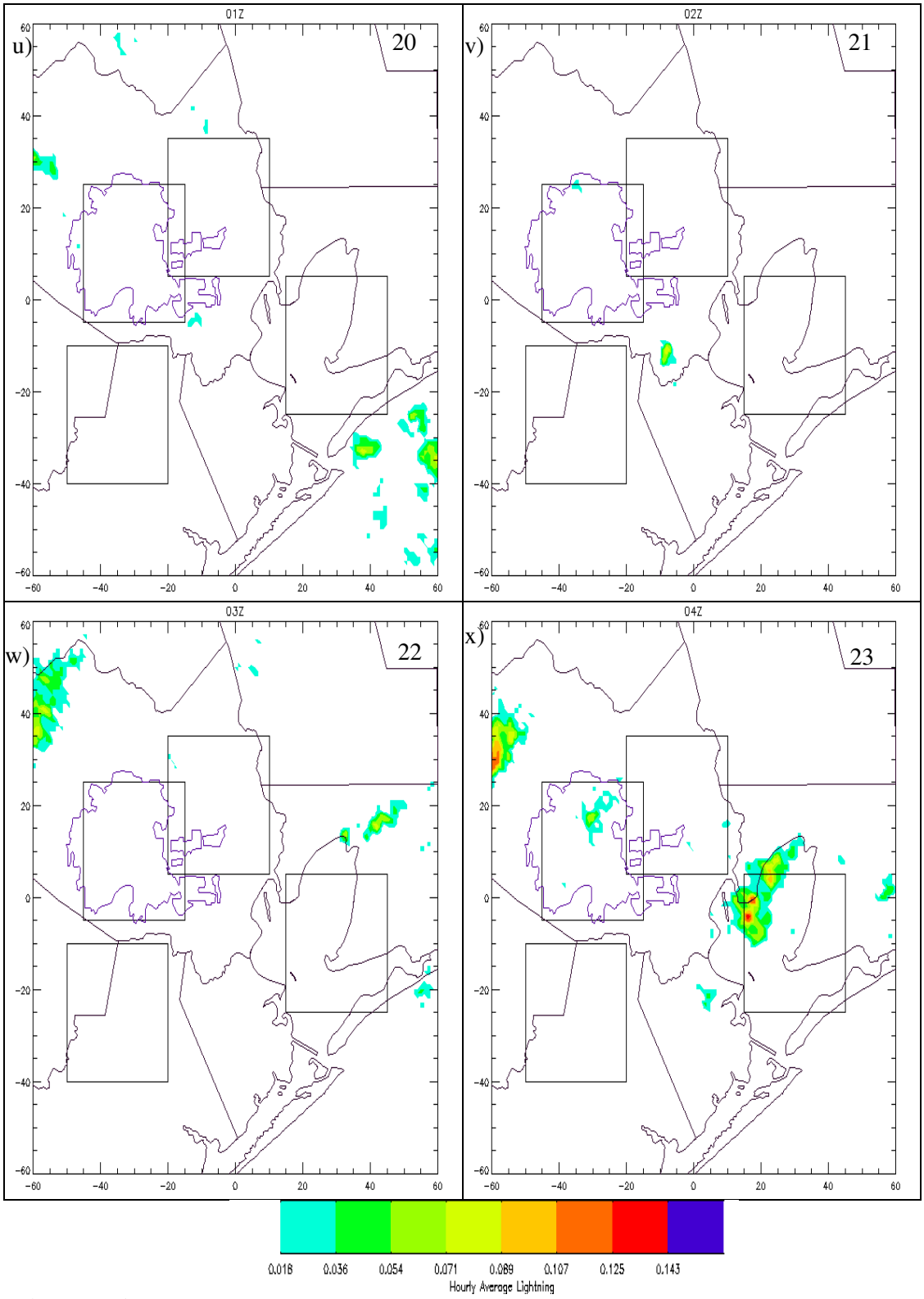

Figure 4.35 cont. (u-x) 20 to 23 LST.

Figure 4.36 presents the hourly time series for mean CG flash density. The domain mean was near zero km^{-1} hr^{-1} until 11 LST. The domain mean increased during the following two hours and reached a steady level of near 0.2 km^{-1} hr^{-1} until 19 LST at which point the mean decreased back to zero. Box 1 increase from 0 km^{-1} hr^{-1} at the same time of day as the domain, but increased sharply and reached a peak of 0.7 km^{-1} hr^{-1} at 14 LST. A second and third peak of near 0.4 km^{-1} hr^{-1} was reached at 16 and 18 LST, respectively. The box 1 mean returned to zero at 20 LST. Box 2 was nearly identical to box 1 and reached a similar peak as Box 1. Box 2 did not have any secondary peaks and decreased to zero by 17 LST. Box 3 slowly increased after 11 LST and sharply increased after 15 LST. Box 3 reached a peak of 1.5 km^{-1} hr^{-1} at 18 LST, and returned to zero at 19 LST. Box 4 remained near zero during each hour except 23 LST, at which point a peak of 0.4 km^{-1} hr^{-1} was reached.

Table 4.9 present the results of the Wilcoxon Rank-Sum test for average ground flash density. The box 1 mean was only significantly higher than the domain mean at 12 to 14, 16, 18, 19, and 23 LST. The mean was not significantly different from the domain mean at all other times. The box 2 mean was significantly higher between 13 and 16 LST, significantly lower at 17 and 18 LST, and not significantly different from the domain mean at all other times. The box 3 mean was significantly higher at 14 and 16 to 19 LST, significantly lower at 13 and 23 LST, and not significantly different from the domain mean at all other hours. The box 4 mean was only significantly higher at 23 LST, significantly lower from 12 to 18 LST, and not significantly different from the domain mean at all other times.

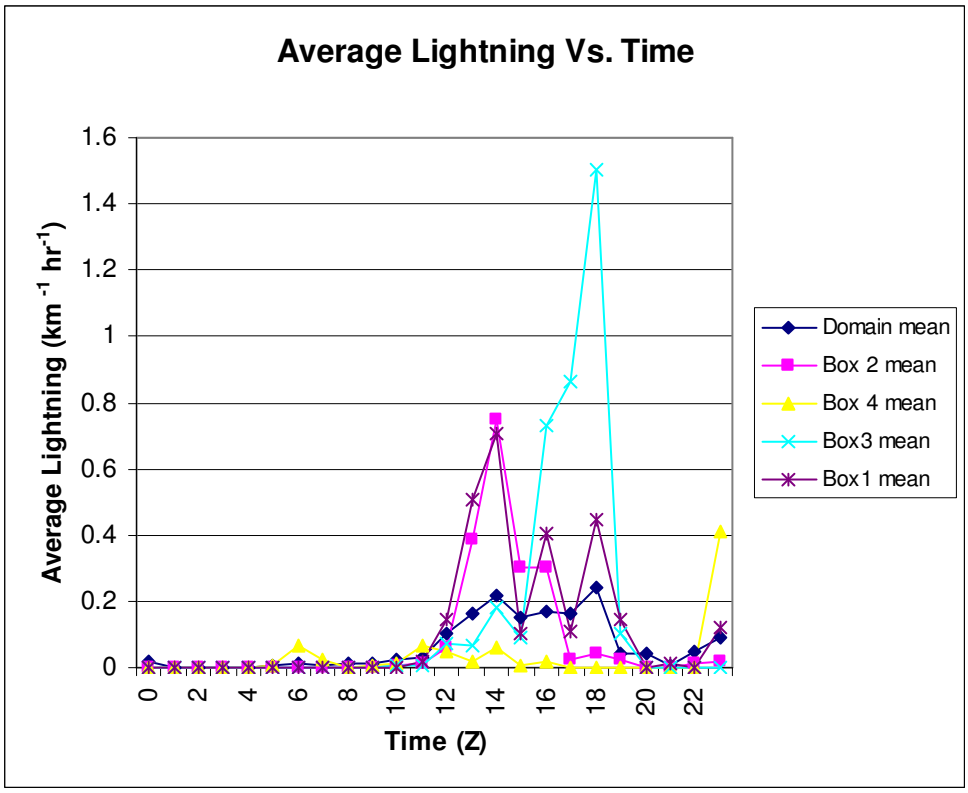

Figure 4.36. Hourly time series of average CG lightning flash density (km^{-1} hr^{-1}).

Table 4.9. Hourly Wilcoxon Rank-Sum results at the 5% significance level for box average CG lightning density. N indicates not significantly different, H is significantly higher, and L is significantly lower then the domain mean.

Hour (LST)	0	1	2	3	4	5	6	7	8	9	10	11	12	13	14	15	16	17	18	19	20	21	22	23
Box 1	N	N	N	N	N	N	N	N	N	N	N	N	H	H	H	N	H	N	H	H	N	N	N	H
Box 2	N	N	N	N	N	N	N	N	N	N	N	N	N	H	H	H	H	L	L	N	N	N	N	N
Box 3	N	N	N	N	N	N	N	N	N	N	N	N	N	L	H	N	H	H	H	H	N	N	N	L
Box 4	N	N	N	N	N	N	H	N	N	N	N	N	L	L	L	L	L	L	L	N	N	N	N	H

Figure 4.37 presents the daily average lightning. Over downtown Houston maximum CG density reached 0.214 lightning flashes km^{-1} day^{-1}. North and northeast of downtown, CG density reached 0.250 lightning flashes km^{-1} day^{-1}. South of Houston also experienced high CG flash density also reaching 0.250 km^{-1} day^{-1}. Most of the domain averaged 0.036 and 0.071 flashes km^{-1} day^{-1}. Large areas of no CG lightning activity include directly north of the Houston area, off shore of Galveston Bay and the central and southern portions of Galveston Bay. Lightning activity was present along the northern coast of Galveston Bay. The results of the Wilcoxon Rank-Sum test show that the means for boxes 1, 2, and 3 were significantly higher than the domain mean while the mean for box 4 was significantly lower.

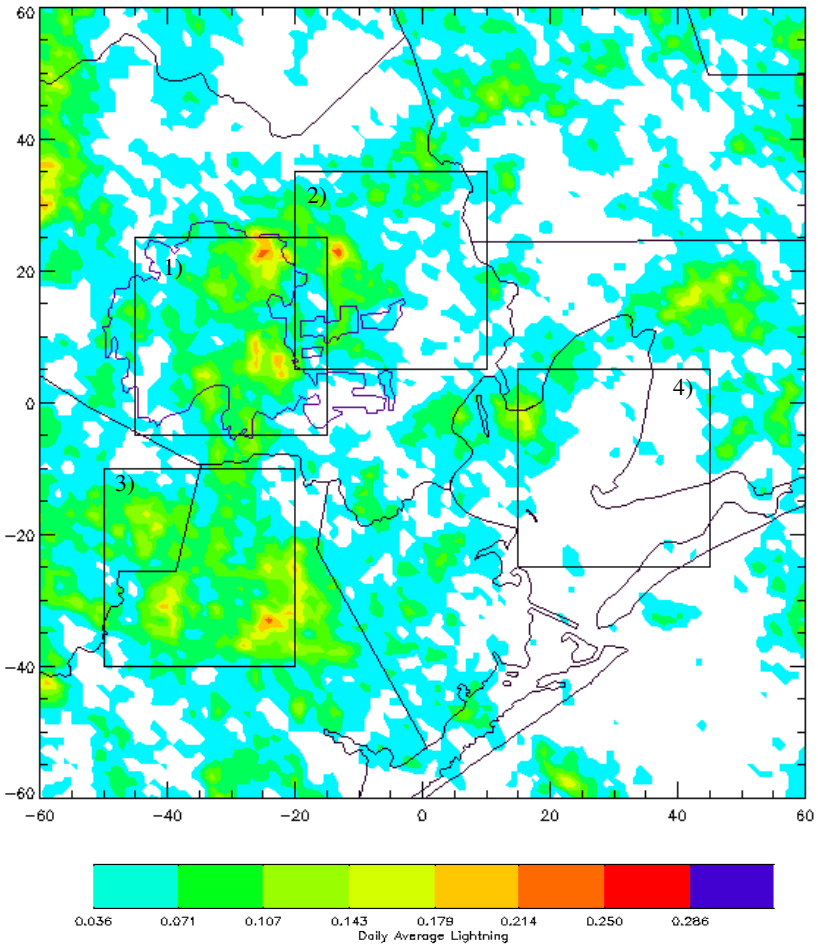

Figure 4.37. Daily average lightning ($km^{-}1\ day^{-1}$).

CHAPTER V

DISCUSSION

5.1 *Convergence and Convection*

The following sections will analyze the patterns that were present in the convergence field. Identifiable patterns that could be associated with the sea-breeze and the urban heat island will be discussed. The correlations between the convergence patterns and the convective frequency and intensity will be examined, along with correlations between convective strength and the presence of lightning.

5.1.1 *Convergence and UHI*

The location of boxes 1 and 2 were chosen to analyze the influence of Houston on convergence and convection. Box 3 was selected as an area that contained with comparable convective activity to boxes 1 and 2, but that should not be influenced by the UHI effects of Houston. The presence of convergence over most of the Houston area during the overnight hours as well as in the day indicates the presence of the UHI (Oke 1987). As mentioned in section 2, the UHI effect is more pronounced during the evening hours. South of Houston, there appears to be more divergence during almost all hours than over the Houston area. It is hard to be certain of the divergence due to the presence of radar artifacts in this area. During the overnight hours, there was a drop in convection in boxes 1, 2, and 3. The lack of convection during the overnight hours despite increased convergence in box 1, specifically, is likely due to the decrease of

favorable thermodynamics during the overnight hours. Due to increased convective inhibition in the evening, there was most likely insufficient lifting for parcels to reach the LFC. However, this cannot be verified due to the lack of sounding data for Houston.

Figure 5.1 presents a summary of the time series for the means of 7 km deep convective frequency, average cumulative rain, average convergence, and average lightning for the domain and each box. Convergence values in box 1 peaked at 9 LST, and values peaked at 8 LST for boxes 2 and 3. Also, the peak values for 2 and 3 were nearly 0.15 X 10^{-4} s^{-1} (60%) less than the peak for box 1. Convection in boxes 1, 2, and 3 increased dramatically between 9 and 10 LST. After this time, convergence decreases in all boxes until approximately 18 LST. This decrease in convergence is expected after the advent of convection due to rainfall, negative temperature perturbations (not shown), and downdraft divergence (e.g., seen in loops of velocity vectors for individual storms but not shown here). The strength of convection was approximately the same for all times in late morning and afternoon for all three boxes and for both 2 km and 7 km. However, between the times of 17 and 19 LST, the strength of the convection in box 1 and box 3 remained high while the strength of the convection in box 2 began to decrease.

The frequency of all events measured by the 2 km frequency was very similar across all 3 boxes. Box 2 decreased more quickly than box 1 and 3. Deep convection, measured by the count of above 30 dBZ at 7 km was over 2 times more frequent for boxes 1 and 2 than for box 3 at the peak at 14 LST. The drop in the frequency and strength of convection in box 2 after this time, while box 1 and box 3 maintain higher frequency and strength is most likely due to the proximity of box 2 to the Galveston Bay. The much larger peak in deep convective frequency seen in boxes 1 and 2 is likely the result of the UHI effect due to the fact that the sudden increase in deep convective frequency does not occur similarly in box 3, an area equally affected by the sea-breeze but not by the UHI. However, the bay-breeze, which occurs earlier in the day than the sea-breeze, was most likely the cause of the decrease in convection in box 2. More stable air, likely ushered in by the bay-breeze, enters the box 2 domain many hours before entering the box 1 or box 3 domains by the sea-breeze (Pielke 1974).

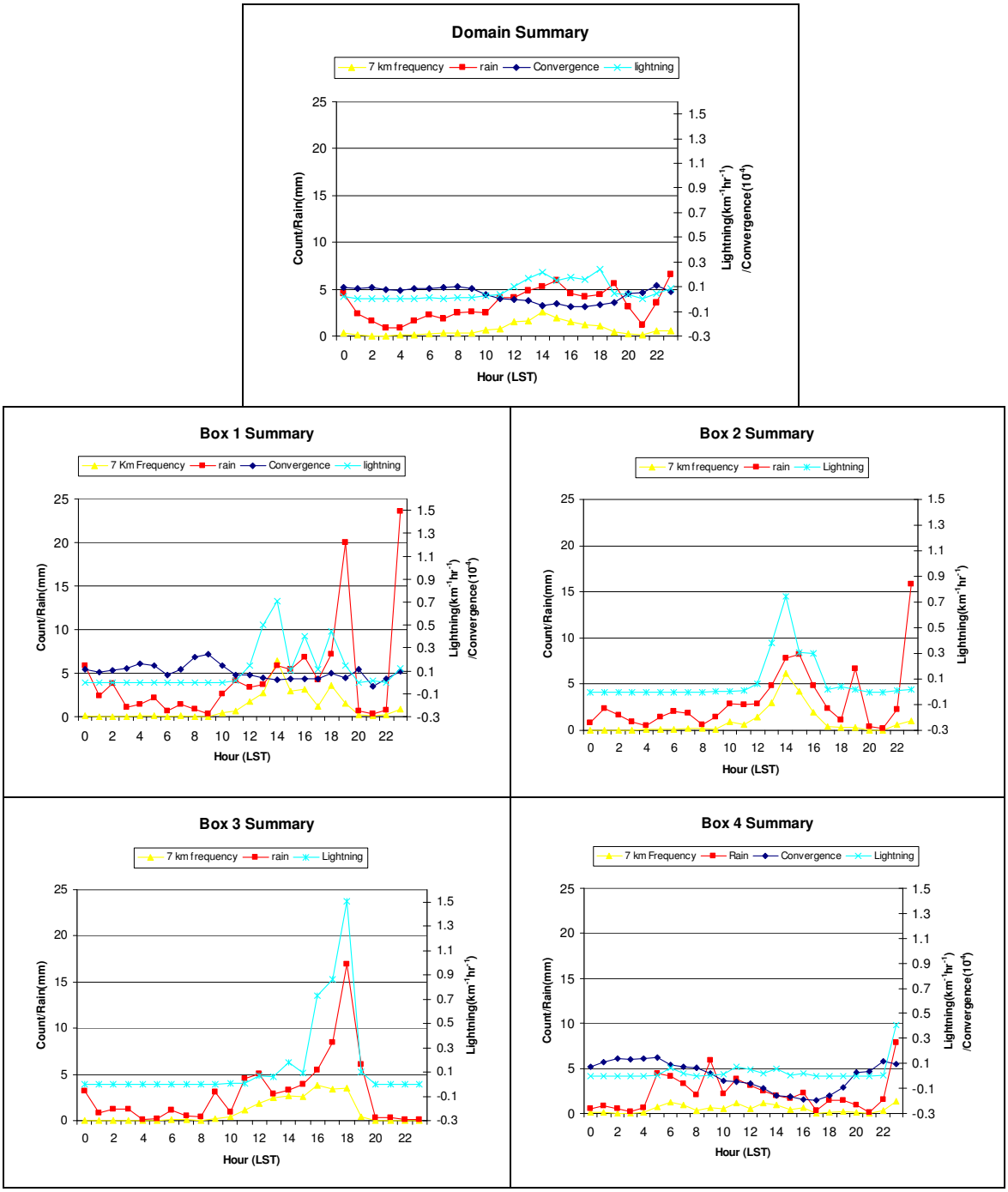

FIG. 5.1. Time series summary of 7 km frequency, average cumulative rain, average convergence, and average lightning for domain and box means. Convergence is not presented for boxes 2 and 3, and domain for convergence is as in Fig. 4.17.

The total average convergence also supports a role for UHI based on the convergence located over most of Houston and downwind, or north, northeast of Houston. The average divergence over west Houston is most likely not real and is a product of averaging strong divergence over this area during 6 LST when birds are present. The total average reflectivity at 2 km does not strongly support the presence of a UHI effect. However, the total average count at 2km does indicate higher frequencies of reflectivities above 30 dBZ over the Houston area than the surrounding areas. At 7 km, the higher reflectivities in the total average reflectivity over the Houston downtown area would indicate the UHI. The count of above 30 dBZ at 7 km strongly indicates the presence of a UHI. This would indicate that the UHI does not affect the convective frequency, but rather the convective intensity, as indicated by the 7 km reflectivity and deep convective count. The increase in the height of convective tops over St. Louis also indicates that UHI affects the intensity of convection (Braham 1991). The downtown and downwind area experienced a far higher frequency of occurrence of deep convection than the surrounding areas.

For comparison, Figure 5.2 presents an overlay of deep convective frequency (i.e., counts of occurrence of > 30 dBZ at 7 km from Figure 4.31) and a Houston land use map. The high density developed and medium density developed land use are white and light grey, respectively. A large area of deep convective counts greater than 30 encircles the downtown area. Deep convective frequency in this area was greater than 40. Rural and low density areas surrounding Houston averaged 15 to 20 occurrences of > 30 dBZ at 7 km. The influence of the UHI over Houston appears to be sensitive to local changes

in land use. Memorial Park is a conservation park in West Houston. The park encompasses 1500 wooded acres[6], which is double the size of Central Park (New York), and is noted on the map by a large area of dark green just inside the Houston city limits. Despite the park's proximity to Houston, the deep convective frequency over this area only averaged 5 to 10. A park cooling effect was identified in Spronken-Smith and Oke (1998) in which parks in an urban setting averaged 5°C cooler than the surrounding urban setting. The cooler air would cause local divergence over the park setting, inhibiting convection. Higher counts did extend downwind of the city, to the north north-east of the city, and directly north of the east end of the downtown. Steering-level winds for convection most often occur out of the south-southeast and southwest (Shepherd and Burian 2003). Due to this, it would be expected that higher counts would occur downwind of the entire downtown area (i.e., also north of the west end of the downtown). It, therefore, seems possible that the presence of the park is inhibiting the progression of deep convection over and northward of the west side of the city.

Figure 5.2 also gives insight into convective patterns not associated with Houston. Forested and non-cropland areas shows areas of decreased deep convective frequency, mostly averaging between 5 and 15 counts. Increased counts of > 30 dBZ at 7 km were also present over cultivated herbaceous land (brown). Deep convective frequency here averaged 25 to 40. Increased moisture due to irrigation in these areas is most likely the cause of the increased deep convection, similar to the findings of Baker et al. (2001).

[6] http://www.memorialparkconservancy.org/index.cfm/MenuItemID/157.htm

The increased moisture results in a decrease of the height of the LFC which would result in more convection.

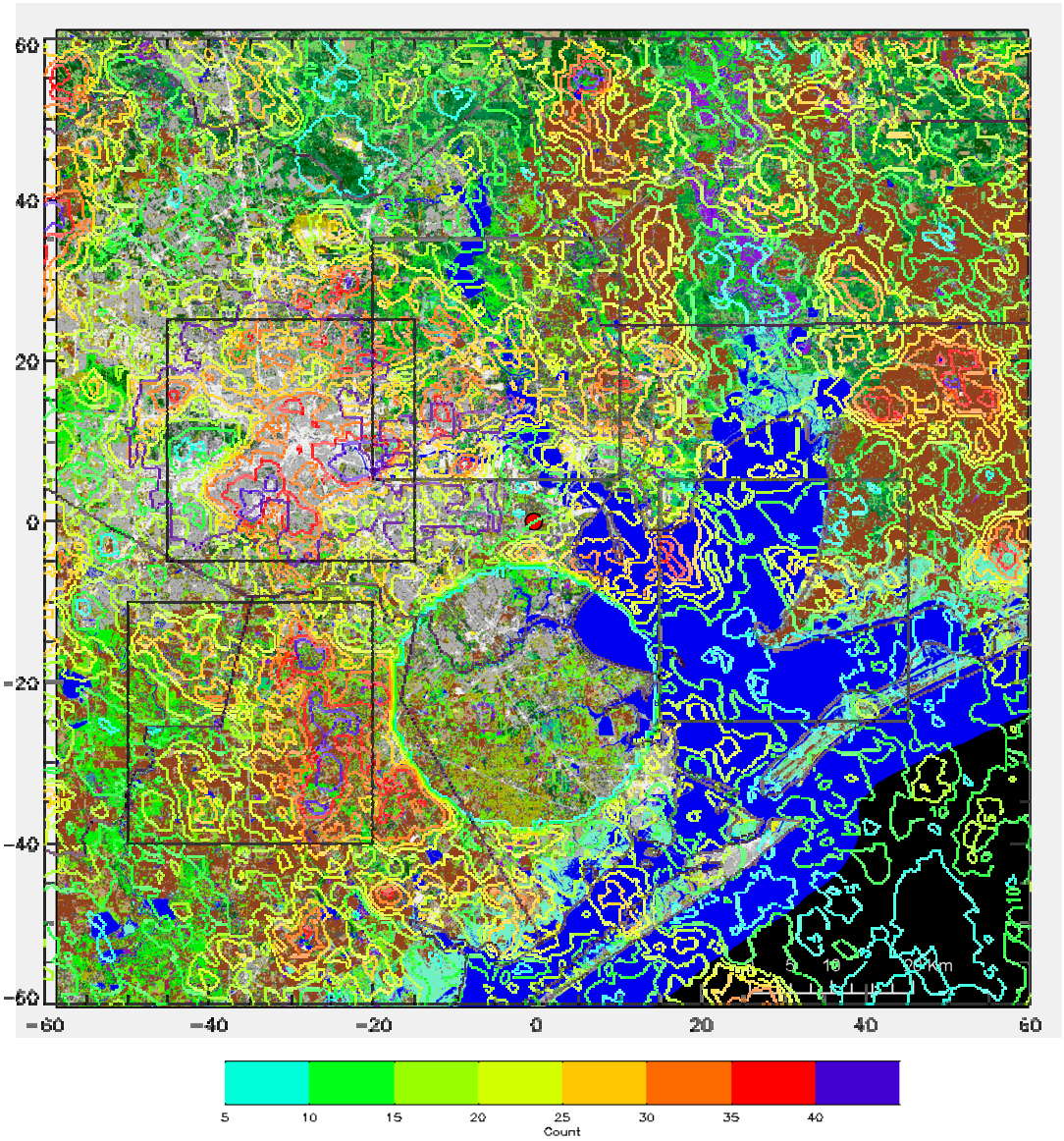

FIG 5.2. Overlay of Figure 4.31 with a Houston 30 meter resolution land use map provided by TCEQ. White is high density developed, light gray is medium density developed, dark grey is low density developed, green is vegetation, brown is crop land, and blue is water.

5.1.2 *Convergence and Sea-Breeze*

The increased convergence over Galveston Bay during the nighttime hours is produced by a land breeze over the Bay (Aksoy et al. 2005). Convergence was the highest for box 4 between 22 and 5 LST. At 6 LST, with the sunrise, it would be expected that convergence would weaken due to the weakening land-breeze. Shortly after sunrise, a halt of the land breeze and a transition to bay-breeze should occur (Banta et al. 1993). Convection did not begin over this area until just before sunrise at 5 LST and was much weaker than the surrounding domain after 10 LST. Convergence began falling after 5 LST in box 4, while convergence in box 1 began rising after this time.

The box 3 domain is not affected by UHI. Unfortunately, convergence for box 3 is greatly affected by the presence of radar artifacts. However, the convective pattern in box 3 shows a gradual increase in convection after 10 LST, reaching a peak at 15 to 17 LST. This time frame agrees with the findings of Aksoy et al. (2005). By modeling the sea-breeze, it was found that by 3 pm local time, the most intense convergence moves inland, and by 6 pm a distinct frontal boundary is present. Box 3 is also located adjacent to both the Galveston Bay and the coast. This is an area of cultivated land, though it is more sporadically mixed with forested land than the areas north and east of Galveston Bay. Therefore, it is unlikely that the high levels of convection here are entirely due to irrigation. The interactions of the bay-breeze and the sea-breeze could be providing additional forcing for convection. A similar effect was found by Pielke (1974) involving an enhancement of convection where the lake-breeze from Lake Okeechobee and the Atlantic sea-breeze interact.

A weaker enhancement was located along the northern coast of the Galveston Bay similar to the results of McPherson (1970) and Gibson and Vonder Haar (1990). The maximum occurred along a convex coastline, which has been shown to be an area of increased convergence (Pielke 1974; Baker at al. 2001). The majority of convection at this location occurred between the hours of 5 and 11 LST, with the exception of an isolated event that occurred at 22 and 23 LST. During the early morning time frame, the bay-breeze would have been weak or non-existent (Pielke 1974). Convection would then form along the coast, rather than inland, because the moist air would not be advected away from the coastline by the bay-breeze.

The average winds also revealed the Galveston Bay land-breeze, bay-breeze, and the sea-breeze. The presence of northerly winds over Galveston Bay beginning just after sunset and lasting until 2 LST were due to offshore flow to the Galveston Bay. Also, shortly after sunset, nightly bird migration occurs. This migration could result in erroneous northerly winds over the entire domain. The hour of sunrise, and the hour following, was marked by less uniform winds over most of the domain. This corresponds with a time of weakening of the land-breeze. At noon winds began to shift from out of the south near the Bay, likely marking the beginning of the bay-breeze. The lack of an eastward bay-breeze is most likely due to the shallowness of the bay-breeze and the height of the radar beam. A bay-breeze can be limited to less than 500 meters (Abbs 1986). The lowest radar beam would have been near 600 meters above the surface at a distance of 40 kilometers from the radar and, therefore, unable to sample low-level winds and the bay-breeze would be missed.

A sea-breeze feature of weak winds out of the southeast began appearing as early as one hour after sunrise in the southern portion of the west dual-Doppler lobe. A pattern of increasing sea-breeze strength is evident on the time-series image and the hourly maps, steadily increasing after 10 LST. By 15 LST the sea-breeze feature began to appear over Galveston Bay, indicated by more easterly winds. By 17 LST box 4 was characterized by southeasterly wind on average, indicating the advancement of a deep sea-breeze over Galveston Bay. The difference in the advancement of the sea-breeze between the land and Galveston Bay is due to the weaker temperature gradient over Galveston Bay. This resulted in the slower advancement of the sea-breeze over the bay, which was also identified in Abbs (1986). Based on the time-series, the sea-breeze reached a peak in strength at 19 LST in box 1. Aksoy et al. (2005) found the peak sea-breeze to occur 9 hours after maximum heating (noon). The wind speed average in box 1 at 20 LST was nearly half the strength of 19 LST. It is important to note that bird migration also begins shortly after sunrise, which can skew the winds to more northerly. However, bird migration does not typically appear in the radar signal until 30 to 45 minutes after sunset, more closely correlating to 21 LST (Schulze 2003). Therefore, the timing of the weakening of the winds at 20 LST is almost certainly a weakening sea-breeze rather than the appearance of birds. The time of 19 LST correlates more closely with the convection in box 3, which peaked at 18 LST. Boxes 1 and 2 peaked much earlier in the day, at 14 LST. There was a small enhancement at 18 LST, most likely due to the sea-breeze. This would also indicate that the strongest enhancements over boxes 1 and 2 were due mainly to UHI due to the timing of the strong convection in boxes 1 and

2. Had sea-breeze been the main forcing in boxes 1 and 2, the timing of the convection would more closely correspond to the timing of maximum sea-breeze.

An interesting feature present on the averaged wind maps is the presence of anti-cyclonic circulation located at the northwest edge of Galveston Bay. This vortex is present between midnight and sunrise when northerly winds were the strongest over Galveston Bay. Abbs (1986) observed and simulated a similar type of mesoscale vortex over the northwest edge of Port Phillip Bay in Australia. The circulation in that study began at sunset and was speculated to have been caused by a combination of low-level convergence due to the interaction of the sea-breeze and bay-breeze and the mountainous topography. However, it was suggested that the orography was not necessary for the vortex formation. The vortex was formed in situations with a northeasterly geostrophic flow with a southeasterly bay-breeze and sea-breeze.

5.2 *Lightning and Convective Strength*

The relationship between lightning and convective strength is examined by the correlation between the amount of convective events with strengths of 30 dBZ or greater at 7 km and the presence of lightning (Larsen and Stansbury 1974, Marshall and Radhakant 1978). With very few exceptions, lightning events correlated with convective strengths greater than 30 dBZ. However, many deep convective events occurred with the presence of little or no lightning. The presence of deep convection appears to be necessary for lightning to occur, but other causative mechanisms must be present. The box 1 and box 2 time-series pattern for the deep convective count closely matches the

lightning time-series for the same boxes. The box 3 lightning time-series peak at 18 LST is not matched by a similar peak in the deep convection time-series. By analyzing the frequency maps, it appears that this peak in lightning was caused by a single, large convective event. A correlation between lightning and the total 7 km convective count is also seen on the total images. All significant areas of lightning correlated with high frequencies of deep convection.

5.3 *The Houston Lightning and Rainfall Anomaly*

The findings of this study back the previous findings of an enhancement in rainfall and lightning over the Houston area. The box 1 and box 2 domains were significantly higher for 2 km average reflectivity, 7 km average reflectivity, 7 km convective frequency, lightning, and average cumulative rainfall than the domain mean. Box 2 was not significantly different than the domain for 2 km frequency while box 1 was significantly higher. The enhanced lightning observed over and downwind of the Houston downtown area in this study was similar in magnitude and location to the results of Orville et al. (2001), Steiger et al. (2002), and Gauthier et al. (2005). However, the magnitude south of Houston (box 3) was found to be more pronounced than the previous studies. However, the length of this study compared to the previous studies could potentially explain the difference in convection south of Houston.

The enhancement in radar derived rainfall correlates with the location of the enhanced lightning. The rainfall findings also correlate well with the rain-gauge results found by Shepherd and Burian (2003). The maxima in rainfall in the northern portion of

the domain do not correlate well with other deep convective features. These maxima may have been produced by a high mean rain rate or a long period of rainfall or both. The enhancement of rainfall, which correlated with an enhancement in lightning, south of the Houston area was also identified by Shepherd and Burian.

Diurnally, box 1 and box 2 were most often significantly higher than the domain mean for the same parameters during the afternoon hours. Most rainfall occurred between the hours of 10 and 19 LST for boxes 1, 2, and 3. Burian and Shepherd (2005) found an increase in rainfall in the Houston urban area and downwind of Houston for the warm season months (June, July, and August) between the hours of 12 and 20 LST.

CHAPTER VI

CONCLUSION

This thesis further examined the Houston lightning and rainfall anomaly with the use of derived boundary-layer radar parameters along with volumetric radar reflectivity. Mass processing of large amounts of radar data were completed for the months of July, August, and September of 2005 for Houston and Dallas. It was found that the boundary layer winds were not significantly different than other wind observations and were generally useful for scientific analysis. However, some artifacts, such as bird migration, remained in the radar inferred horizontal winds even after processing and filtering of the data. Hence, care was taken not to interpret these artifacts as meteorological signals.

The results of this study, conducted during one summer season, supported the results of previous findings involving the enhancement of convection over the Houston area. The downtown Houston area, as well as downwind of downtown, had an increase of deep convection, and its associated by-products, namely rainfall and lightning, when compared to the domain mean. More unique to this study was the increase in deep convection, rainfall, and lightning south of the Houston area during the analysis period. This feature was only also identified in the study by Shepherd and Burian (2003). The timing and location of rainfall was also similar to those found in Burian and Shepherd (2005) and Shepherd and Burian (2003).

Based on the findings from this study, it was concluded that the increase in convection over Houston was mostly consistent with the UHI effect. The downtown and

downwind area experienced a sudden increase in convection after noon. The downtown area remained higher in frequency until sunset, while the downwind area decreased in frequency shortly after 14 LST. The area to the south of Houston, not affected by UHI effect, exhibited no such sudden increase in convection, but rather a gradual increase in convection up to the time of the strongest sea-breeze signal. Box 1 and box 2 experienced only a small enhancement of convection at that time, indicating a much smaller role for sea-breeze in convection over Houston. Also, the lack of deep convection over Memorial park, an area that would be as equally affected by the sea-breeze as the surrounding Houston area, likely indicates the importance of the UHI in the presence of deep convection. Before we can generalize this latter conclusion, more research is required to fully understand the thermodynamic and dynamic impact of the forested Memorial park area embedded within the larger Houston urban zone on UHI, convective frequency and intensity, lightning, and rainfall.

The relative increase in convection south of Houston during the period of this study appears to be greatly influenced by the sea-breeze. This location may be affected by a convergence zone caused by the collision of the bay-breeze and the sea-breeze. Other areas of increased convection exist over land identified as cultivated herbaceous. The increase in these areas is most likely due to the increase in moisture due to the irrigation present on this land. However, more research and a larger data sample are required to confirm this speculation. As is expected, areas that are labeled as water or forest experienced the least amount of convection (Negri et al. 2004), deep convection, rainfall, and lightning.

This study also found a correlation between high reflectivities at heights above the freezing level (e.g., -10° to -20°C) and the presence of lightning, as suggested by many past studies that are summarized in Vincent et al. (2004). The presence of lightning was co-located with an area of high (> 30 dBZ) reflectivity at temperatures near -10°C (7 km). However, not every area of high reflectivity also had lightning present indicating the importance of microphysics and/or updraft intensity inside the thunderstorms or perhaps that a higher radar reflectivity threshold should have been used (e.g., Vincent et al. 2004).

Future research would require the processing of dual-Doppler data over multiple summer seasons in the Houston area, including multiple platforms for boundary layer measurements, and modeling studies of convergence over Houston and convection. This additional research would further back up trends highlighted in this study and ensure that any correlations were not coincidental. Preliminary results of Memorial Park seem to be generally consistent. It would also be useful to acquire better dual-Doppler data for the areas to the south of Houston, where the current dual-Doppler data was contaminated. By doing this, it could be possible to resolve whether this area is affected by a collision of the bay-breeze and sea-breeze. A sea-breeze, bay-breeze model would also contribute to the understanding of the convection occurring in this area. Also, further research could investigate the impact of large parks in urban settings on localized convergence and convection through a local field project as well as modeling studies. A model which explored the couplet of the sea-breeze and the UHI over Houston could be used to

validate the findings of this research on the influences of either on convection in the Houston area.

REFERENCES

Abbs, D. J., 1986: Sea-breeze interactions along a concave coastline in Southern Australia: Observations and numerical modeling study. *Mon. Wea. Rev.,* **114**, 831-848.

Aksoy, A., F. Zhang, J. W. Nielsen-Gammon, and C. Epifanio, 2005: Ensemble-based data assimilation for thermally forced circulations. *J. Geo. Res.* **110**: doi:10.1029/2004JD005718.

Armijo, L., 1969: A theory for the determination of wind and percipitation velocities with Doppler radars. *J. Atmos. Sci.,* **26**, 570-573.

Arya, S. P., 2001: *Introduction to Micrometeorology*. Academic Press. 420 pp.

Atkins, N. T. and R. M. Wakimoto, 1997: Influence of the synoptic-scale flow on sea breezes observed during CaPE. *Mon. Wea. Rev.,* **125**, 2112-2130.

Auer, Jr., A. H., 1981: Urban boundary layer. *METROMEX: A Review and Summary, Meteor. Monog.,* Amer. Meteor. Soc. **40,** 41-62.

Avila, E. E., A. V. G. Guillermo, and G. M. Caranti, 1995: Temperature dependence of static charging in ice growth by riming. *J. Atmos. Sci.,* **52**, 4515-4522.

Avila, E. E., G. M. Caranti, N. Castellano, and C. Saunders, 1998: Laboratory studies of the influence of cloud droplet size on charge transfer during crystal-graupel collisions. *J. Geo. Res.,* **103**, 8985-8996.

Baker, D. R., B. H. Lynn, A. Boone, W. Tao, and J. Simpson, 2001: The influence of soil moisture, coastline curvature, and land-breeze circulations on sea-breeze-initiated precipitation. *J. Hydrometeor.,* **2**, 193-211.

Banta, R. M., L. D. Olivier, and D. H. Levinson, 1993: Evolution of the Monterey Bay sea-breeze layer as observed by pulsed Doppler lidar. *J. Atmos. Sci.,* **50**, 3959-3982.

Banta, R. M., C. J. Senff, J. Nielsen-Gammon, L. S. Darby, T. B. Ryerson, R. J. Alvarez, S. P. Sandberg, E. J. Williams, and M. Trainer, 2005: A bad air day in Houston. *Bull. Amer. Meteor. Soc.,* **86**, 657-669.

Biggerstaff, M. I., L. J. Wicker, J. Guynes, C. Ziegler, J. M. Straka, E. N. Rasmussen, A. Doggett IV, L. D. Carey, J. L. Schroeder, and C. Weiss, 2005: The shared mobile atmospheric research and teaching radar. *Bull. Amer. Meteor. Soc.,* **86**, 1263-1274.

Braham Jr., R. R., 1981: Urban precipitation processes. *METROMEX: A Review and Summary. Meteor. Monog.*, Amer. Meteor. Soc. **40,** 75-115.

Burian, S. J. and J. M. Shepherd, 2005: Effect of urbanization on the diurnal rainfall pattern in Houston. *Hydrol. Process.,* **19**, 1089-1103.

Burpee, R. W. and L. N. Lahiff, 1983: Area-average rainfall variations on sea-breeze days in South Florida. *Mon. Wea. Rev.,* **112**, 520-534.

Carey, L. D. and S. A. Rutledge,1996: A multiparameter radar case study of the microphysical and kinematic evolution of a lightning producing storm. *Meteorol. Atmos. Phys.,* **59**, 33-64.

Carey, L. D. and S. A. Rutledge, 2000: The relationship between precipitation and lightning in tropical island convection: A c-band polarimetric radar study. *Mon. Wea. Rev.,* **128**, 2687-2710.

Carey, L. D., 2005: Final progress report for the c-band radar project. Texas A&M University. Prog. Rep. 47pp.

Changnon, Jr., Stanley A., 1980: Evidence of urban and lake influences on precipitation in the Chicago area. *J. Appl. Meteor.,* **19**, 1137-1159.

Changnon, Jr., Stanley A., R. T. Shealy, and R. W. Scott, 1991: Precipitation changes in fall, winter, and spring caused by St. Louis. *J. Appl. Meteor.,* **30**, 126-134.

Cooper, H. J., M. Garstang, and J. Simpson, 1982: The diurnal interaction between convection and peninsular-scale forcing over South Florida. *Mon. Wea. Rev.,* **110**, 486-503.

Cressman, G. P., 1959: An operational objective analysis system. *Mon. Wea. Rev.,* **87**, 367-374.

Cummins, K. L., M. J. Murphy, E. A. Bardo, W. L. Hiscox, R. B. Pyle, and A. E. Pifer, 1998: A combined TOA/MDF technology upgrade of the U.S. National Lightning Detection Network. *J. Geo. Res.,* **103**, 9035-9044.

Cummins, K. L., J. A. Cramer, C. J. Biagi, P. E. Krinder, J. Jerauld, M. A. Uman, and V. A. Rakov, 2006: The U.S. National Lightning Detection Network: Post-upgrade status. Preprints, *2nd Conf. on Meteor. Appl. of Lightning Data*. Atlanta, GA, Amer. Meteor. Soc., CD-ROM.

Davies-Jones, R. P., 1979: Dual-Doppler radar coverage area as a function of measurements accuracy and spatial resolution. *J. Appl. Meteor.,* **18**, 1229-1233.

Dixon, G. P. and T. L. Mote, 2003: Pattern and causes of Atlanta's urban heat island-initiated precipitation. *J. Appl. Meteor*., **42**, 1273-1284.

Doviak, R. J. and D. S. Zrnic, 1993: *Doppler Radar and Weather Observations*. 2nd ed. Academic Press, Inc, 562 pp.

Gauthier, M. L., W. A. Petersen, L. D. Carey, and R. E. Orville, 2005: Dissecting the anomaly: A closer look at the documented urban enhancement in summer season ground flash densities in and around the Houston area. *Geo. Res. Lett*., **32,** doi:10.1029/2005GL022725.

Gauthier, M. L., 2006: Urban influences on convection and lightning over Houston. Dept. of Atmospheric Science, Huntsville, AL, University of Alabama in Huntsville. 169 pp.

Gauthreaux Jr., S. A., D. S. Mizrahi, and C. G. Belser, 1998: Bird migration and bias of WSR-88D wind estimates. *Wea. Forecasting,* **13**, 465-481.

Gibson, H. M. and T. H. Vonder Haar, 1990: Cloud and convection frequencies over the Southeast United States as related to small-scale geographic features. *Mon. Wea. Rev.,* **118**, 2215-2227.

Kelly, D. L., J. T. Schaefer, R. P. McNulty, C. A. Doswell III, and R. F. Abbey, Jr., 1978: An augmented tornado climatology. *Mon. Wea. Rev.,* **106**, 1172-1183.

Kessinger, C., S. Ellis, J. Van Andel, and J. Hubbert, 2004: Current and future plans for the AP Clutter Mitigation Scheme. Preprints, *20th Int. Conf. on Interactive Information and Processing Systems (IIPS) for Meteor.,* Seattle, WA, Amer. Meteor. Soc., CD-ROM.

Kingsmill, D. E, 1995: Convection initiation associated with a sea-breeze front, a gust front, and their collision. *Mon. Wea. Rev.,* **123**, 2913-2933.

Kurbatskii, A. F., 2001: Computational modeling of the turbulent penetrative convection above the urban heat island in a stably stratified environment. *J. Appl. Meteor.,* **40**, 1748-1761.

Larsen, H. R. and E. J. Stansbury, 1974: Association of lightning flashes with precipitation cores extending to height 7 km. *J. Atmos. Terr. Phys.,* **36**, 1547-1553.

Lhermitte, R. M. and J. L Miller, 1970: Doppler radar methodology for the observation of convective storms. Preprints, *14th Conf. Radar Meteorology*, Tucson, AZ, Amer. Meteor. Soc., 133-138.

Liu, S., Q. Xu, and P. Zhang, 2004: Identifying Doppler velocity contamination caused by migrating birds. Part II: Bayes identification and probability tests. *J. Atmos. Oceanic Technol.* **22**, 1114-1121.

Marshall, J. S. and S. Radhakant, 1978: Radar precipitation maps as lightning indicators. *J. Appl. Meteor.,* **17**, 206-212.

McPherson, R. D., 1970: A numerical study of the effect of a coastal irregularity on the sea breeze. *J. Appl. Meteor.,* **9**, 767-777.

Miller, J. L., C. G. Mohr, A. J. Weinheimer, 1986: Simple rectification to Cartesian space of folded radial velocities from Doppler radar sampling. *J. Atmos. Oceanic Technol.,* **3**, 162-174.

Miller, J. L. and S. M. Fredrick, 1998: CEDRIC-Custom Editing and Display of Reduced Information in Cartesian Space. Boulder, CO, NCAR Tech. Memo, MMM Division**,** 130.

Mohr, C. G. and J. L. Miller, 1983: A software package for Cartesian space editing, synthesis, and display of radar fields under interactive control. Preprints, *21st Conf. on Radar Meteorology,* Boston, MA, Amer. Meteor. Soc.*,* 569-574.

Negri, A. J., R. F. Adler, L. Xu, and J. Surratt, 2004: The impact of Amazonian deforestation on dry season rainfall. *J. Climate,* **17**, 1306-1319.

Oke, T. R., 1987: *Boundary Layer Climates, 2nd. Ed.*, Methuen, 435 pp.

Orville, R. E., G. Huffines, J. Nielsen-Gammon, R. Zhang, B. Ely, S. M. Steiger, S. Phillips, S. Allen, and W. Read, 2001: Enhancement of cloud-to-ground lightning over Houston, Texas. *Geo. Res. Lett.,* **28**, 2597-2600.

Oye, D. and M. Case, 1995: REORDER: a program for gridding radar data. Installation and use manual for the Unix version. Boulder, CO, NCAR Atmospheric Technology Division.

Pereyra, R. G., E. E. Avila, N. E. Castellano, and C. P. R. Saunders, 2000: A laboratory study of graupel charging. *J. Geo. Res.,* **105**, 20,803-20,812.

Pielke, R. A., 1974: A three-dimensional numerical model of the sea breezes over South Florida. *Mon. Wea. Rev.,* **102**, 115-139.

Rinehart, R. E., 2004: *Radar for Meteorologists.* 4th ed. Rinehart Publications, 482 pp.

Rosenfeld, D., D. B. Wolff, and D. Atlas, 1993: General probability-matched relations between radar reflectivity and rain rate. *J. Appl. Meteor.,* **32**, 50-72.

Rozoff, C. M., W. R. Cotton, and J.O. Adegoke, 2003: Simulation of St. Louis, Missouri, land use impacts on thunderstorms. *J. Appl. Meteor*., **42**, 716-738.

Russell, K. R. and S. A. Gauthreaux Jr., 1998: Use of weather radar to characterize movements of roosting purple martins. *Wildlife Soc. Bull.,* **26**, 5-16.

Ryzhkov, A. V. and D. S. Zrnic, 1998: Observations of insects and birds with a polarimetric radar. *IEEE Trans. Geosci. Remote Sens*., **36**, 661-668.

Saunders, C. P. R. and S. L. Peck, 1998: Laboratory studies of the influence of the rime accretion rate on charge transfer during crystal/graupel collisions. *J. Geo. Res.,* **103**, 13,949-13,956.

Schulze, K. W., 2003: An investigation into the contamination of WSR-88D vad wind profile output by migrating birds. M.S. Thesis. Dept. of Atmospheric Science, College Station, TX, Texas A&M University. 177pp.

Shepherd, J. M., B. S. Ferrier, and P. S. Ray, 2001: Rainfall morphology in Florida convergence zones: A numerical study. *Mon. Wea. Rev.,* **129**, 177-197.

Shepherd, J. M. and S. J. Burian, 2003: Detection of urban-induced rainfall anomalies in a major coastal city. *Earth Interaction*, **7**, 1-17.

Smith, J. R., H. E. Fuelberg, and A. I. Watson, 2005: Warm season lightning distributions over the Northern Gulf of Mexico Coast and their relation to synoptic-scale and mesoscale environments. *Wea. Forecasting,* **20**, 415-438.

Spronken-Smith, R. A. and T. R. Oke, 1998: The thermal regime of urban parks in two cities with different summer climates. *Inter. J. Remote Sensing,* **19**, 2085-2104

Stallins, J. A., M. L. Bentley, and L.S. Rose, 2006: Cloud-to-ground flash patterns for Atlanta Georgia (USA) from 1992 to 2003. *Clim. Res.,* **30**, 99-112.

Steiger, S. M., R. E. Orville, and G. Huffines, 2002: Cloud-to-ground lightning characteristics over Houston, Texas: 1989 - 2000. *J. Geo. Res.,* **107**, 4117-4128.

Streutker, D. R., 2002: Satellite-measured growth of the urban heat island of Houston, Texas. *Remote Sensing Environ.,* **85**, 282-289.

Stull, R. B., 1988: *An Introduction to Boundary Layer Meteorology*. Kluwer Academic Publishers, 666 pp.

Takahashi, T., 1978: Riming electrification as a charge generation mechanism in thunderstorms. *J. Atmos. Sci.,* **35**, 1530-1548.

U.S. Census Bureau, 2005: July 1, 2005 population estimates for metropolitan, micropolitan, and combined statistical areas. U.S. Census Bureau Office Population Division. [Available online at http://www.census.gov/population/www/estimates /Estimates%20pages_final.html.]

Vincent, B. R., L. D. Carey, D. Schneider, K. Ketter, and R. Gonski, 2004: Using WSR-88D reflectivity data for the prediction of cloud-to-ground lightning: A central North Carolina study. *Natl. Weather. Dig.* **27**, 35-44.

Westcott, N. E., 1995: Summertime cloud-to-ground lightning activity around major midwestern urban areas. *J. Appl. Meteor.,* **34**, 1633-1642.

Williams, E. R., M. E. Weber, and R. E. Orville, 1989: The relationship between lightning type and convective state of thunderclouds. *J. Geo. Res.,* **94**, 13213-13220.

Wilson, J. W., T. M. Weckwerth, J. Vivekanandan, R. M. Wakimoto, and R. W. Russel, 1994: Boundary layer clear-air radar echoes: origin of echoes and accuracy of derived winds. *J. Atmos. Oceanic Technol.,* **11**, 1184-1206.

Zhang, P., S. Liu, and Q. Xu, 2005: Identifying Doppler velocity contamination caused by migrating birds. Part I: Feature extraction and quantification. *J. Atmos. Oceanic Technol.,* **22**, 1105-1113.

Zrnic, D. S., V. M. Melnikov, and A. V. Ryzhkov, 2006: Correlation coefficients between horizontally and vertically polarized returns from ground clutter. *J. Atmos. Oceanic Technol.,* **23**, 381-394.

VITA

Name:	Veronica Ann McNear
Address:	P.O. Box 768, Atlanta, IL 61723
E-mail Address:	vmcnear@verizon.net
Education:	B.S., Synoptic Meteorology, Purdue University, 2004 M.S., Atmospheric Science, Texas A&M University, 2007